

A Manual for Conducting Image-Based Inertial Impact (IBII) Tests

Lloyd Fletcher¹ Jared Van Blitterswyk¹
Fabrice Pierron¹

¹*Faculty of Engineering and Physical Sciences, University of Southampton, UK*

August 22, 2019

Abstract

For brittle and low wave speed materials testing, with the split-Hopkinson pressure bar is difficult at high strain rates. This has led to the increasing use of full-field measurements for high strain rate testing applications. With the advent of ultra-high speed imaging ($> 1 \text{ Mfps}$) it is now possible to image elastic strain wave propagation in materials. This capability has in turn led to the development of the Image-Based Inertial Impact (IBII) test. The IBII test uses full-field measurements of an inertially impacted sample (edge-on impact) to extract material properties using the Virtual Fields Method (VFM). The key idea is that the full-field displacement measurements encode the strain information in space and the stress information is encoded in time through the acceleration field. This report gives a detailed description of the IBII test method. The intention is that this report can be used by researchers in the experimental mechanics community to implement the IBII test themselves while avoiding some common pitfalls. This report is divided into three sections covering the main aspects of the IBII test method: 1) design of a purpose-built gas gun impact rig for IBII testing, 2) practical implementation of the experimental method and 3) VFM theory and data processing for IBII tests. A dataset is provided at the end of this report that contains all necessary information to conduct IBII tests from plans for the gas gun impact rig through to a data processing code which can be used to analyse IBII data.

1 Introduction

Since the development of the strain gauge high strain rate materials testing has focused on the use of the split Hopkinson pressure bar (SHPB) (or Kolsky bar) apparatus. This technique has been successfully applied to many problems in high strain rate testing, for example, high strain rate plasticity in metals [1–5]. However, the SHPB technique is not well suited for testing materials that have a low wave speed (*i.e.* soft materials) or low strains to failure (*i.e.* brittle materials) [6]. The reason for this is linked to the underlying assumptions of the test methodology.

The traditional SHPB technique uses a small sample placed between two long bars with strain gauges attached to them. The gauges are located far from the interface between bar and sample allowing the bars to act like a dynamic load and deformation cell. A stress wave is imparted on one of the bars and is transmitted into the sample. Due to the impedance mismatch between the bars and the sample some of the wave is transmitted and the rest is reflected. By making a number of simplifying assumptions the strain gauge measurements on the bars can be used with one dimensional wave mechanics to infer the material properties of the test sample. A key assumption of this analysis is that the specimen must be in a state of quasi-static equilibrium (*i.e.* inertial effects in the sample are neglected such that the force on the sample from the input and output bars are equal). For this assumption to be satisfied the specimen must be very small compared to the overall bar length and sufficient time must be allowed for the stress wave to reverberate and damp out in the specimen prior to using the strain gauge data to infer material properties. Inertial effects are most prevalent in the early portion of the test therefore it is generally accepted that

for most materials elastic properties cannot be accurately obtained with this technique [6, 7]. The assumption of quasi-static equilibrium is particularly critical when testing brittle or quasi-brittle materials in tension. The reason for this is that these materials exhibit small strains to failure and can fail before inertial effects have adequately damped out. As an example of this for the transverse tensile properties of composites this assumption typically limits the strain rate to well below 1000 s^{-1} [8].

An additional problem with the tensile SHPB technique is the accurate measurement of the sample strain. In an early study by Melin and Asp they used Moiré photography to show that the SHPB analysis was significantly underestimating the strain for the transverse tensile properties of a unidirectional composite material [8]. Similar issues with accurate strain measurement have been reported for tensile testing of metals [5] and adhesives [9] with the SHPB. In order to obtain accurate strain measurements these studies have focused on using full-field measurements in conjunction with the standard SHPB analysis. However, these studies have remained relatively conservative, using the traditional Hopkinson bar analysis and assumptions with the full-field measurement system acting as supplementary information.

The use of full-field measurements opens up completely new possibilities for designing tests that are not constrained by assumptions of the traditional SHPB method. Here we quote Gilat et al. [10] “In the past, the use of the SHB technique was limited for testing specimens undergoing uniform deformation. The introduction of 3D image correlation for measuring the full strain field on the surface of the specimen provides means for developing new types of experiments with the SHB technique in which the deformation in the specimen is intentionally not uniform.”. The purpose of the IBII test is to take this one step further and use ultra-high speed imaging as both the force and strain sensor and replace the Hopkinson bar apparatus with a stress wave imparted by impacting the sample with a projectile. The underlying idea of the IBII method is to obtain temporally resolved displacement fields and numerically differentiate them to obtain the acceleration and strain fields. The acceleration and strain fields are then combined with the Virtual Fields Method (VFM) to extract material properties. In this way the acceleration fields act as a dynamic load cell and additional measurement of external force is not required. All the required information for identification is contained within the camera images.

An initial validation of the IBII test method was published in [11] where the elastic modulus of a non-strain rate sensitive material (quasi-isotropic composite) was successfully identified. Later studies have shown that the IBII test is well suited to testing materials that are particularly challenging for the traditional SHPB technique, such as the transverse tensile properties of unidirectional composites [12], the interlaminar tensile properties of composites [13] and the tensile properties of tungsten carbide cermets [14].

The purpose of this report is to describe the IBII method with a level of detail that is not possible in a standard journal article. The idea is that someone with basic knowledge of full-field measurements could use the report to wholly replicate the IBII method as described in [12–14]. This report is divided into three main parts. The first part (Section 2) covers the design and construction of a gas gun impact rig specifically for IBII testing. Those who already have suitable loading apparatus (*e.g.* a gas gun or Hopkinson bar with the output bar removed) may want to skip this section and go straight to the second section of the report. The second section of the report gives a detailed account of the experimental implementation of the IBII test. This section covers everything from sample preparation through to running the test to obtain high quality raw images. The third and final section of the report covers the theory and data processing procedures required to extract material properties from the images. The authors hope that as the IBII test methodology starts to become more widely used this report will serve as a useful reference for those wanting to implement the test method themselves. Before delving into the main report a brief overview of the IBII test method is given to put the remaining sections in context.

1.1 Overview of the Image-Based Inertial Impact (IBII) Test

The principle behind the IBII test is relatively simple, a flat rectangular sample is struck with a projectile on its through-thickness edge to impart a stress wave and during the test the sample is imaged using an ultra-high speed camera. A pattern is placed on the surface of the sample such that the displacement field can be extracted from the raw images. From the displacement field both the acceleration and strain fields can be obtained by numerical differentiation. The kinematic fields are then processed with the VFM to extract the material properties. The interested reader is referred to [15] for a full description of the VFM theory. A detailed description of the application of the VFM to the IBII test is given in references [11–14].

A general schematic of the IBII test configuration is shown in Figure 1. For practical implementation of the IBII test a waveguide is added between the sample and the projectile. The purpose of the waveguide is to transmit an even pulse into the sample and mitigate the effects of any small misalignments between the projectile and the waveguide. This is done by taking advantage of the Saint Venant effect in dynamics as described in [16]. In this way, the waveguide acts in a similar manner to an end tab used for a quasi-static test. The waveguide also provides a convenient means of holding the sample in the impact chamber without compromising the free boundary conditions on all specimen edges apart from the contact with the waveguide.

Due to the limited size of the pixel arrays of typical ultra-high speed cameras (*e.g.* Shimadzu HPV-X / X2 with 400×250 pixels) the grid method has been used for full-field measurement in previous studies using the IBII test [11–14]. This is because the grid method offers an improved trade-off between spatial resolution and measurement resolution when compared to digital image correlation [17]. The main drawback of the grid method is that a regular pattern needs to be deposited on the sample surface. However, recently a new technique for directly printing grids onto the surface of the sample has been developed (as described in [13]). A review article describing the theory and applications of the grid method can be found in [18]. More detail on grid production and image capture during the experiment is given in the second part of this report (Section 3. For now it is useful to keep in mind that the practical aspects of imaging the sample during impact places constraints on the design of the experimental apparatus, as described in the following section.

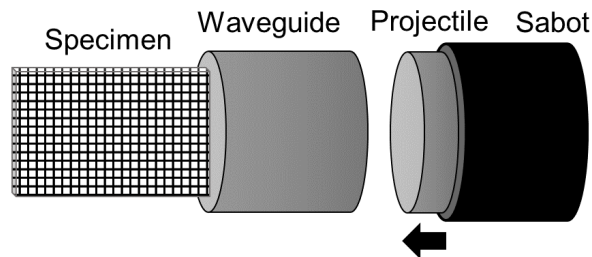


Figure 1: Schematic of the main components used in the Image-Based Inertial Impact (IBII) test.

2 Impact Rig Design

2.1 Design Specification

The following design specification outlines the main requirements for the experimental apparatus to implement the IBII test:

1. Maximum velocity of 100 m.s^{-1} - [11] showed that impact speeds of only 30 m.s^{-1} produced a compressive stress of 300 MPa at a strain rate of $\sim 2000 \text{ s}^{-1}$ in a quasi-isotropic composite

sample. Thus, a maximum impact velocity of 100 m.s^{-1} for the heaviest projectile will be more than sufficient to test most materials at strain rates on the order of 1000s of s^{-1} .

2. Bore size of 50 mm - Practically, it is easier to produce grids of pitches of approximately 1 mm . Given the size of the pixel array of the Shimadzu HPV-X camera ($400 \times 250 \text{ pixels}$) and sampling at 5 pixels/period to achieve maximum spatial resolution there will be 80×50 grid lines. With a grid pitch of 1 mm the field of view of the camera will be $80 \times 50 \text{ mm}$. Thus, a bore of 50 mm is preferred. This is also favourable to ensure that the tested specimens are large enough to be representative, covering for another weakness of the SHPB methodology that requires the use of very small specimens.
3. Maximum floor space of $4.7 \times 2 \text{ m}$ - this is specified based on the available floor space in the laboratory while allowing for adequate optical access on both sides of the rig.

2.2 Projectile Acceleration Method

Several different mechanisms of projectile acceleration were considered including gravity ('drop' systems), chemical / explosive, elastic ('bungee' chord systems) and pressurised gas. The gravity and elastic options were discounted as it would be difficult to achieve the required velocity using these methods. As the impact rig would be housed in a shared laboratory space the chemical / explosive option was discounted for safety reasons. Thus, a pressurised gas system was selected as this could be interfaced with the existing laboratory compressed air supply for convenience. This would also allow for transferability of the design as many mechanical testing laboratories already have compressed air supplies at similar pressures.

2.3 Idealised Gas Gun Design

The idealised design calculations for single-stage gas guns operating at low speeds are described in [19, 20]. These calculations make the assumption that the work done by adiabatic expansion of the compressed gas is converted into kinetic energy of the projectile. At higher projectile speeds shock effects in the working gas need to be accounted for as described in [21, 22]. Here the low speed design approach is suitable as the maximum design velocity is only 100 m.s^{-1} . The main result of this idealised analysis relates the projectile velocity to the design variables of the gas gun system as follows:

$$v_p = \eta \sqrt{\frac{2P_0V_0}{m_p(\gamma - 1)} \left[1 - \left(\frac{V_0}{V_0 + A_b L_b} \right)^{\gamma - 1} \right]} \quad (1)$$

where v_p is the projectile velocity and m_p is the projectile mass. The reservoir pressure is denoted P_0 and the volume of the reservoir is given by V_0 . The length of the barrel is given by L_b and the cross sectional area of the barrel is A_b . The adiabatic index is given by γ and is taken as 1.4 for dry air. Finally, η is the efficiency of the system accounting for losses such as friction in the barrel, air escaping around the projectile due to an imperfect seal *etc.*. Note that the derivation of this relationship is given in [20] so it will not be re-iterated here.

Equation 1 outlines the main design variables for a compressed gas gun system including the maximum pressure and volume of the pressurised cylinder, the length and cross sectional area of the barrel and the mass of the projectile. Selection of these and other design variables will be discussed in the following sections.

2.4 Barrel

As previously mentioned the bore size of the barrel is already specified at 50 mm based on practical constraints on the specimen size. As for the barrel length, it is desirable to have a longer barrel

as this increases the distance over which the pressurised gas can accelerate the projectile leading to higher projectile velocities. Given the available length of floor space at 4.7 m the longest barrel possible is 3 m. This allows for 1 m to house the working section and capture chamber and 0.7 m for the pressure vessel and firing valve.

The barrel was machined from a single piece of EN24T steel by a specialist deep hole boring machinist. The wall thickness of the barrel is 10 mm and the inner surface is honed to Ra 0.5 μm . To interface the barrel with standard pneumatic components a standard PN20 flange (rated to 20 bar) was machined on both ends of the barrel. The other advantage of using a standard flange is that it would allow for future modification of the system to accommodate other firing mechanisms such as burst discs.

2.5 Projectile and Sabot Design

In [11] a steel projectile of similar length to the sample was used to generate a single compressive load and unload. Based on equation 1 the limiting velocity for the gas gun system will be for the heaviest projectile that needs to be accelerated to the design velocity ($v \propto 1/\sqrt{m}$). Thus, projectile 1 in Figure 2 (a) will be considered here.

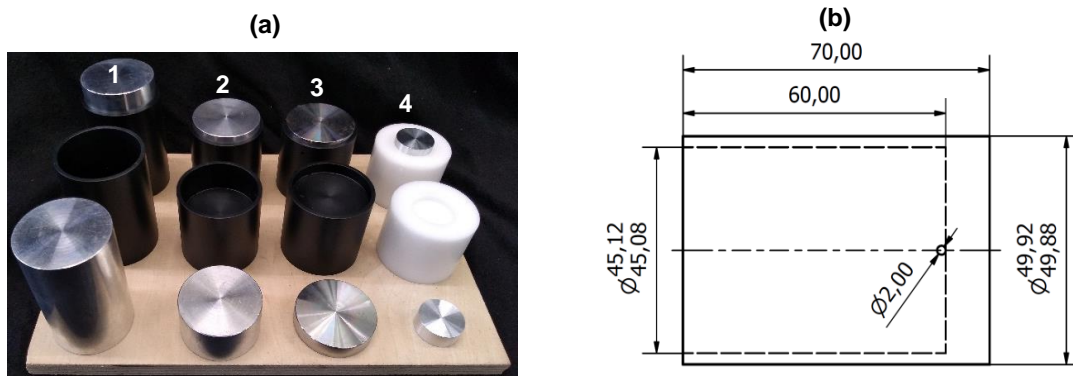


Figure 2: (a) Various projectiles used for different tests: 1 standard compressive projectile; 2 transverse tension testing of composites [12]; 3 tension testing of tungsten carbide [14] and 4 intralaminar tensile testing of composites [13]. (b) Delrin sabot design drawing for projectile 1, dimensions in mm.

Metal projectiles need to be encased in a plastic sabot to reduce friction and prevent damage to the barrel. The required wall thickness for the sabot is 2.5 mm meaning the maximum diameter of a metal projectile is 45 mm. In order to match the aspect ratio of the camera the field of view will be 72×45 mm. Thus, the longest projectile required for testing will be 72 mm. For general purpose testing aluminium 7075-T6 is used as the quasi-static yield stress of this material is on the order of 500 MPa. This allows a compressive pulse of up to 500 MPa to be input into the test sample without yielding the projectile and clipping the input pulse.

Initially the sabots were made from oil filled nylon. However, this material is prone to atmospheric water absorption and given the tight tolerance of the sabot in the barrel the sabots would eventually swell to the point where they were unusable. More recently, the sabots have been machined from an acetal polymer with the trade name Delrin which does not suffer from the same water absorption issues. This allows the sabots to be machined in batches and stored for extended periods of time.

A dimensioned schematic of the sabot is shown in Figure 2 (b). A relief hole is added at the base of the sabot which allows the projectile to be pressed into place without trapping air between the projectile and the base of the sabot. Based on the dimensions of each component the volume can be calculated and mass determined using the density of each material. For this purpose the following densities were used: aluminium 7075-T6 $2800 \text{ kg}\cdot\text{m}^{-3}$ and Delrin $1410 \text{ kg}\cdot\text{m}^{-3}$. For the

Delrin sabot shown in Figure 2 (b) the total mass is 0.06 kg and for an aluminium projectile the mass is 0.32 kg . Thus, a combined projectile mass of 0.38 kg which will be used in equation 1 to determine the theoretical performance of the gas gun system.

In order to test a variety of materials different projectiles are required, longer projectiles will produce longer input pressure pulses. Shorter projectiles are required for spall type tests which use the reflection of the pulse to cause tensile failure of the sample. For example in [12] aluminium projectiles of 25 mm length were used for testing carbon fibre in transverse tension and in [14] steel projectiles of 10 mm length were used to test tungsten carbide in tension. A photograph of the different projectile designs are shown in Figure 2 (a).

2.6 Pressure Vessel

The nominal maximum pressure of the compressed air supply in the laboratory is 8 bar . Thus, a design pressure of 8 bar will be assumed to achieve the maximum velocity of 100 m.s^{-1} . The volume of the pressure vessel must also be sufficient such that the pressure accelerating the projectile does not drop significantly as compressed gas is evacuated from the chamber. If the efficiency term in equation 1 is set to $\eta = 1$ then the pressure P_0 can be expressed as a function of the volume V_0 :

$$P_0 = \frac{m_p v_p^2 (\gamma - 1)}{2V_0} \left[1 - \left(\frac{V_0}{V_0 + A_b L_b} \right)^{\gamma - 1} \right]^{-1} \quad (2)$$

Here we take the heaviest projectile mass of $m = 0.38 \text{ kg}$ and the maximum possible barrel length of $L_b = 3 \text{ m}$. Figure 3 plots equation 2 over a range of reasonable pressure vessel sizes from 1 L to 30 L and projectile velocities from 20 m.s^{-1} to 100 m.s^{-1} . This shows that for pressure vessel volumes above $15 \times 10^{-3} \text{ m}^3$ there is minimal change in the required pressure for a given projectile velocity. Therefore the pressure vessel volume was set at $V_0 = 20 \text{ L}$.

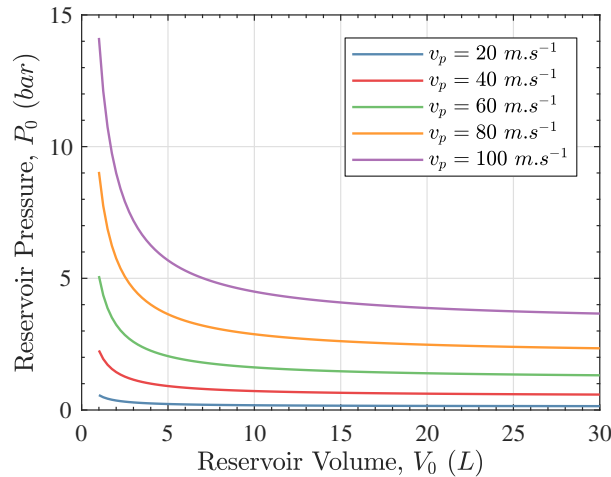


Figure 3: Relationship between the reservoir pressure and reservoir volume showing that the required volume for a given projectile velocity converges at 15 L .

2.7 Firing Valve

There are several options for firing valves for gas gun systems. Designs for burst disc systems have been used on high speed gas guns [21, 23] as well as the wrap-around method which uses the projectile itself to seal the pressure vessel and act as a trigger [24]. However, for low-speed gas gun designs electro-pneumatic solenoid valves are favoured due to their ease of use [19, 20, 22]. Therefore, a solenoid valve was used as the firing mechanism for this design.

The main issue with using a solenoid valve for a large bore gas gun is that the opening time of the valve is linked to the valve orifice size. Specifically, smaller solenoid valves tend to have faster opening times than larger valves. If the valve opening time is too slow then the projectile can exit the barrel before the valve has fully opened. Another important parameter when selecting a valve is the discharge coefficient C_d . The discharge coefficient is a dimensionless number that describes the ratio of the actual mass flow rate to the theoretical mass flow rate through a valve. Thus, the discharge coefficient is always less than 1.

To investigate the effects of different firing valve characteristics such as the valve opening time and orifice size a pneumatic Simulink model was developed in Matlab (v2017a). The block diagram for this Simulink model is shown in Figure 4. The associated Matlab code for this model is provided in the dataset detailed at the end of the manuscript. A constant pressure source is used to model the pressurised air supply that is used to fill the pressure vessel. The firing valve and fill valve are modelled as variable area pneumatic orifices. The effective area of the firing valve orifice is modelled as linearly increasing over the valve opening time with a limit of the valve orifice size. The barrel of the gas gun is modelled as a pneumatic piston with a mass attached to the piston acting as the projectile. A translational motion sensor is then used to extract the velocity and displacement of the projectile with the desired output being the velocity of the projectile when it has been displaced by the length of the barrel.

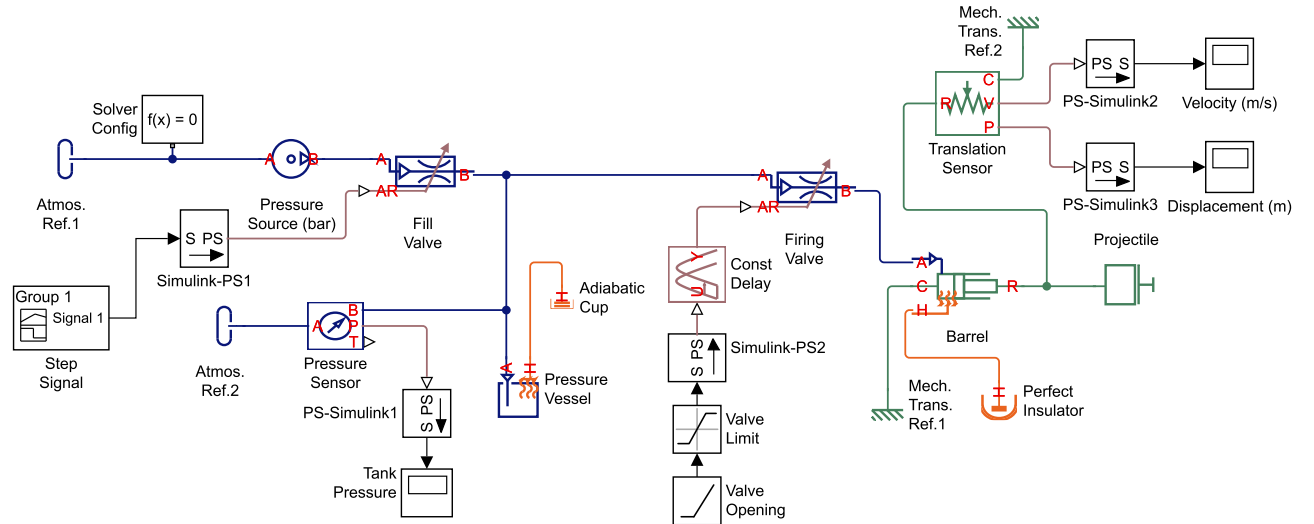


Figure 4: Gas gun Simulink model to investigate the effects of firing valve orifice size and opening time.

The Simulink model runs in two stages. The first stage pressurises the pressure vessel and the second stage releases the pressure into the piston ‘firing the gun’. The first signal is a 0.25 s long step pulse sent to the fill valve at $t = 0$ s. This allows the pressure vessel to be ‘filled’ to the same pressure as the constant pressure source. Then a constant delay is used such that the opening signal is sent to the firing valve at $t = 0.5$ s with the total simulation time being 1 s. The model is then run in a loop with various pressure source values to extract the velocity versus pressure curve for a given configuration.

For analysis of the solenoid valve characteristics all variables were fixed apart from the valve opening time and the valve orifice size. The fixed input parameters for the model are listed in Table 1. The discharge coefficient of the firing valve was assumed to be $C_d = 0.5$. Based on a collection of solenoid valve data sheets from [25], for solenoid valves with up to 12.5 mm orifice sizes a 20 ms maximum opening time is expected while for valves up to 25 mm an opening time of 50 ms is expected. Finally, for larger valves up to 50 mm a 200 ms opening time is given. Based on this data the Simulink model can be used to predict the pressure velocity curves for each given valve configuration as shown in Figure 5.

Table 1: Design parameters for the gas gun system.

| | |
|----------------------------------|-----------------------------------|
| Barrel Bore, D_b | 50 mm |
| Barrel Area, A_b | $1.96 \times 10^{-3} \text{ m}^2$ |
| Barrel Length, L_b | 3 m |
| Projectile Mass, m_p | 0.384 kg |
| Design Pressure, $P_{0,max}$ | 8 bar |
| Pressure Reservoir Volume, V_0 | 20 L |

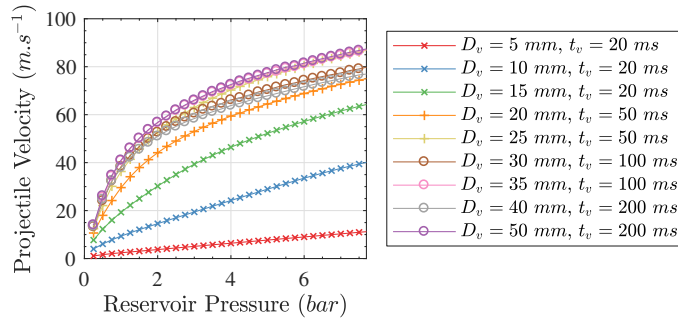


Figure 5: Predicted pressure/velocity performance curves from the Simulink model for various firing valve diameters D_v and valve opening times t_v .

The general trend in Figure 5 shows that the larger valves tend to have better performance despite the longer opening times. The best performing valve is the 50 mm diameter valve with a 200 ms opening time. However, the 25 mm diameter valve with a 50 ms opening time has similar performance illustrating the trade-off between opening time and orifice size. Based on this result a CS Fluid Power SA50 valve was selected and purchased from [25]. This valve has a discharge coefficient of $C_d = 0.64$ for an orifice size of 50 mm. The maximum working pressure of the valve is 20 bar for air. The opening mechanism of the valve is pressure assisted and therefore 0.5 bar of back pressure is required for the valve to open. The maximum opening time of this valve is given by the manufacturer as 200 ms. The specific performance of the selected valve will be discussed in the following section.

2.8 Predicted Gas Gun Performance

Using the design variables detailed previously in equation 1 can be used to estimate the performance curve of the gas gun system (pressure against velocity). This can then be compared to the predictions of the Simulink model. The design variables used for this comparison are listed in Table 1 and the characteristics of the solenoid valve were taken as those of the selected valve in the previous section. The comparison of the two models is shown in Figure 6 including three efficiency levels for the ideal model ($\eta = 0.5, 0.75, 1$).

Based on the results in Figure 6 the Simulink model predicts results similar to the case of $\eta = 0.75$ for the ideal model. However, the shape of the pressure velocity curve predicted by the Simulink model is quite different to the ideal model. The simulink model and the ideal model with $\eta = 0.75$ both predict maximum velocities close to the design velocity of 100 m.s^{-1} therefore the selected configuration can be expected to satisfy the design specification.

2.9 Pneumatic Control System

The pneumatic control system has two main functions, 1) control pressurisation and firing of the gas gun and 2) operate the safety interlocks. A schematic of the main components of the pneumatic control system is shown in Figure 7.

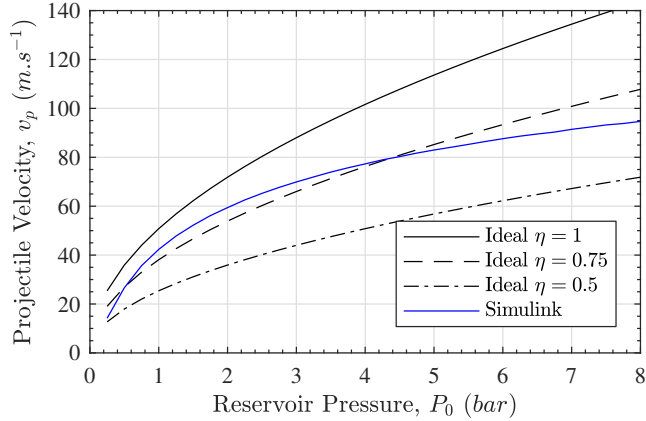


Figure 6: Comparison of the predicted performance from the ideal gas gun model (equation 1) and the Simulink model. For the ideal model three different efficiencies are shown $\eta = 1, 0.75, 0.5$.

There are three main safety interlocks on the impact rig. The first interlock is on the door of the capture chamber, the second is on the flange which acts as the breech of the gas gun and the third is emergency shut down switch that acts like a ‘safety-catch’. All interlocks must be closed before a master relay is triggered which allows the relays for each solenoid valve to operate. Both solenoid valves were selected to be ‘normally closed’ (*i.e.* closed by default with power required to open) such that if power is cut then there was no possibility of an accidental firing. Apart from the electronic components the pressure vessel is also fitted with a manual drain valve and manual pressure gauge such that the pressure can be safely drained without having to fire the gun. Finally, the pressure vessel is fitted with a spring loaded automatic pressure release valve which will activate if the pressure vessel exceeds the design pressure.

As can be seen in Figure 7 an additional solenoid valve is coupled with an electronic pressure sensor to control the filling of the pressure vessel. A Shako PU225H valve was sourced from [25] and an Efactor500 PU5403 pressure sensor was sourced from RS Components (<https://uk.rs-online.com/web/p/products/8353923/>) were used for this purpose. The main control of the pressurisation and firing systems occurs through a National Instruments NI USB-6211 data acquisition system. A Labview graphical user interface program was written to control the pressurisation and firing sequence of the system. Figure 8 shows a programming flow chart of the pneumatic control program. The Labview program is also provided in the dataset detailed at the end of the manuscript.

2.10 Frame, Breech and Capture Chamber

The frame for the gas gun was designed using standard steel sections with the barrel being mounted along an I-beam. An annotated photograph of the main I-beam section is shown in Figure 9 (a). The legs of the I-beam are bolted to the concrete floor with metal shims placed under each set of legs such that barrel and I-beam are mounted level. The legs supporting the I-beam near the working section and capture chamber were deliberately spaced further apart to allow for ease of positioning tripods for the camera and flash.

Due to practical constraints it was decided that a breech loading design would be most suitable. This would avoid the possibility of accidentally bumping the specimen once it had been aligned with the camera while muzzle loading the gun. Therefore the pressure vessel was mounted on low friction rails such that the pressure vessel could be moved to open the flange joining the pressure vessel and the barrel. A photograph of the breech loading mechanism is shown Figure 9 (b).

The canopy over the working section of the gas gun can be rolled back over the capture chamber to allow a specimen to be mounted, as shown in Figure 9 (c). Once the sample is in place and the camera is aligned the canopy encloses the test section with a polycarbonate window allowing for

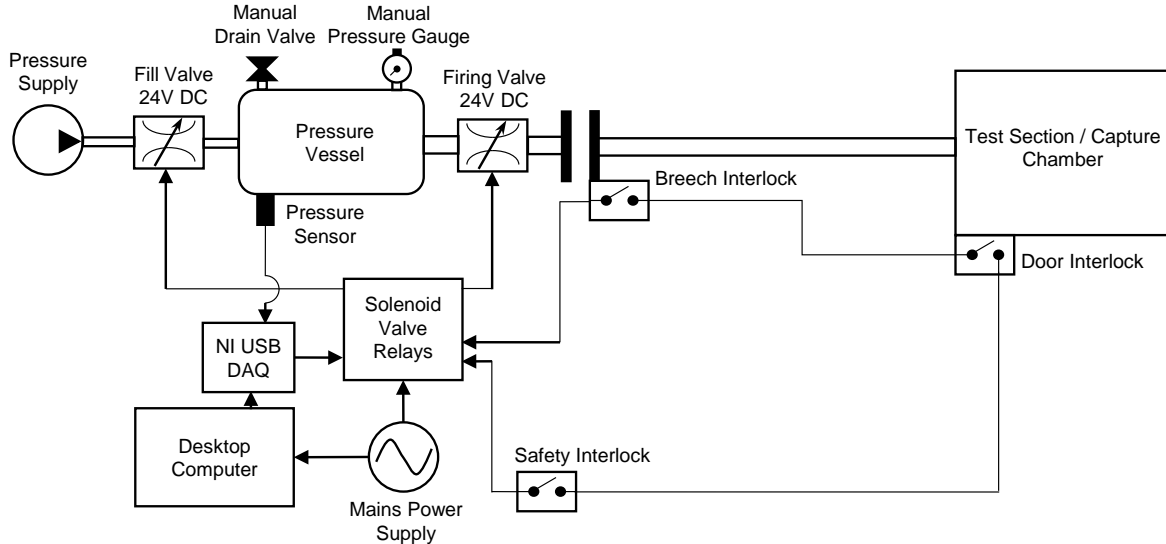


Figure 7: Pneumatic control system schematic showing the main safety interlocks and interface connections between the electronic and pneumatic components.

optical access. The capture chamber at the end of the I-beam is loosely packed with cardboard and scrap shredded fabric to safely decelerate impact debris after the test.

2.11 Projectile Speed Measurement

A projectile speed measurement system was developed using infra-red light gates coupled with an Arduino Uno micro controller. The infra-red gates used for this purpose were Honeywell SPX 1189 sensors. Initially, the voltage response of the light gates was analysed using an oscilloscope. This revealed that when the infra-red beam was broken the signal from the photo detector exponentially decayed whereas when the photo sensor was exposed again the signal was almost square. Thus, to improve accuracy of the speed measurement the light gate system was triggered from the rising edge of the light gate signal. For this case the projectile will first break the gate (with an exponentially decaying signal) and then once it has passed and the sensor is re-exposed (producing a more square signal) the timing signal will be recorded. Note that Arduino code is provided in the dataset detailed at the end of the manuscript.

The light gates were mounted just ahead of the barrel exit such that the projectile would be in free flight once the speed measurement was taken. The nominal spacing of the light gates was 40 mm. To calibrate the speed measurement system the effective spacing between the light gates was inferred by tracking the free flight of the projectile using an ultra high speed camera. This was achieved using a Shimadzu HPV-X recording 256 images at 200,000 fps. A REL SURE Bright LED panel was used for continuous illumination (<http://www.relinc.net/sure-bright-led-lighting-system/>). An initial set of calibration images was taken with the HPV-X to obtain the pixel to length calibration as 0.115 mm/px. The front of the projectile was then tracked using the subpixel edge detection algorithm described in [26]. The position of the projectile was then plotted against the recording time and linearly fitted to obtain the average velocity. The timing between each light gate signal was also recorded and by comparing this to the speed measured using the images an effective light gate spacing was calculated. The results of this analysis are summarised in Table 2. Therefore, an effective light gate spacing of 38.3 mm was determined by taking the average of the three runs. Using the average effective light gate spacing the uncertainty in the velocity measurement can be estimated by taking the maximum error from all three shots. Shot 2 has the largest error at -0.14 m.s^{-1} giving an estimated uncertainty of $\pm 0.4\%$ at this pressure.

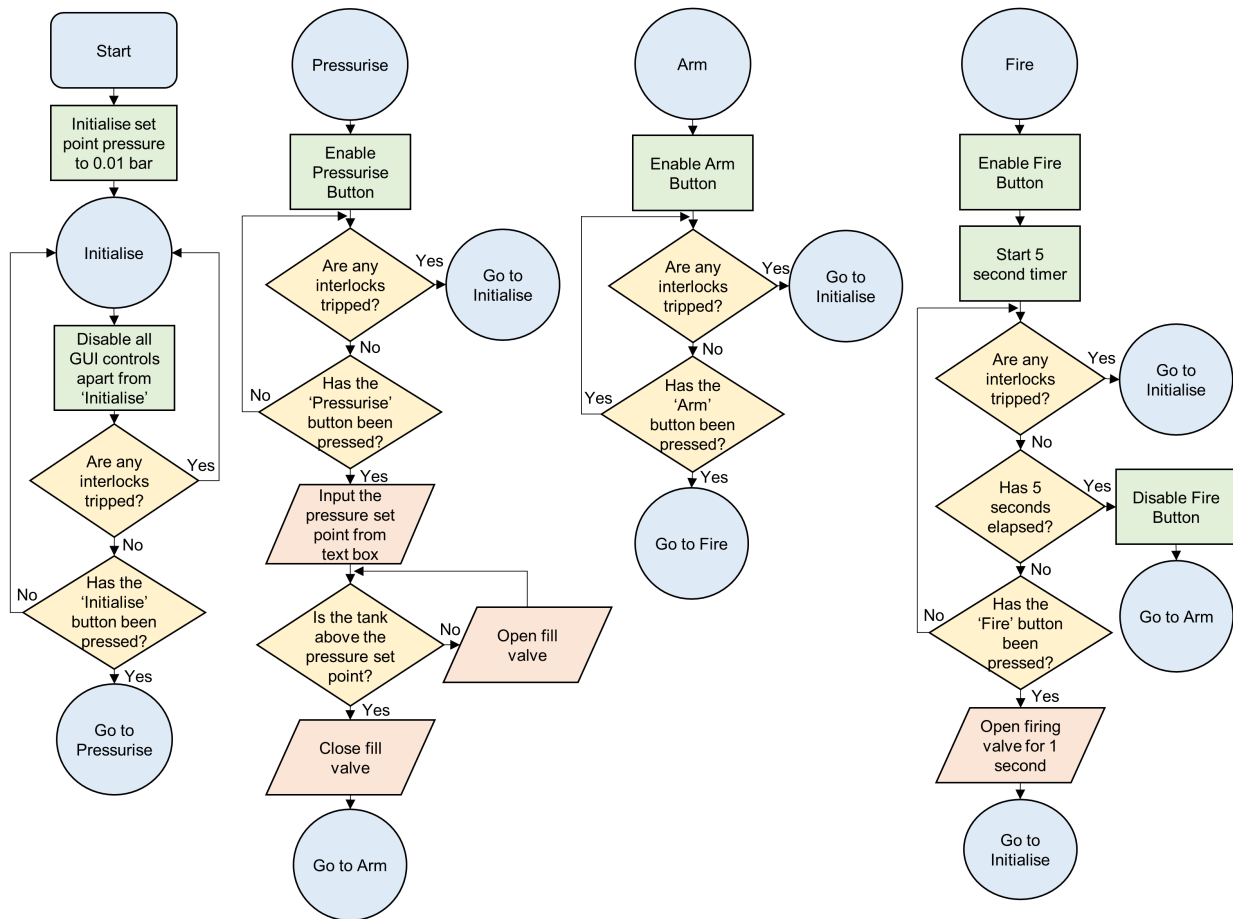


Figure 8: Program flow chart for the Labview based pneumatic control system.

2.12 Gas Gun Performance

A series of tests was carried out to compare the performance of the real gas gun system to that predicted using the models described previously. Six shots were conducted at each pressure from 0.65 to 4.0 *bar*, apart from 4.0 *bar* where only three shots were conducted. Figure 10 shows all shots with the real gas gun system compared to the ideal and Simulink models. Note that the design parameters for the ideal and Simulink model are summarised in Table 1.

There are some significant differences between the predictions from both models and the real performance of the gas gun system. The ideal model does not seem to replicate the performance of the gas gun system and tends to over predict the projectile velocity at low pressure and under predict the velocity at high pressure. The Simulink model more closely replicates the overall shape of the curve which seems to be linked to the opening time of the firing valve. However, the Simulink model still over predicts the performance of the gas gun system. Part of the difference for both models can be attributed to the solenoid valve having a pressure assisted opening mechanism. This means that the valve requires 0.5 *bar* back pressure to open (and stay open) whereas both models assume that the valve will open regardless of the back pressure. It is interesting to note that shifting the predicted performance curve of the Simulink model by +0.5 *bar* (see Figure 10) closely matches the real performance of the gas gun system. Other differences between the models and the performance of the real gas gun can be attributed to losses in the system that are not captured by either model such as friction in the barrel and loss of air around the projectile due to an imperfect seal.

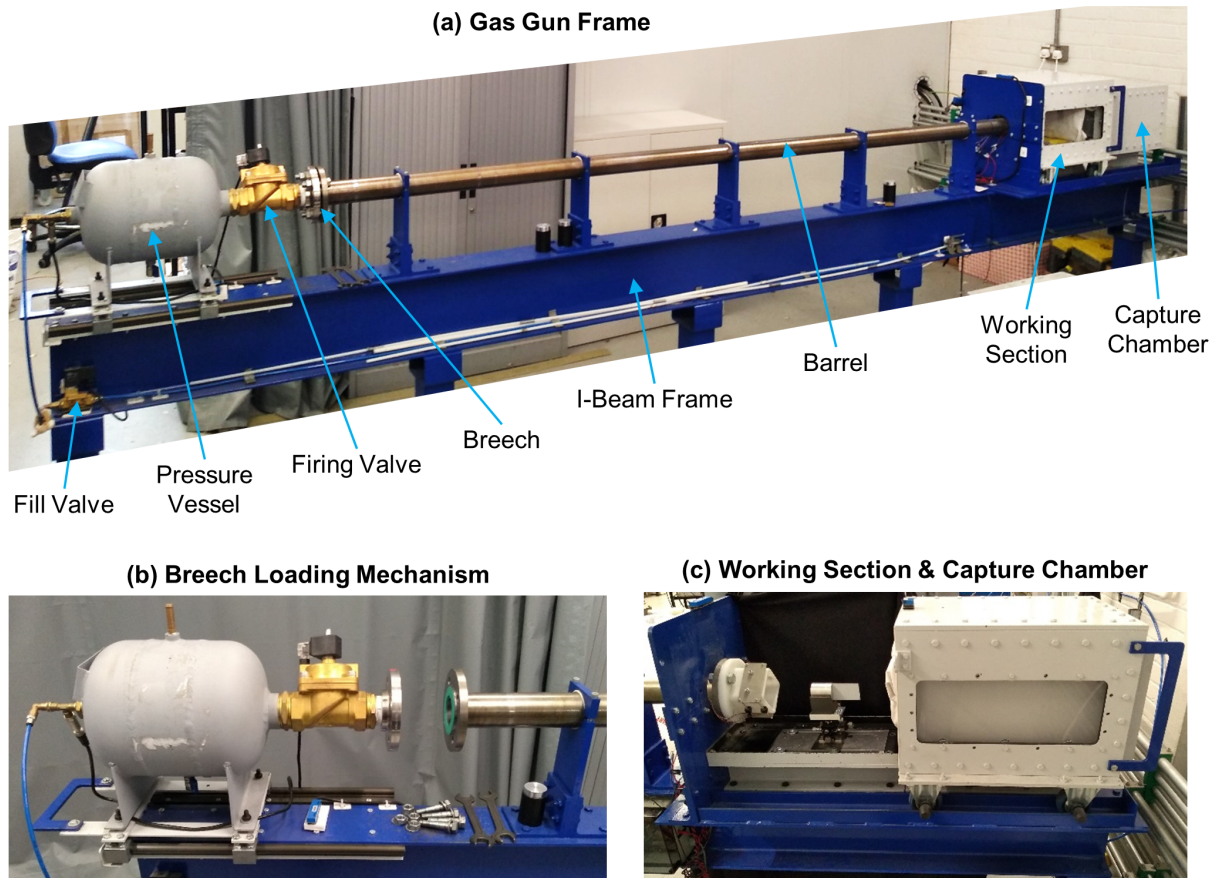


Figure 9: (a) Annotated photograph of the gas gun system, (b) close up of the breech loading mechanism in the open position and (c) close up of the working section and capture chamber with the canopy rolled back over the capture chamber.

2.13 Design Modifications and Alternative Apparatus

Based on the design presented here and experience gained through our previous test campaigns [12–14] it would be possible to produce a much more compact design that is still capable of performing IBII tests on most materials. For most cases impact speeds up to 60 m.s^{-1} are more than sufficient (see [14] where a $\sim 200 \text{ kN}$ pulse was generated with an impact speed of 55 m.s^{-1} which was used to spall tungsten carbide with a tensile stress of $\sim 1.2 \text{ GPa}$). Additionally, for the case of tensile spall testing lighter projectiles are generally used. Therefore, a much shorter barrel (on the order of 1 m long) could be used and still achieve the required velocity for testing most materials. This would greatly reduce the overall footprint of the system and make it much closer in size to a standard mechanical testing machine. We are currently in the process of implementing a smaller bench top IBII test rig that will be housed in a Class 2 biohazard laboratory for testing biological samples.

It is also worth noting that it is possible to use other impact apparatus to perform IBII tests such as a drop tower or split Hopkinson pressure bar. For example the implementation described in [27] used a Hopkinson bar to supply the loading to the test samples in a spall-like configuration providing a free edge to allow for the analysis of the data. As long as the general assumptions of the IBII test (through-thickness homogeneity and plane stress) are valid the loading apparatus can be anything that provides an inertial loading to the sample.

Table 2: Light gate effective spacing calibration using three shots at 1.2 *bar*.

| Shot Num. | Speed HPV-X ($m.s^{-1}$) | Light Gate Time (μs) | Effective Light Gate Spacing (mm) |
|-----------|----------------------------|-----------------------------|---------------------------------------|
| 1 | 32.9 | 1160 | 38.2 |
| 2 | 32.3 | 1192 | 38.5 |
| 3 | 32.7 | 1172 | 38.3 |

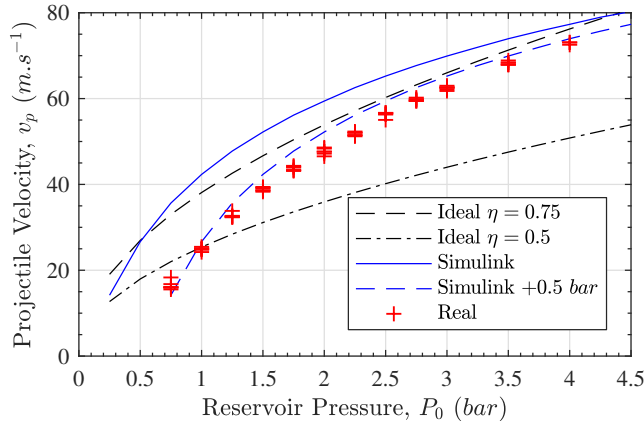


Figure 10: Comparison of the real performance of the gas gun system with the predicted performance from the ideal and Simulink models. For the ideal model two different efficiencies are shown $\eta = 0.75, 0.5$.

3 Experimental Implementation

3.1 Specimen Mounting and Alignment

The waveguide is mounted in front of the gas gun barrel on a wedge shaped foam stand as shown in Figure 11 (a). The foam stand is attached to an aluminium tray using double sided tape. The aluminium tray is mounted on a series of translation and rotation stages as shown in Figure 11 (b). The translation and rotation stages allow for ease of alignment of the waveguide with the gas gun barrel.

The following steps outline the entire alignment procedure for the IBII tests. Image analysis is used to quantify the misalignment between the waveguide and projectile at impact to within 1 *pixel* (0.2 *mm* positional accuracy). Experiments have shown that this level of alignment is sufficient to ensure two-dimensional loading over much of the sample for consistent stiffness and strength measurements. The alignment is performed in two phases: 1) side-on alignment to correct for pitch and vertical offsets (Figure 12 (a)), and 2) top-down alignment using a mirror system to set the waveguide yaw and out-of-plane position (Figure 12 (b)). The procedure for mounting the waveguide and aligning it with the projectile is given below.

1. Attaching the waveguide to the foam stand: The waveguide is stood upright on a flat surface (copper contacts facing up) and a 1 *mm* metal shim is placed underneath the waveguide. Two pieces of double sided tape are placed on the faces of the ‘V’ of the foam stand. The ‘V’ shape of the foam stand is then pushed into place on the waveguide while it is standing upright. The purpose of the shim is to ensure that the face of the waveguide is 1 *mm* in front of the stand allowing the top and bottom edges to be viewed for alignment. The double sided tape used to attach the waveguide to the stand ensures that the waveguide is not displaced by air exiting the gas gun barrel (this is not normally a problem for the standard 45 *mm*

waveguides however, for the small 25 mm diameter waveguides this was found to be useful). The waveguide and foam stand can now be placed on the mounting tray as shown in Figure 11 (c). Double sided tape should be used to attach the foam stand to the mounting tray such that the waveguide is held securely in place.

2. Approximate waveguide positioning using an alignment rod: The waveguide is aligned with the barrel using a precision machined Delrin rod placed inside the barrel. The rod is 370 mm in length and the main part of the rod is machined to closely match the inside tolerance of the barrel (49.95 ± 0.01 mm) with one end of the rod being machined to the same diameter as the projectile (nominally 45 mm). Initially, the waveguide is moved with the translation stages such that it is approximately aligned with the rod mounted in the barrel. Both the pitch and yaw angles are then adjusted using the rotation stages. The rotational alignment is verified by back illuminating the contact between the alignment rod and waveguide with an LED flash light. The rotation stages are then adjusted until no light is observed between the contact of the alignment rod and the waveguide. Once the angular alignment is complete the translation stages are used to complete the alignment of the waveguide. Figure 11 (c) shows the alignment rod mounted in the barrel with the waveguide following the alignment process. The pitch angle of the wave guide is also verified using a spirit level as shown in Figure 11 (d).
3. Side-on alignment shots: The camera is placed with a side-on view (see Figure 12 (a)) such that the diameter of the projectile (typically 45 mm) fills most of the vertical field of view (normally 225 pixels) giving a resolution of ~ 0.2 mm/pixel. The position of the top and bottom of the waveguide is then determined to the nearest pixel on a series of static images using ImageJ. A projectile is then fired at the waveguide and the impact is recorded with the location of the top and bottom of the projectile being determined to the nearest pixel. Normally, this is done at a frame rate of 500 kfps with a 50 frame pre-trigger. The pre-trigger allows the vertical position of the projectile and waveguide to be measured before and after impact. Based on the vertical and pitch angle misalignment of the waveguide (extracted with ImageJ) the translation and rotation stages are adjusted. Here it is easiest to adjust the stages while using the ‘live view’ mode of the camera and using the pixel numbers on the image as reference points (e.g. if the top of the projectile was aligned with pixel 25 in the Y direction then the waveguide should be moved to this point). The side-on alignment should be repeated iteratively until the projectile and waveguide are aligned within 1 pixel.
4. Top-down alignment shots: The procedure for the top down alignment shots is essentially the same as the side on case however, a mirror system is used to obtain the appropriate angle of view (see Figure 12 (b)). Photographs of the mirror system are shown in Figure 13. In this case it is desirable to be able to view the length of the waveguide as angular misalignment for the top-down case can be seen as a bending motion of the waveguide post-impact. If the waveguide and projectile are properly aligned in the top-down direction the waveguide will translate in the direction of the impact without any bending motion. Again, the top-down alignment shot should be repeated until the alignment falls within 1 pixel.

3.2 Image Capture and Grid Processing

3.2.1 Ultra-high Speed Cameras

The IBII test relies on the use of ultra high speed imaging (> 1 Mfps) to resolve deformation of an impacted test sample in the mechanical wave regime. An elastic wave in the test sample propagates at the longitudinal wave speed in the material, which is typically greater than 1000 m.s⁻¹ for most engineering materials. Thus, inter-frame times of 1 μ s or less are required.

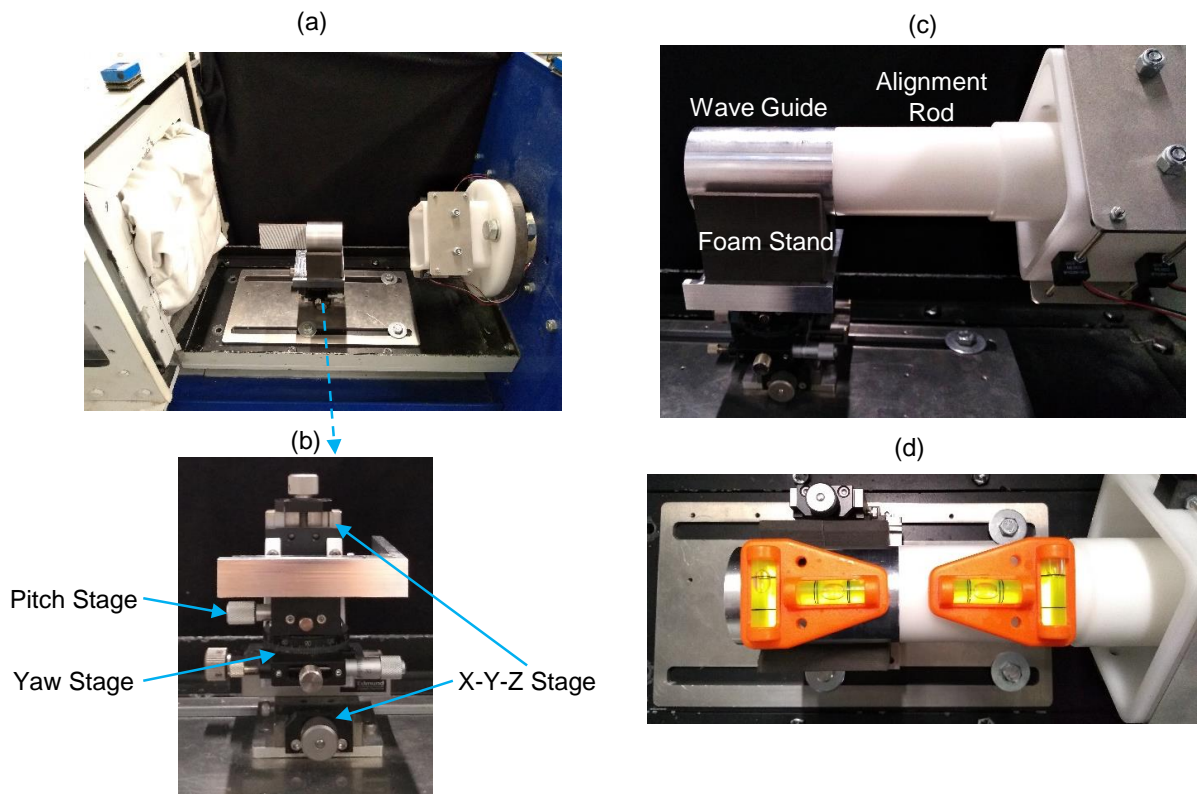


Figure 11: (a) Specimen mounted in the working section of the gas gun. (b) Close up view of the rotation and translation stages used to align the waveguide to the barrel. (c) Image of the alignment rod being used to align the waveguide. (d) Verification of the pitch alignment using spirit levels.

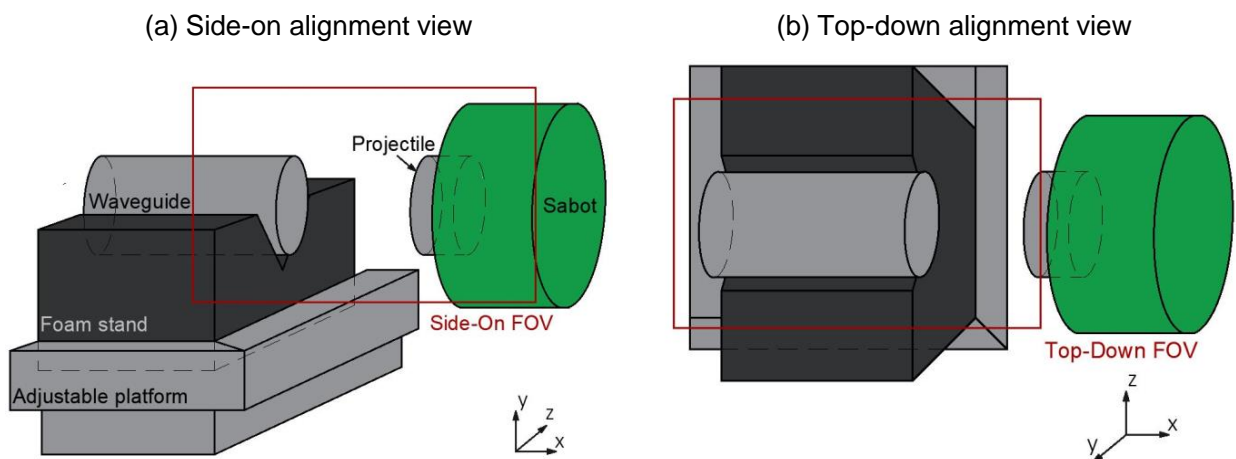


Figure 12: Schematics of two imaging perspectives used to align the waveguide with the projectile: (a) side-on alignment used to set the pitch and y-position, and (b) top-down perspective used to set the yaw and z-position.

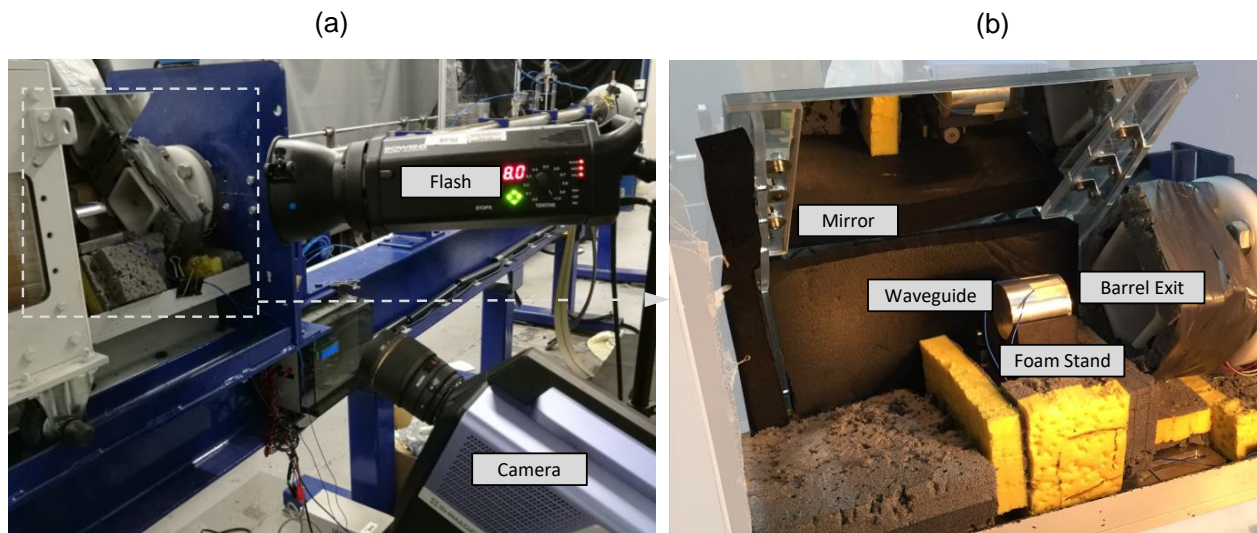


Figure 13: Mirror system installed in the capture chamber to enable visualisation of the impact in the 'top-down' perspective. (a) Mirror installed in the chamber, and (b) camera setup to visualise mirror through side windows of the test chamber

Previous implementations of the IBII test have mainly used the Shimadzu HPV-X ultra-high speed camera [11–14]. This camera has excellent image quality and low grey level noise making it ideal for full-field measurements. The main drawback of the Shimadzu HPV-X is the low pixel count (400×250 pixels). This limits the test geometry that can be used in the IBII test to relatively simple configurations that do not induce large gradients in the kinematic fields. The current successor of the Shimadzu HPV-X is the HPV-X2 which exhibits more sensitivity but higher random pixel noise¹. The pixel array size for the HPV-X2 is still limited to 400×250 pixels. The authors hope that future iterations of ultra-high speed cameras will be able to replicate the image quality of the Shimadzu HPV-X with significantly larger pixel arrays (ideally 2000×2000 pixels). This would enable much more interesting test configurations including features such as holes and notches.

There are several other ultra-high speed cameras which are potentially capable of being used for the IBII test method. The previous version of the Shimadzu camera, the Shimadzu HPV-1, was used to analyse a concrete spalling test in [27]. With the HPV-1 sensor architecture there are known issues with the low pixel fill-factor and temporal image 'flickering' that must be accounted for as described in [28, 29]. A camera system that is similar to the Shimadzu HPV-X and X2 is the Specialised Imaging Kirana. Unfortunately issues with the sensor architecture on this camera generate worse temporal 'flickering' issues than for the HPV-1 which does not enable the reliable calculation of temporal derivatives (velocity, acceleration, strain rate)¹. Other ultra-high speed camera systems such as gated intensified cameras and rotating mirror cameras can also be used. However, each of these technologies present challenges for performing full-field measurements. For gated intensified cameras the use of light intensifiers leads to significant increases in measurement noise [28, 30]. For rotating mirror cameras it is possible to achieve much higher pixel counts however, the mechanical nature of these systems leads to differences in images taken on each sensor introducing measurement errors. A rotating mirror camera was used to analyse a Hopkinson Bar experiment in [31]. For the remainder of this report descriptions of the imaging procedure will relate directly to the Shimadzu HPV-X camera which has been used in previous studies.

¹<http://photodyn.org/tools/ultra-high-speed-camera>

3.2.2 The Grid Method

The next component of the IBII test is a full-field displacement measurement technique. The most popular method for obtaining full-field displacement measurements is Digital Image Correlation (DIC). However, the grid method has been implemented in previous studies using the IBII test as it offers an improved spatial resolution when compared to Digital Image Correlation (DIC) [17]. This increase in spatial resolution is especially important due to the small pixel array size on current ultra-high speed cameras. It is possible to apply the IBII test method using any full-field displacement measurement technique as long as there is sufficient spatial and temporal resolution. Those wishing to use DIC instead of the grid method for IBII testing are strongly encouraged to consult the DIC good practice guide for experimental information specifically related to DIC [32].

The grid method will be briefly described here as it will be used in the following sections. A more detailed description of the grid method is given in the review article [18]. The basic principle of the grid method is to use a periodic pattern applied to the sample and detect changes in the phase of the pattern as the sample deforms. The change in phase between two images is then directly related to the displacement of the sample.

A windowed discrete Fourier transform algorithm is used to extract phase maps from the raw grey level images of the grid pattern. Here, a bi-triangular analysis window is used as the grey level noise of the camera is low and the spatial gradients are high with respect to the number of available pixels [33]. Within a single phase map it is possible that the displacement exceeds one grid pitch. This causes discontinuous jumps in the phase from $-\pi$ to π known as ‘phase wraps’. These discontinuities can be corrected for by using a suitable spatial unwrapping algorithm. Here, the algorithm described in [34] is used. A similar phase wrapping problem can also occur in time due to rigid body motion of the sample above one grid pitch. For the IBII test, the rigid body translation increases monotonically with the total rigid displacement between frames being much less than a grid pitch. Therefore, the phase can be temporally unwrapped by adding integer multiples of p_i to the phase maps so that the mean phase monotonically increases with time. Temporal phase unwrapping can also be corrected if the displacement is not monotonic. This requires plotting the displacement at each data point along time, and detecting jumps corresponding to one grid pitch and correcting for them by adding integer multiples of p_i to the phase maps.

Once the phase has been extracted for all images the displacement u between two images can be estimated by analysing the phase difference $\Delta\phi$ between them as follows:

$$u_i = -\frac{p}{2\pi}\Delta\phi_i \quad , \quad i = x, y \quad (3)$$

where p is the pitch of the grid. This equation requires that the displacements are small and that the grid pattern is regular. More recently an iterative procedure for calculating the displacement has been proposed in [18]. The use of this procedure corrects for irregularities in the grid pitch and accounts for the fact that the phase subtraction method does not include the physical displacement of the points of the grid. The strains can then be calculated from the displacement fields by differentiation:

$$\epsilon_{ij} = \frac{1}{2} \left(\frac{\partial u_i}{\partial j} + \frac{\partial u_j}{\partial i} \right) \quad , \quad i, j = x, y \quad (4)$$

In practice this is done by numerically differentiating the displacement fields using a centred finite difference algorithm (easily implemented in Matlab using the ‘gradient’ function). As the displacement fields contain noise it is normally necessary to smooth them prior to differentiation. The choice of smoothing parameters will be discussed in the next section (Section 4 of this report) in the context of obtaining accurate material properties from the raw images. For the analysis presented here, smoothing will not be applied prior to displacement differentiation.

An implementation of the grid method processing code in Matlab and Python is freely available from [35] including the iterative displacement calculation procedure. This code has been used here

to perform all grid method calculations. The next section discusses methods of depositing grids onto the surface of a sample.

3.2.3 Grid Deposition Techniques

The main drawback of the grid method when compared to DIC is the requirement that a regular pattern that is as accurate as possible must be deposited on the sample. The requirement of grid accuracy can be relaxed if the iterative displacement calculation procedure described in ref. [18] is used. This makes the pattern requirements of the grid method more similar to DIC which requires tight control of the speckle size to avoid aliasing issues. Here we present a new technique of printing grid patterns directly onto test samples that greatly mitigates the main drawback of the grid method (*i.e.* difficulty depositing a regular grid pattern onto the sample surface).

In previous studies using the IBII test grids were transferred onto the samples using the technique described in [36]. This procedure can produce grids of extremely fine pitches (down to $30\ \mu\text{m}$). However, the glue used to transfer the grids tends to form bubbles which do not fully transfer the grid pattern leading to missing pieces of grid where the bubbles were located. These spot defects have a significant impact on the kinematic fields obtained with the grid method and create a systematic error that cannot easily be corrected [13]. Thus, it is preferable to have a grid deposited with minimal defects.

Recently, a much simpler and more cost effective technique has been developed for printing grids directly onto the surface of the sample using a flatbed UV inkjet printer. This technique was applied to the IBII test in [13]. The results in [13] for the printed grids were compared to tests conducted using the grids produced with the method in [36]. It was shown that the technique for printing grids directly onto the sample drastically reduced the occurrence of spot defects due to missing parts of the grid. The main trade-off is that the current resolution of the printer used for this can only produce grids with pitches down to $0.34\ \text{mm}$. In the future improvements in printing technology should alleviate this. Given the current size of ultra-high speed camera pixel arrays this is more than adequate to produce the grids required for IBII tests on most materials (normally a grid with a pitch of $0.7 - 0.9\ \text{mm}$ is used).

The specific printer that was used here for producing the printed grids was a Canon Oce Arizona 1260 XT, an image of this printer is shown in Figure 14. This type of printer can be used to print on any flat and rigid substrate up to $50\ \text{mm}$ thick. Generally, a clearance of $0.3\ \text{mm}$ is added to the thickness of the samples to be printed on the print head does not collide with the samples.

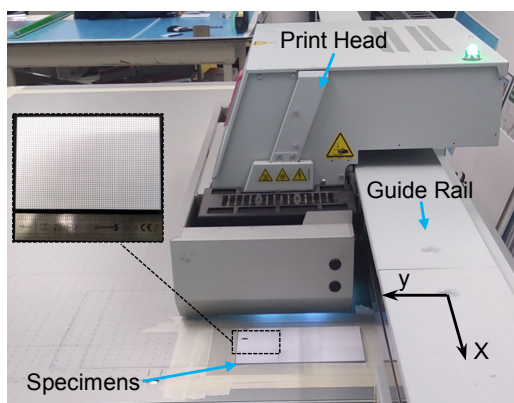


Figure 14: Printer system used for depositing grids on the samples.

When printing grids it is important to know the true resolution of the printer such that the grid pattern is adapted to the number of dots the printer can resolve. The Canon printer has several different resolution settings however, we will focus on two here: 1) ‘Quality’ at a nominal resolution of $446(x) \times 451(y)\ \text{DPI}$ and ‘High’ at a nominal resolution of $1058(x) \times 902(y)\ \text{DPI}$. Note that

the x direction refers to the direction in which the print head traverses along the guide rail and y is the direction in which the whole rail system moves (see Figure 14). For the ‘Quality’ setting, test grids were printed with a pitch of 4 dots (two printed dots and two blank dots) using the nominal resolution. Analysis of the grid showed that periodic irregularity appeared in the x direction with a period of 80 mm . This gives the difference between the real and nominal resolutions as: $\Delta DPI = \pm d_0/d$, where $d_0 = 25.4 mm$ and the defect period $d = 80 mm$. Thus, $\Delta DPI = 0.3175$ with a test print showing that this needed to be subtracted from the nominal resolution giving an effective resolution of $445.6825 \times 451 DPI$. A similar analysis of the ‘High’ setting showed a similar defect in the x direction which gave an effective resolution of $1058.33867 \times 902 DPI$. When creating a file for printing the grid this resolution must be specified correctly to ensure that the grids do not manifest these periodic defects. In the dataset detailed at the end of the manuscript two postscript files can be found that can be used for generating grids with either the ‘Quality’ or ‘High’ setting. The ‘Quality’ setting is generally preferable as it leads to the smallest mismatch in the x and y pitch of the grid. However, to print grids finer than 0.68 mm it is necessary to use the ‘High’ setting and only select pitches where the ratio of dots in each direction leads to small asymmetries in the pitch (approximately 1% of the pitch or less).

We note here that we have not tried this grid printing technique on another Canon Océ Arizona 1260 XT so it is possible that the real resolution analysis performed above is unique to each printer. Therefore we recommend that the resolution analysis described above is performed by printing grids onto paper before printing on prepared samples.

Normally the grid is printed as a series of disconnected black squares with a white paint layer giving optical contrast. For applications where larger strains are expected (*e.g.* plastic deformation in metals) a flexible paint is recommended such as Rustoleum Peel Coat. For black samples such as carbon fibre it is possible to print the grid as a series of white squares on the sample. However, the white ink used in the Canon Océ printer was found to be more specularly reflective leading to issues with lighting control and pixel saturation. For quasi-static testing this could be corrected for by using polarising filters. However, for high speed applications it is more difficult as the polarizers absorb some level of light which may result in the impossibility of filling the grey level histogram. For fine grids printed with the ‘High’ setting it is also recommended that the grid is printed twice to enhance the contrast of the grid. These grids were also imaged with an Allied Vision Manta camera and a Sigma 105 mm lens sampling at 10 *pixels/period* as shown in Figure 15. Even with the correction to the printer resolution there is still some variance between grid pitches due to the accuracy of the print head and nature of the droplet deposition process. However, the remaining pitch defects can be easily corrected for using the iterative displacement calculation method described in [18].

The grid printing technique described here can also be used for producing speckle patterns for DIC. In fact, the printing procedure described here is particularly advantageous because it allows for strict control of the dot size and production of an optimised DIC pattern. Also, as the accuracy of the printed pattern is much less critical for DIC it is possible to print finer speckles than the smallest grid pitch of 0.337 mm . Thus far we have produced speckle patterns with a dot size 65 μm which corresponds to a speckle that has a radius of approximately 3 printed pixels using the ‘High’ setting.

3.3 Triggering and Synchronisation

3.3.1 Lighting and Flash Trigger

As the Shimadzu HPV-X is quite light sensitive it is normally adequate to use a single standard photographic flash for lighting. In previous implementations of the IBII test a Gemini 1000 Pro flash was used [12–14]. The main drawback of using a photographic flash is that it requires a period of time to reach peak intensity which is commonly referred to as the ‘rise time’. For impact experiments the rise time of the flash can be on the same time scale as the experiment. Therefore,

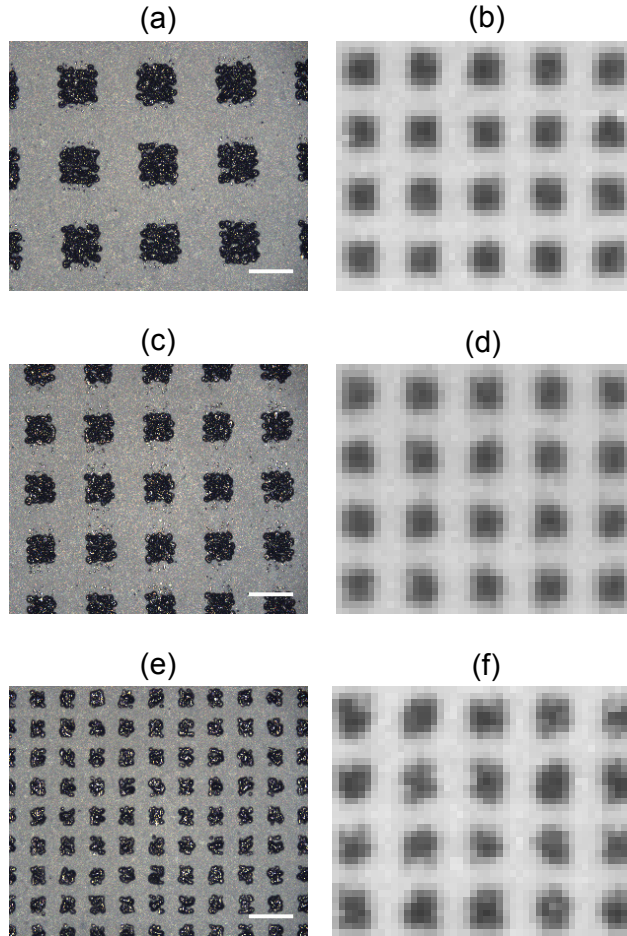


Figure 15: Comparison of common printed grid pitches (a),(b) 0.91 mm (c),(d) 0.68 mm and (e),(f) 0.337 mm . Images on the left hand side were taken with an optical microscope at $5\times$ magnification. Images on the right hand side were taken using a standard machine vision camera sampling at 10 pixels/period . The scale bar for the microscope images (a),(c),(e) is 0.5 mm .

it is important to analyse the rise time of a given flash and trigger it at an appropriate time to account for its rise time.

The lighting profile of the Gemini 1000 Pro flash was analysed using a Shimadzu HPV-X camera imaging at $200,000\text{ fps}$ with an integration time of 200 ns . A printed grid that filled the camera field of view was imaged. The flash was triggered directly from the camera with no delay. The mean grey level over the whole image as a function of time is plotted in Figure 16. This shows that the flash takes $40\text{ }\mu\text{s}$ to respond to the trigger signal before the light level starts to rise. After this, the flash takes $180\text{ }\mu\text{s}$ to reach peak intensity. Here the usable lighting time is taken as the period for which the intensity remains above 50% of the peak value. This give a usable time of approximately $500\text{ }\mu\text{s}$. Based on Figure 16 a delay of $150\text{ }\mu\text{s}$ is used for the flash to respond and rise to a usable light level.

The required lighting duration is driven by the required recording duration of the test, which is linked to the longitudinal wave speed in the material being tested. For most solid engineering materials the elastic wave speed is generally greater than 1000 m/s and with a specimen length of 70 mm the wave will traverse the specimen and return to the impact point within $140\text{ }\mu\text{s}$. This sets the time over which the light must be at a usable and preferably stable intensity. Fortunately, the usable light duration of the flash is long relative to this test duration. Thus, a large tolerance (more

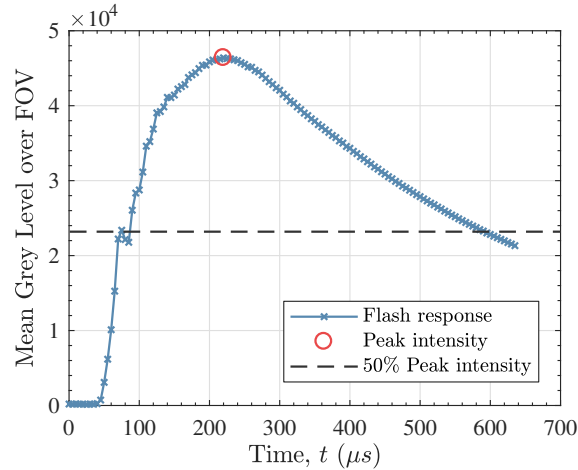


Figure 16: Response time for the Bowens Gemini 1000 Pro flash measured with a Shimadzu HPV-X camera at 200,000 *fps*.

than $\pm 10 \mu s$) on the accuracy of the flash trigger is allowable. This enabled the development of a flash trigger that was integrated with the Arduino light gate system used to measure the projectile speed. The Arduino system uses the projectile speed measurement to determine how long it will take the projectile to reach the waveguide given the range from the light gates to the target. A programmatic flow chart for the Arduino code is given in Figure 17. As described previously the speed is calculated once the back of the projectile has passed the last light gate. Thus, the effective range to target is the difference between the projectile length and the distance from the last light gate to the waveguide. The program then factors in the time taken to calculate the projectile velocity ($108 \mu s$) and the rise time of the flash ($100 \mu s$) such that the flash reaches peak intensity just before the projectile contacts the waveguide. The main advantage of this system is that it is robust to variations in projectile velocity and only needs to have the range to target and projectile length set as input variables for each test. The Arduino code used to trigger the flash can be found in the dataset attached to this report. The flash triggering method developed here is compatible with most off-the-shelf flash systems as long as the flash can receive an electrical trigger signal and the rise time is identified using the method described previously.

There are other systems that can be used for lighting such as continuous/flash LED light systems and pulsed lasers. For both of these systems triggering is much simpler as the usable light level for continuous light systems is effectively unlimited whereas for pulsed lasers the rise time is extremely low so the laser can be triggered based off an output signal from the camera. An example of a continuous LED light panel is the REL Surebright focused LED panel ². A significant advantage of a continuous light system is that it can be used effectively with frame rates that have recording times longer than the usable time of the photographic flash (*i.e.* 500,000 *fps* or less). This is especially useful for testing low-wave speed materials such as foams. An example pulsed laser system is the Cavitar, Cavilux Smart Ultra-High Speed system ³. The main advantage of the pulsed laser is that the pulse width can be set extremely short ($10 ns$) which effectively reduces the exposure time of the camera to the pulse width of the laser. The laser is capable of a repeat rate up to 10 *MHz*, synchronized with the camera framing. This combination is ideal for high magnification imaging where image blurring can become an issue with the lower integration time of the HPV-X camera, 110 *ns*.

²<https://www.relinc.com/split-hopkinson-bar-kolsky-bars/sure-test-systems/sure-bright-lighting-systems/>

³<https://www.cavitar.com/cavilux-laser-illumination-products/cavilux-smart/>

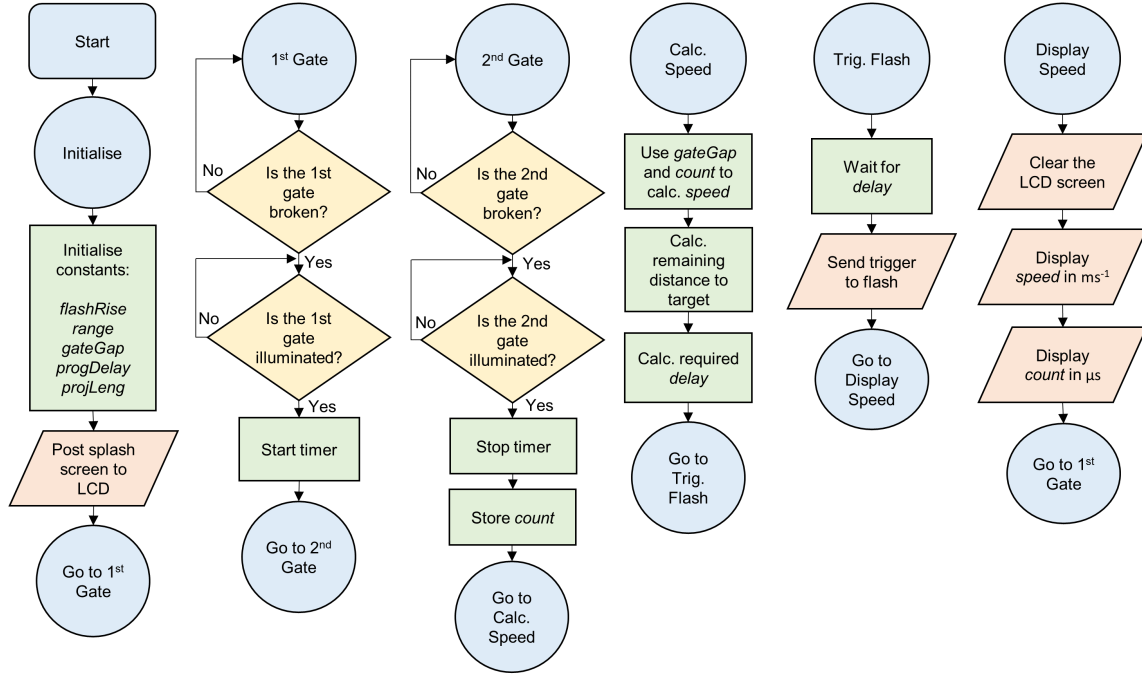


Figure 17: Program flow chart for the Arduino speed measurement system used to trigger the flash.

3.3.2 Camera Trigger

The current system for triggering the camera uses the contact of the projectile with the waveguide to complete a circuit and trigger the camera. A photograph of the trigger system is shown in Figure 18. The basic trigger system consists of two pieces of copper foil placed on the front face of the waveguide. These two pieces of foil are insulated from the metallic waveguide using double-sided tape. The two pieces of foil are then soldered to wires which in turn are connected to the BNC trigger port of the camera using a cable with alligator clips.

As the trigger signal is sent when the circuit is completed it is also necessary to include a delay to account for the time that the wave takes to propagate through the waveguide before entering the specimen. The delay that is required can be estimated using simple one dimensional wave theory to calculate how long the wave will take to traverse the waveguide. Take the test in [12] as an example. The waveguide is made from aluminium with material properties taken as $\rho = 2800 \text{ kg.m}^{-3}$ and $E = 70 \text{ GPa}$ giving a longitudinal wave speed of $c = \sqrt{E/\rho} = 5000 \text{ m.s}^{-1}$. The waveguide is 50 mm long so the wave will take $10 \mu\text{s}$ to travel through the waveguide. It is desirable to have at least 5 images captured before the wave enters the sample to avoid edge effects from the temporal differentiation scheme used to calculate the acceleration (more detail on calculation of acceleration is provided in the third section of this report, Section 4). For the tests in [12] images were captured at 2 Mfps giving an inter-frame time of $0.5 \mu\text{s}$. Thus, 5 frames is $2.5 \mu\text{s}$ giving a required delay of $7.5 \mu\text{s}$. This delay serves as an initial reference however, after the first test it is advisable to process the data and analyse the mean displacement, strain and acceleration as a function of time. If surface average of the acceleration field starts at 0 then the delay is correctly set. The data processing for the grid method and subsequent calculations of the kinematic fields is quite efficient and will generally produce results within a few minutes on a standard laptop. This analysis can be run while the next test is being set up. Another method for verifying the delay is to use the grid method to correlate the sequence of dynamic images with an image taken from a static reference of the test sample. Analysis of the strain fields will reveal when the wave is entering the sample. Note that the data processing procedures including calculation of acceleration are described in detail in the third section of this report (Section 4).

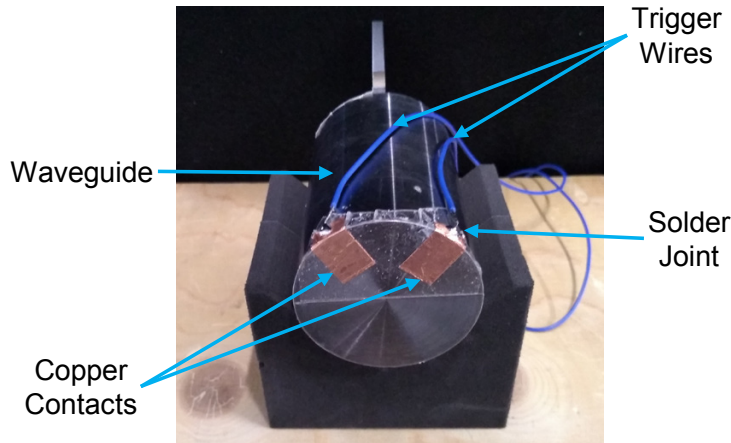


Figure 18: Copper contact trigger system used for triggering the camera. The trigger wires attach to the trigger port on the camera using a cable that has alligator clips on one end and a BNC port on the other.

The simple contact trigger described above has been used on all previous tests with the IBII method. However, there are other possible solutions for triggering. The most obvious is the use of a strain gauge bonded to the waveguide. Compared to the simple copper contact system this requires the use of signal conditioning and a picoscope to transmit the trigger signal from the gauge to the camera. However, this system has the advantage that the double-sided tape on the front of the waveguide can be removed. This thin layer of tape has a pulse shaping effect leading to a smoother loading pulse than direct metal to metal contact would produce (Figure 15 in [14]). By removing the tape it should be possible to achieve steeper loading pulses and higher strain rates at the cost of a more complex trigger system.

Another option for the trigger system is the use of a photon Doppler velocimetry (PDV) system pointed at the back of the sample or the back of the waveguide. Again, this system requires a more complex trigger setup but has additional benefits. If the PDV system is pointed at the back of the sample this would allow measurements to be taken directly at the free edge of the sample. As discussed in previous implementations of the IBII test method [12–14] one pitch of data is lost at the edge of the sample requiring data extrapolation to improve performance of the identification. Using an array of PDV probes on the free edge of the sample it would be possible to use the acquired data to aid the edge reconstruction procedure. This is an interesting avenue for future improvement to the IBII test method. Here it should be noted that the use of a PDV trigger on the back of the sample would require the camera to be post-triggered to retain the data that occurs before the wave reaches the free edge of the sample. Fortunately, the HPV-X camera has a continuous buffer and can be post-triggered. A similar arrangement was used in [37] using a Visar system rather than a PDV.

3.4 General Experimental Procedure

This section gives an overview of the procedure for setting up and running IBII tests from preparing samples through to obtaining the raw image data required for identifying material properties. A summary of the required equipment for running IBII tests is given in Appendix I for user reference.

3.4.1 Pre-test Preparation

The first step in preparing for a series of IBII tests is to align the specimen mounting stage and then update the code on the Arduino system to account for the range to target and projectile length for the specific test. The alignment procedure was already discussed in Section 3.1. As part of the alignment procedure a test shot is conducted to verify the alignment of the projectile and the waveguide. The secondary purpose of the alignment shot is to verify that the flash is being triggered at an appropriate time. This is achieved by setting the camera to post-trigger and recording 100 *frames* before the trigger event. The alignment shot is conducted at a frame rate of 500,000 *fps* giving an inter-frame time of 2 μs . Thus, 200 μs is captured before the trigger event allowing the rise time of the flash to be observed. Ideally, the flash should reach peak intensity just before the projectile contacts the waveguide. If this is not the case the range to target or flash delay needs to be adjusted and the alignment shot repeated until the flash is triggered at the appropriate time. Normally the appropriate flash timing can be achieved without requiring additional shots as long as the range to target is accurate to the nearest *mm*.

3.4.2 Sample and Test Component Preparation

Selection of specimen geometry needs to be considered so that the spatial resolution is appropriate for the test. The allowable specimen geometry is linked to the parameters of the camera and the full-field measurement technique being used. If using the grid method it is recommended that the minimum possible grid sampling is used at 5 *pixels/period*. The next step is to consider the pixel array size of the camera. The Shimadzu HPV-X has 400×250 *pixels* meaning that a maximum of 80×50 grid periods can fit in the field of view. The other constraint on the specimen geometry is the bore of the gas gun being used for the experiment. In Section 2 the bore size was set to 50 *mm* giving a maximum projectile diameter of 45 *mm* (allowing 5 *mm* for the wall thickness of the Delrin sabot). In order to impact the sample over the whole edge the maximum height of the sample is limited to 45 *mm*. Matching the aspect ratio of the camera gives a maximum length of 72 *mm*. Taking this value and dividing by the maximum number of grid periods over the height gives an ideal grid pitch of: $45 \text{ mm}/50 = 0.9 \text{ mm}$. Rounding up to the nearest printable grid pitch gives 0.91 *mm*. The field of view of the camera can now be determined by using the maximum number of grid periods in each direction as $72.8 \times 45.5 \text{ mm}$. Note that the sample dimensions will need to be smaller than this such that the sample remains within the field of view throughout the test, as outlined below.

Another constraint on the specimen geometry is that once the stress wave reaches the free edge of the sample rigid body motion occurs. The current data processing procedures for the IBII test assume that all edges of the sample are free apart from the impacted edge. Therefore, all free edges of the sample must remain in the field of view during the test. This is achieved by slightly reducing the size of the sample and allowing the sample to translate without moving outside the field of view. The rigid body motion that occurs over the test depends on the specific test set-up. However, it is generally less than 2 grid pitches for a standard test sample. Therefore it is recommended that specimens of $70 \times 44 \text{ mm}$ be used for the 0.91 *mm* grid. The test configuration outlined here (sampling of 5 *pixels/period*, grid pitch of 0.91 *mm*, specimen geometry of $70 \times 44 \text{ mm}$) is suitable for most general purpose testing. If another camera or gas gun bore size is used then the required grid pitch can be calculated using the reasoning previously outlined.

Apart from the in-plane dimensions the thickness of the sample also needs to be considered. The thickness should be much less than the in-plane dimensions to ensure that the sample is in a state of plane stress and that the kinematic fields are uniform through-thickness (*i.e.* the test is 2D). This is generally satisfied if the thickness is one tenth or less of the smallest in-plane dimension (see the appendix in [12]). Thus, for the case considered previously the thickness of the sample should be 4.4 *mm* or less.

For some materials it is not possible to obtain samples of sufficient size to use 0.91 *mm* grids.

An example of this is the 18×12 mm through-thickness composite samples tested in [13]. In this case it was shown that using the printed grids of 0.337 mm sampled at 7 pixels/period produced excellent results due to dramatic decrease in point grid defects. For samples smaller than this the process described in [36] is required.

It should be noted that the IBII test method does not require that the sample is impacted over the whole edge. The only requirement is that all other edges remain free so as not to introduce additional unknowns into the dynamic equilibrium of the specimen. This means it would be possible to impact the sample over some portion of its height and still use the same analysis techniques. In fact, this would induce a more heterogeneous stress state allowing for the identification of more complex material models. This is an interesting area which will be investigated as future work.

Apart from the test sample geometry the projectile/waveguide material and geometry also need to be considered in addition to the required impact velocity. While the specimen geometry is generally limited by the pixel array of the camera, there is much more flexibility in the design of the projectile and waveguide based on the loading that needs to be achieved. The most efficient method of optimising the test set-up is to use a parametric sweep of geometry and projectile velocity using an explicit dynamics finite element model. This allows for various projectile and waveguide configurations to be investigated with minimal cost. The finite element modelling process has been described for previous implementations of the IBII test in references [12–14]. When selecting a material for use as a projectile/waveguide it is important to keep in mind two factors. The first is the longitudinal wave speed in the material and the second is the yield or failure stress of the material. Generally it is easier to use a projectile/waveguide material that has a similar longitudinal wave speed to the material being tested, as this makes it easier to control the pulse length and introduce a single loading pulse into sample. The failure stress of the projectile is also important as this determines the magnitude of the loading pulse that can be induced in the sample. Example projectiles from various test configurations are shown in Figure 2.

After the sample has been machined a grid is applied to the surface as described in Section 3.2.3. The sample is then bonded to the back of the waveguide using an engineer’s square as guide to make sure the sample is perpendicular to the back of the waveguide. It is also helpful to mark the required specimen position with a pencil to help align the sample in the centre of the waveguide. Due to the turning process used to produce the waveguides there can be a small nodule of material left at the centre of the waveguide. This needs to be removed using a fine grit sandpaper prior to bonding the sample. For dense materials such as metals and ceramics it is recommended that a cyanoacrylate glue be used. For lighter materials such as composites and polymers a temporary spray adhesive is sufficient. After the sample is bonded to the back of the waveguide the back surface of the waveguide should be masked with a non-reflective material as shown in Figure 19 (a) (masking tape is a convenient material for this purpose). This prevents light reflecting off the metal waveguide causing brighter illumination near the impact edge of the sample, making it easier to achieve a uniform illumination across the whole sample.

The waveguide and sample can then be placed in the working section of the gas gun using a wedge shaped foam stand as shown in Figure 19 (b). Previously we have used Rohacell machinable foam to make the stands. However, this type of foam tends to be destroyed with each test. More recently we have had stands water-jet cut from high density PVC foam. This is the type of stand shown in Figure 19 (b). A design drawing for the foam stand can be found in the dataset. The wedge shaped foam stand is attached to an aluminium tray using double-sided tape. For smaller samples such as the through-thickness samples tested in [13] it is advisable to use double-sided tape or spray glue to attach the waveguide to the foam stand such that it is not ‘blown away’ by the air escaping the barrel ahead of the projectile. The pitch alignment of the sample can be verified with a spirit level and adjusted if necessary using the pitch rotation stage as shown in Figure 19 (b).

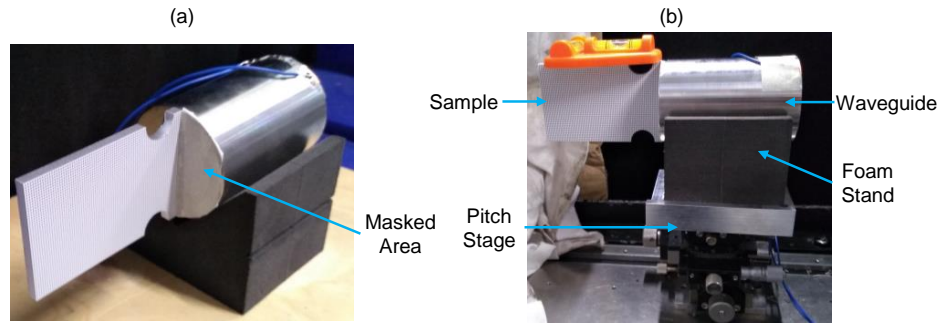


Figure 19: (a) Example prepared waveguide and sample showing masked area to prevent light reflection. (b) Placement and alignment of sample and waveguide in the working section of the gas gun.

3.4.3 Camera Setup

The main aspects of the camera set-up that need to be selected include the frame rate, exposure time and lens. In general the choice of frame rate is driven by the longitudinal wave speed in the material being tested, the sample geometry and the type of test being performed. The same one-dimensional wave analysis that was used to calculate the camera delay (see Section 3.3.2) can be used to estimate the total recording time that is required based on the length of the sample. The final consideration is the type of test being performed. For spall type IBII tests like [12–14] the recording time needs to be set to include the wave reflection and failure of the sample to measure the tensile failure stress. However, for testing the plastic behaviour of metals in compression the unloading portion of the test is not required, so the frame rate can be set such that the reflected tensile wave is not fully captured [38]. As a broad recommendation when testing materials with high wave speeds (i.e. ceramics and metals) 5 *Mfps* should be used whereas testing polymers or transverse composites will require a frame rate of 1 – 2 *Mfps*. In general it is desirable to set the exposure time to the smallest value possible to reduce any effects resulting from motion blur. For recording at 5 *Mfps* the exposure time is fixed at 110 *ns* while for 2 *Mfps* and lower the minimum exposure time is 200 *ns*. This difference in exposure time should be kept in mind as it can lead to a significant difference in light intensity when switching between 5 and 2 *Mfps*.

Previous implementations of the IBII test have used a Sigma 105 *mm* fixed focal length lens. The advantage of the fixed focal length lens is that it generally has lower optical distortion than a zoom lens. Other lens can be used for the IBII test however, it is recommended that a fixed focal length lens with a high focal length is used. Additional specifics of lens selection for optical full-field measurements are discussed in [39].

There are several practical considerations for mounting the camera and flash for the experiment. The camera should be mounted on a 3 axis tripod head along with a translation stage. The translation stage is required for two reasons, the first is that it makes it much easier to position the camera to achieve accurate grid sampling and the second is that it allows for the use of an out-of-plane movement test during set-up. An example translation stage which is compatible with standard tripod adaptors is the Manfrotto SKU 454 micro-positioning sliding plate ⁴.

Apart from positioning the camera the position of the flash with respect to the camera also needs to be considered to achieve optimal lighting. Generally, the flash needs to be placed at an angle to the optical path of the camera to avoid specular reflection off the window of the capture chamber. A typical camera and flash set-up is shown in Figure 20. From our experience it is easier to achieve more uniform light intensity if the flash is above the camera as shown in Figure 20 rather than beside the camera as this avoids reflection or shadows from the back of the waveguide.

⁴<https://www.manfrotto.co.uk/micro-positioning-sliding-plate>

When setting up the camera and flash to image the sample there are several factors that need to be considered including 1) lighting, 2) grid alignment, 3) grid sampling, and 4) defocusing/blurring. Each of these factors will affect the quality of the raw data obtained. The lighting drives the contrast of the image which in turn relates to the achievable signal to noise ratio. The other three factors relate to the grid method and errors in any of these will produce a systematic error that manifests itself as artificial fringes in kinematic fields. Most of these factors are coupled so they need to be analysed in an iterative manner to converge on a appropriate set-up. The general procedure for setting up the camera and flash is as follows:

1. Use the ‘live’ view mode to place the camera such that the sample fills most of the field of view.
2. Place the flash at an angle to the camera and connect it to the auxiliary port on the camera.
3. Use the angular adjustments on the tripod head to align the camera sensor to the grid.
4. Set the delay on the camera to $150 \mu s$ to account for flash rise time and manually trigger the camera to acquire the first series of images.
5. Check the lighting and grid sampling using Matlab programs (provided in the dataset), continue adjusting the camera position until an integer sampling is achieved and adjust the flash position/intensity until the lighting is optimal.
6. Once the lighting and grid sampling are optimal take the first set of static reference images
7. Perform an out of plane movement test by moving the camera on the translation stage and taking another set of images.
8. Move the camera back to its original position and take another set of static images, check the grid sampling to verify the camera has been moved back to its original position.
9. Process the out of plane movement image with one of the static reference images and verify that the image is appropriately blurred by checking that there are no fringes in the strain fields.
10. Iterate through steps 3 to 8 until the lighting, grid alignment, sampling and blurring are optimal.

The next two sections will focus on the specifics of steps 5 to 9 to achieve an optimal set-up. Note that once the camera and flash have been positioned for the first test sample it is generally much quicker to set up and align subsequent specimens.

3.4.4 Grid Alignment and Sampling

When setting up a grid method experiment the grid is normally aligned with the camera sensor. Alignment is required in the in-plane and out-of-plane directions. In-plane alignment can be visually appraised by using a cross-hair on the grid image. Out-of-plane mis-alignment will manifest as a linear strain gradient in an out-of-plane movement test. More recent work on the grid method has demonstrated that it is possible to analyse grid data that is intentionally rotated (in-plane) with respect to the camera sensor to minimise aliasing between the camera sensor and grid [40]. However, this requires the use of a Gaussian analysis window which has a larger minimum size than a bi-triangular window. This is a disadvantage for the IBII method as a larger analysis window will lead to more of the data on the border of the sample being lost. This is especially critical due to the small pixel array sizes on current ultra-high speed cameras. This analysis may be possible in the future when ultra-high speed cameras have larger pixel arrays. For now it is recommended

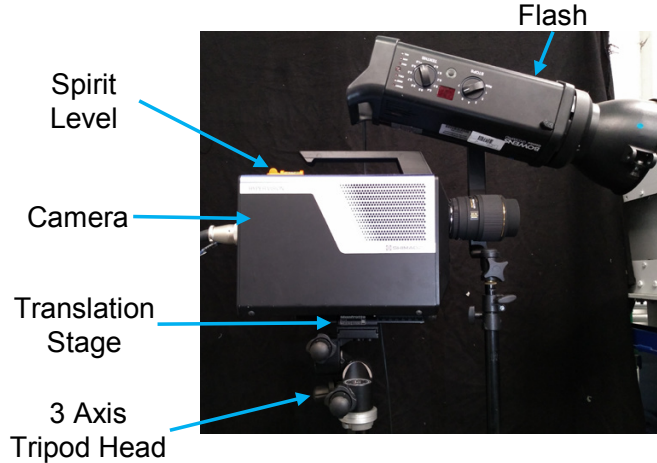


Figure 20: Typical camera and flash set-up.

that the grid is aligned with the camera sensor and a bi-triangular analysis window is used with the smallest sampling possible at 5 pixels/period .

Apart from alignment it is also critical that the camera is positioned such that the sampling is as close to an integer as possible. This process is made significantly easier if the camera is attached to a translation stage because this allows for fine adjustment of the sampling without having to move the whole tripod. An easy way to check the sampling is to analyse a down-sampled version of the grid image. If the lighting is completely uniform and the sampling is exactly 5 pixels/period then every fifth pixel will exhibit the same grey-level. If the sampling is incorrect then Moiré fringes will appear. For a real experiment the lighting is rarely uniform so down sampling in this way reveals the mean light intensity over the image if the sampling is an exact integer. An example of the down-sampling procedure for integer and non-integer sampling is given in Figure 21 (c) and (d) for a 0.91 mm pitch printed grid imaged with the Shimadzu HPV-X and a Sigma 105 mm lens. The sampling can also be analysed by performing a Fourier transform along the rows or columns of the grid image. The result of taking the Fourier transform along a row near the centre of the image is shown Figure 21 (e) and (f). A Matlab program was developed that performs the sampling analysis described above. This program can be found in the dataset at the end of the manuscript.

Analysis of Figure 21 can also give an indication of the lens distortion that is present in the images. The relative uniformity of Figure 21 (c) shows for this camera and lens combination (Shimadzu HPV-X camera and Sigma 105mm macro lens) there is minimal lens distortion. For other lenses it is possible that lens distortion effects will be more pronounced. If there is limited deformation or rigid body movement then lens distortion will not have a significant impact on the test results. However, when large rigid body motion is expected it may be necessary to use an appropriate lens distortion model. This can be calibrated by imaging a grid of known pitch that fills the camera field of view.

3.4.5 Defocusing and Out of Plane Movement

Grids produced with the printing process described in Section 3.2.3 or those produced with the process described in [36] are binary, meaning that the grid is effectively a square wave signal. The sharp transition in the square wave leads to harmonics in the phase when using the grid method. To avoid this it would be preferable to produce grids that are almost sinusoidal by printing an ‘egg box’ pattern. Unfortunately, this is difficult to produce with the technology described in [36]. This has not been attempted yet with the grid printing procedure and is an area for potential future work.

Other than directly printing a sinusoidal grid it is also possible to mitigate the problem by

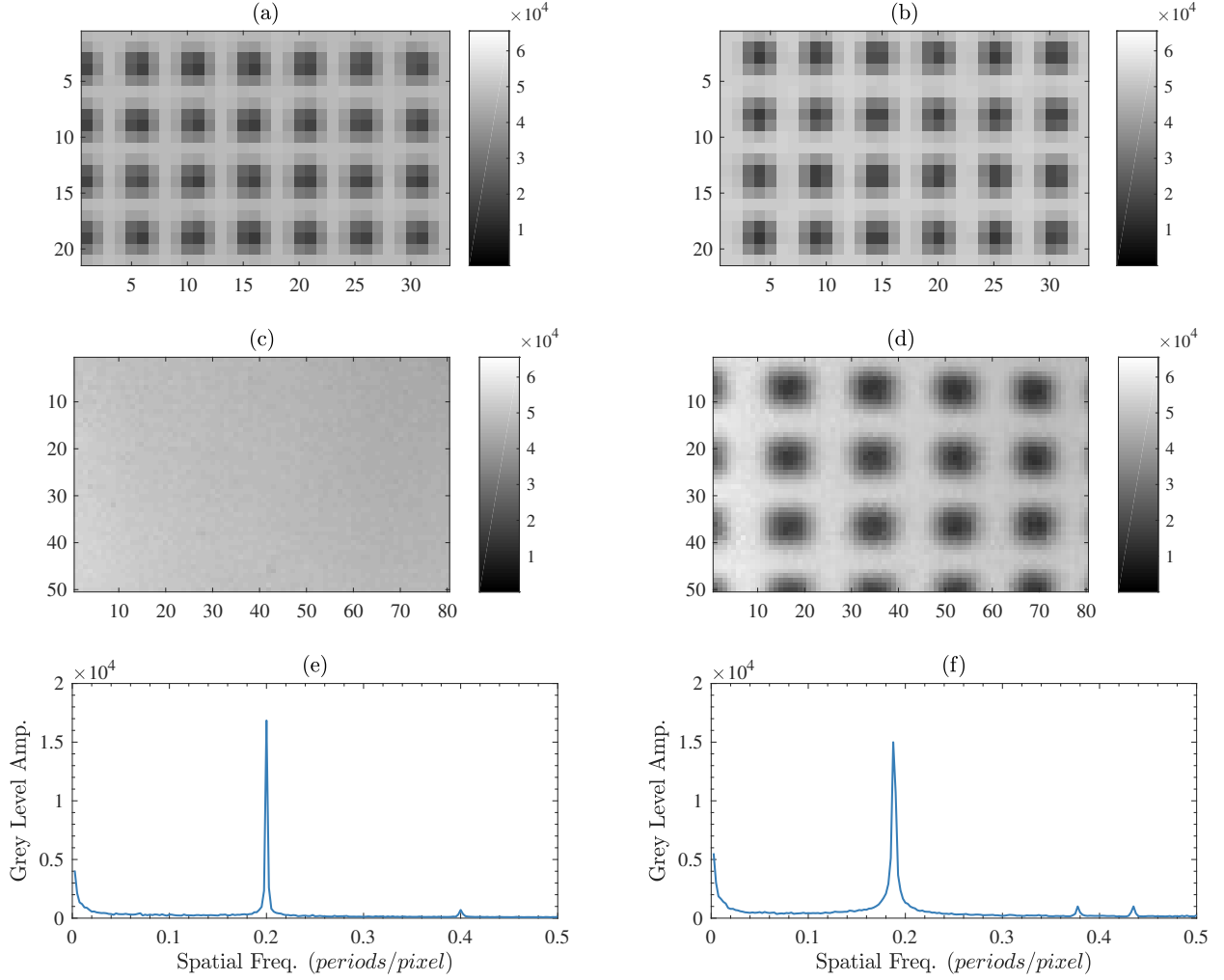


Figure 21: Comparison between integer sampling (5 *pixels/period*) (a),(c),(e) and non-integer sampling (5.31 *pixels/period*) (b),(d),(f). Zoomed in region of a raw grey level image of a 0.91 mm printed grid taken with the Shimadzu HPV-X (a),(b). Down sampled full image taking every fifth pixel (c),(d). Frequency spectrum taking a horizontal row near the centre of each image (e),(f).

slightly defocusing the camera lens and blurring the image. The drawback of this approach is that when the lens is defocused, the contrast of the grid is reduced, lowering the signal to noise ratio. Effectively, the process of defocusing the lens trades a systematic error (harmonics in the phase maps) for an increased random error (lower signal to noise ratio). This trade-off is favourable because it is easier to compensate for a random error using noise filtering procedures whereas it is extremely difficult to remove a systematic error that causes spurious fringes at a frequency similar to the signal of interest. Further discussion of noise filtering procedures is given in the third section of this report (Section 4).

The process of blurring the grid image has also been found to be beneficial for suppressing artificial fringes that occur due to the low pixel fill-factor that is characteristic of high speed cameras. For the Shimadzu HPV-1 (the predecessor of the HPV-X) this was especially pronounced as the fill-factor was only about 14% in the longitudinal axis of the sensor [28, 29]. Though, the fill-factor is much more favourable for the HPV-X, with 94% in the horizontal direction but it is still only 67% in the vertical direction [41]. Thus, the blurring procedure is also beneficial for mitigating any additional spurious fringes arising from the reduced pixel fill factor in the vertical direction.

While defocusing the image of the grid is beneficial the obvious question is ‘How much blurring is enough?’. If the image becomes too blurred the signal to noise ratio will be too low to accurately

capture the wave as it propagates in the test sample. To check if the blurring is adequate an out of plane movement test can be used. The basic idea is to take a series of static images and then move the camera out of plane by a small amount (1 to 5 mm is normally sufficient depending on the working distance). This out of plane movement creates an artificial uniform isotropic strain which has an approximate magnitude of $\epsilon = dz/z$ where dz is the distance the camera moves and z is the working distance between the camera and sample. If the blurring is not sufficient then spurious fringes appear in the strain fields that should otherwise be spatially uniform. This is demonstrated in Figure 22 for a printed grid of 0.91 mm imaged with the Shimadzu HPV-X camera with a Sigma 105 mm lens. Note the slight decrease in contrast when blurring the image as shown in Figure 22 (c) and (d). If the blurring is appropriate then the fringes will be removed from the strain field as shown by comparing Figure 22 (e) and (f). The working distance for this test was $\sim 680 mm$ with an out of plane movement of 5 mm giving an expected artificial strain of 7.35 $mm.m^{-1}$ which compares well to the mean strains in Figure 22 (e) and (f).

Once the image is appropriately blurred the sampling must also be verified using the procedure described in Section 3.4.4. Note that the act of defocusing the lens slightly changes the magnification and hence the sampling of the grid. Therefore, it is recommended that the sampling is checked after blurring before performing an out of plane movement test. The out of plane movement test should be approached with caution because many errors that can occur with the grid method will manifest as spurious fringes in this type of test. An example of this is having inappropriate grid sampling or a fill factor problem. More recently we tested a composite material that was produced by vacuum bagging with a fabric layer on both sides. This left a fabric imprint on the sample surface which had a similar frequency to the grid pattern printed on the surface. We found that if this fabric print was not removed by polishing the samples it would create spurious fringes in the grid analysis.

From our previous experience it is much easier to converge on an optimal experimental set-up if a reference image with optimal set-up is available for direct comparison. Therefore, the dataset detailed at the end of the manuscript contains a series of example images taken with the Shimadzu HPV-X camera of printed grids with pitches of 0.91 mm , 0.68 mm and 0.34 mm (produced using the procedure described in Section 3.2.3). This part of the dataset also contains the associated out of plane movement test images which can be used for comparison purposes. The complete camera set-up and grid sampling procedure can appear to be quite tedious but with experience, it becomes easier. We strongly advise against any short-cuts here as our experience has taught us that the thoroughness of the camera set-up procedure is paramount to the quality of the results.

3.4.6 Running the Experiment

As there is considerable time investment in preparing samples and setting up the experiment it is desirable that all tests are successful. The most common way of missing a test is due to human error (*e.g.* not connecting a trigger properly or setting an inappropriate delay on the camera). Based on previous experience in our laboratory, having a check list that is consulted before each test minimises the possibility of human error. Before the impact experiment is run the flash is generally connected to the auxiliary port on the camera for the purpose of taking static images to align the camera and perform the out of plane movement test described above. The check list given below assumes that the camera and flash are in this pre-test state and that the camera is aligned according to the procedures given in Section 3.4.3 above.

1. Set the delay on the camera to account for the time taken for the wave to travel through the waveguide.
2. Connect the wires from the contact trigger to the BNC trigger port on the camera.
3. Disconnect the flash from the camera auxiliary port and connect it to the BNC cable attached to the Arduino light gate system.

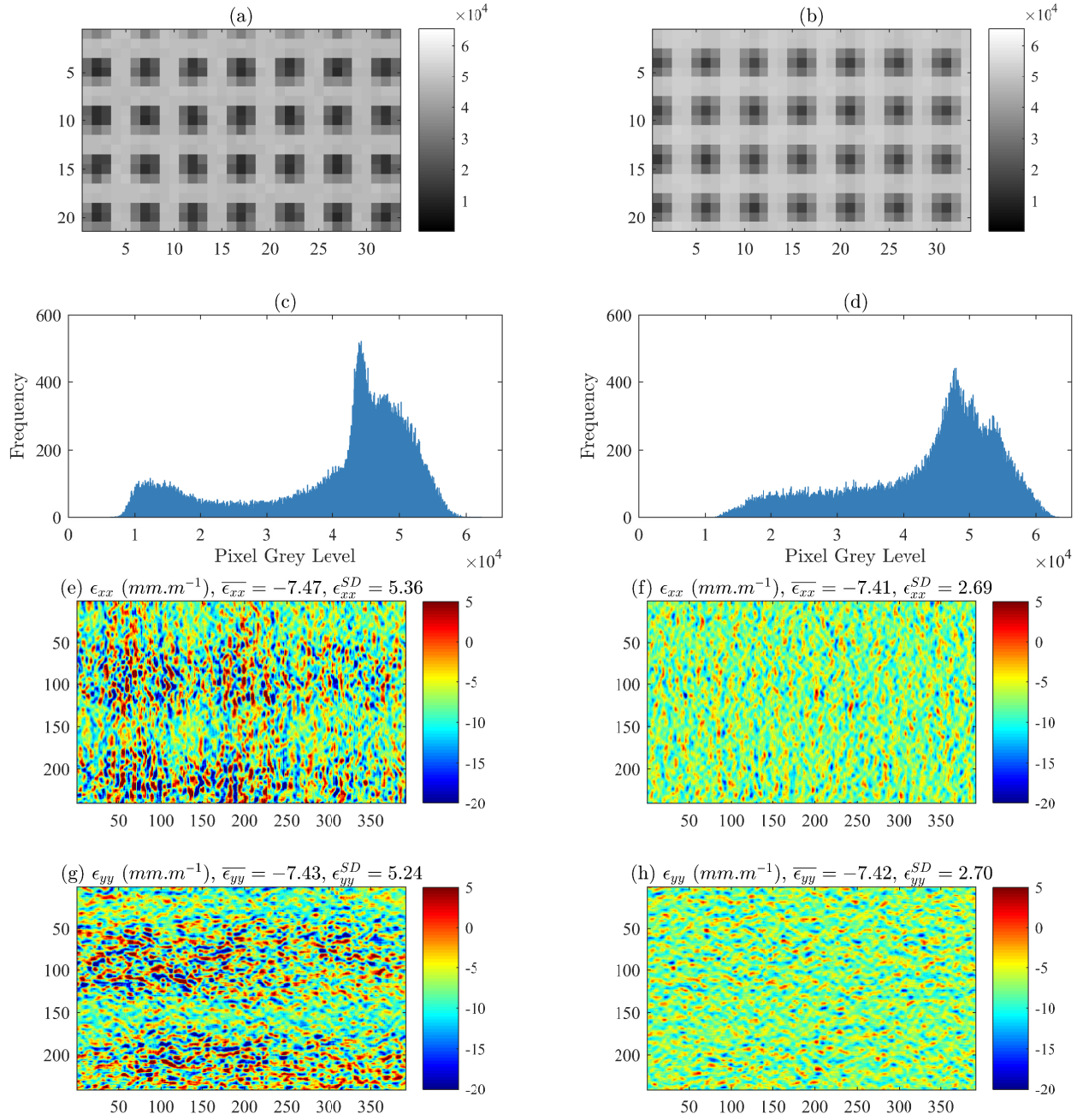


Figure 22: Comparison between an overly sharp (a),(c),(e), (g) and appropriately blurred grid image (b),(d),(f),(h). Close up image of the sharp (a) and blurred (b) grid, note the asymmetry in the sharp grid pattern. Grey level histogram for sharp (c) and blurred (d) grid images. Strain fields from an out of plane movement test for sharp (e),(g) and blurred (d),(h) grids, note the distinct pattern in the sharp image strain field.

4. Arm the camera (set it to recording mode) and test the trigger by gently touching the two copper contacts with a conductive material to complete the circuit.
5. Test that the Arduino is triggering the flash by pulling a piece of opaque material through the path of the light gates.
6. Close the capture chamber and load the breech of the gas gun.
7. Arm the camera, pressurise the gas gun and run the experiment.
8. Backup the test data to an external drive.

The most common error is associated with step 1 where the camera delay is left in the state required for taking static images ($150 \mu s$ to account for the flash rise time) so special care should be taken such that the delay is set appropriately for the experiment. It is useful to have two people for step 7 such that one can operate the camera and the other can control the gas gun. This is especially important if running the camera at $2 Mfps$ or higher as the camera will time out and stop waiting for a trigger signal if not triggered within $60 s$. It is also recommended that the data is analysed while the next test is being set-up such that any adjustments (*e.g.* changing the camera delay to increase/decrease the number of blank frames) can be made prior to running the next experiment.

4 Theory and Data Processing

The previous section of this report has described the IBII method up to the point at which the experiments have been completed and high quality raw image data has been obtained. From here our goal is to use the grid method to obtain the displacement fields and then apply the virtual fields method (VFM) theory to extract the material properties from the full-field kinematics. This section of the report begins by discussing the VFM theory for processing IBII test data. This is followed by a description of the IBII processing code that implements VFM theory in Matlab. The IBII processing code is made freely available and can be found in the dataset attached to the report. The final part of this section describes the image deformation procedures used for selecting optimal smoothing parameters for processing IBII data in a similar manner to [42–46]. The Matlab codes for creating deformed grid images from FE data and for performing a parametric sweep of smoothing parameters can also be found in the attached dataset.

4.1 IBII Test Theory

This section will give an overview of the virtual fields method (VFM) theory required for identifying material properties from an IBII test. A more general description of the VFM theory is given in [15]. The most developed application of the IBII test includes two different material models: 1) linear elastic orthotropic materials tested transverse to the highest stiffness direction (referred to as reduced orthotropic) [12, 13], and 2) linear elastic isotropic materials [13, 14]. The required theory for these two cases will be discussed below as these

Recently, other material models have been investigated with the IBII methodology including metal plasticity [38], orthotropic off-axis fibre composites [47] and adhesives [48]. The processing methods for these models will be implemented in later release versions of the IBII processing code. For now the reader is referred to the individual references for the specific theory required in each case.

4.1.1 The Virtual Fields Method

The VFM uses the principle of virtual work to extract material properties from full-field kinematic measurements. The principle of virtual work describes the weak form of equilibrium. With strategic

selection of virtual fields one obtains independent expressions relating the internal state of stress to external forces and/or acceleration. The internal stress state depends on the unknown stiffness parameters, which can be directly identified from these expressions by substitution of an appropriate constitutive model. The general form of the principle of virtual work, neglecting body forces is:

$$-\int_V \boldsymbol{\sigma} : \boldsymbol{\epsilon}^* dV + \int_{\delta V} \mathbf{T} \cdot \mathbf{u}^* dS = \int_V \rho \mathbf{a} \cdot \mathbf{u}^* dV \quad (5)$$

where V and S denote the volume and surface of the region of interest, \mathbf{T} is the Cauchy stress vector acting at the boundaries of δV , \mathbf{u}^* is the virtual displacement field, $\boldsymbol{\epsilon}^*$ the virtual strain field and $\boldsymbol{\sigma}$ the Cauchy stress tensor. Note that $:$ and \cdot denote the dot product in matrix and vector forms, respectively. The first and second terms on the left hand side of equation (5) represent the internal and external virtual work, respectively. The term on the right hand side of the equation represents the virtual work of inertial forces (or acceleration virtual work). Any continuous and piecewise differentiable virtual fields will satisfy the principle of virtual work, with $2\epsilon_{ij}^* = u_{i,j}^* + u_{j,i}^*$.

Consider the schematic of an IBII sample shown in Figure 23. The goal is to relate the measured kinematic fields to the desired material properties using equation 5. Here, the following assumptions are made: 1) the material has constant density, thickness and stiffness throughout; 2) the kinematic fields are constant through-thickness; and 3) the specimen is loaded in a state of plane stress. Under these conditions, equation (5) simplifies to:

$$-\int_S \boldsymbol{\sigma} : \boldsymbol{\epsilon}^* dS + \int_{\delta l} \mathbf{T} \cdot \mathbf{u}^* dl = \rho \int_S \mathbf{a} \cdot \mathbf{u}^* dS \quad (6)$$

where l denotes the in-plane boundary of the specimen where tractions are applied. It is useful to note here that not all of the previously mentioned assumptions are compulsory for analysing test data with the VFM. Previous implementations of the VFM under quasi-static loading have shown that the material properties can be parametrised in space as in refs. [49, 50]. Also, in [51] it was shown that the density change caused by compaction waves in dynamically loaded foams could be accounted for in the VFM analysis. These cases illustrate that it is possible to design test analysis procedures using the VFM by manipulating the principle of virtual work creatively. In fact, designing an IBII test method for heterogenous materials is an interesting area of future work.

In order to use equation (6) for material property identification, it is necessary to define a constitutive model and substitute this for the stress in the equation.

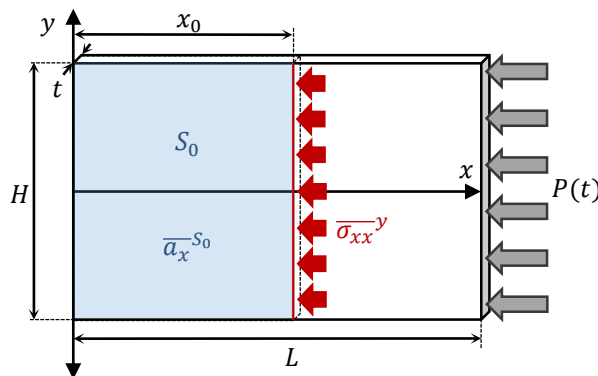


Figure 23: Schematic of an IBII test sample, all edges are free apart from the impact edge which has a pressure pulse applied.

4.1.2 Constitutive Laws

A general constitutive law for a linear elastic orthotropic material is given as follows:

$$\begin{bmatrix} \sigma_{xx} \\ \sigma_{yy} \\ \sigma_{xy} \end{bmatrix} = \begin{bmatrix} Q_{11} & Q_{12} & 0 \\ Q_{12} & Q_{22} & 0 \\ 0 & 0 & Q_{66} \end{bmatrix} \begin{bmatrix} \epsilon_{xx} \\ \epsilon_{yy} \\ \epsilon_{xy} \end{bmatrix} \quad (7)$$

where the Q_{ij} 's represent the stiffness components, and σ_{ij} 's and ϵ_{ij} 's denote the stress and strain components in the global coordinate system. The standard convention for composite materials has been adopted here with the co-ordinate 1 corresponding to the fibre direction and 2 corresponding to the direction transverse to the fibres.

Reduced Orthotropic Model: The reduced orthotropic material model is a special case of a general orthotropic material model. This model is used for materials which exhibit a significantly higher stiffness in the direction transverse to the loading direction. For example, testing uni-directional carbon fibre composites in the transverse direction or through-thickness direction, as in refs. [12, 13]. In this case the fibre direction is aligned with the global y coordinate in Figure 23 and the stiffness components Q_{11} and Q_{22} are reversed in equation 7. The analysis here will focus on the case of the in-plane transverse properties. In this case, the strains from Poisson's effect and the ϵ_{yy} strains from loading will be minimal compared to the axial strains. Also, as the minor Poisson's ratio is very small $Q_{22} \sim E_{22}$. Thus, the general orthotropic material model reduces to: $\sigma_{xx} = E_{22}\epsilon_{xx}$. This reduced orthotropic material is the simplest case for the IBII test as only a single material stiffness, E_{22} , needs to be identified.

Isotropic Model: If the material is isotropic, the linear elastic constitutive relationship only depends on two parameters, Q_{11} and Q_{12} , since $Q_{22} = Q_{11}$ and $2Q_{66} = Q_{11} - Q_{12}$. The virtual fields implemented in the IBII processing code for identifying these stiffness parameters are described in the following sections.

4.1.3 Virtual Fields for Stiffness Identification

The final step of the VFM is to select virtual fields. Here, we will focus on the three types of virtual fields that have been used for stiffness identification in previous implementations of the IBII test. It should be noted here that there are other methods for selecting virtual fields such as the sensitivity based virtual fields described in [52] or the generalized stress-strain curve procedure described in [53]. These will be implemented in a future version of the IBII test processing toolbox. The three separate approaches currently implemented in the IBII processing toolbox include:

1. Manual virtual fields: Use equation 6 with manually defined functions as virtual fields.
2. Special optimised virtual fields: Use a noise minimisation procedure to automatically define virtual fields that minimise the effect of strain noise on the identification as in refs. [15, 54].
3. Rigid body virtual fields: Construct stress-strain curves using stress averages from acceleration and linearly fit the curves to obtain the stiffness.

Here, only the theory for the manual virtual fields and rigid body virtual fields will be discussed as examples. More detailed formalism of the special optimised virtual fields can be found in refs. [15, 54]. Note that the special optimised virtual fields are implemented in the IBII processing code and the results of the manual and special optimised virtual fields will be presented in later sections (see Section 4.3.10).

4.1.4 Manual Virtual Fields for Stiffness Identification

Reduced Orthotropic Case: As there is only a single stiffness parameter to be identified for the reduced orthotropic model only a single virtual field is required. When using the IBII test the load information is provided by the acceleration and the external loading pulse is not measured. Thus, it is desirable to select virtual fields that cancel the contribution of the unknown pressure pulse (*i.e.* the external virtual work term). A simple virtual field that satisfies this constraint is given by: $u_x^* = L - x$ and $u_y^* = 0$, where L is the length of the sample as shown in Figure 23. Substituting the reduced orthotropic constitutive law and the given virtual field into the principle of virtual work gives the following:

$$E_{22} = \frac{\overline{\rho a_x(L-x)}^S}{\overline{\epsilon_{xx}}^S} \quad (8)$$

where $\overline{\epsilon_{xx}}^S \neq 0$ and ρ is the density of the material. The superscript S coupled with the overline notation indicates the spatial average over the whole surface of the sample. Thus, term $\overline{a_x(L-x)}^S$ is the surface average of the acceleration weighted by the function $x - L$ over the whole surface of the sample and $\overline{\epsilon_{xx}}^S$ is the average of the axial strain over the same surface. This equation can be used at any time step of the test to directly identify the stiffness E_{22} from the kinematic fields.

Isotropic Case: For isotropic materials, two stiffness parameters must be identified simultaneously and therefore, two sets of virtual fields are required. This will produce two linear equations in terms of Q_{11} and Q_{12} which can be solved simultaneously at each time step. The virtual fields will also need to be selected to cancel the contribution of the unknown pressure load. The first virtual field will be the same as used for the reduced orthotropic model: $u_x^* = L - x$ and $u_y^* = 0$. Substituting this and the isotropic constitutive law into the principle of virtual work gives:

$$Q_{11}\overline{\epsilon_{xx}}^S + Q_{12}\overline{\epsilon_{yy}}^S = \overline{\rho a_x(L-x)}^S \quad (9)$$

The second set of virtual fields is given by: $u_x^* = 0$, $u_y^* = \frac{(L-x)y}{H}$, where the in-plane dimensions of the specimen are given by L and H as defined in Figure 23. Combining this virtual field, the isotropic constitutive law and the principle of virtual work gives:

$$-Q_{11} \left[\overline{(L-x)\epsilon_{yy}}^S - \overline{y\epsilon_{xy}}^S \right] - Q_{12} \left[\overline{(L-x)\epsilon_{xx}}^S + \overline{y\epsilon_{xy}}^S \right] = \overline{\rho(L-x)ya_y}^S \quad (10)$$

Here averages and weighted averages of the kinematic fields are calculated over the whole surface of the sample. These equations can be solved simultaneously at any time point in the test to identify the stiffness components Q_{11} and Q_{12} .

4.1.5 Rigid Body Virtual Fields for Stiffness Identification

Using a simple rigid-body virtual field ($u_x^* = 1$, $u_y^* = 0$) in equation (6), and approximating integrals with discrete sums, one obtains a direct relationship between acceleration and average stress:

$$\overline{\sigma_{xx}}^y = \rho x_0 \overline{a_x}^{S_0} \quad (11)$$

where superscript y coupled with an overline denotes the width average at x_0 . Here, the superscript S_0 coupled with an overline denotes the surface average between the free edge and x_0 . The parameters for this equation are shown on the schematic in Figure 23. This equation is referred to as the ‘stress-gauge’ (SG) equation [11, 13, 14]. Equation 11 can be used for stiffness identification by plotting stress-strain curves at each cross-section of the sample. The elastic portion of the curve can then be linearly fitted to identify the stiffness, the strain term is different for each material model as discussed below.

Reduced Orthotropic Case: For this case $\overline{\sigma_{xx}}^y$ can be plotted against $\overline{\epsilon_{xx}}^y$ at any axial slice x_0 to produce a stress-strain curve. Linearly fitting the elastic response yields the transverse elastic modulus E_{22} .

Isotropic Case: Here, the average strain is given by $\overline{\epsilon_{xx} + \nu\epsilon_{yy}}^y$. This is plotted against the average stress $\overline{\sigma_{xx}}^y$ at all axial slices and linearly fitted to obtain the stiffness component Q_{11} . When using this approach it is necessary to know the Poisson's ratio ν . This is obtained using the manual or special optimised virtual fields method discussed previously, as in [13, 14]. If the test is sufficiently uni-axial then $\overline{\sigma_{xx}}^y$ can be plotted directly as function of $\overline{\epsilon_{xx}}^y$ and the results compare to the previous approach including the Poisson effect, see for example [55].

4.1.6 Virtual Fields for Failure Stress Identification

The use of virtual fields for failure stress identification relies on the use of rigid body virtual fields to reconstruct stress information where the material fails. The stress-gauge equation can be used as an initial estimate of tensile failure stress by reconstructing the average stress at the cross-section where the material fails. However, this is only useful for failure stress identification if the stress distribution is uniform over the sample height. Therefore, it is desirable to have stress information which can provide a more local estimate of stress throughout the material. In [12, 14] it was shown that combining the three independent rigid body virtual fields (rigid translation in x , rigid translation in y and rigid rotation) a linear approximation of the axial stress can be derived. This equation is referred to as the linear stress-gauge and is given as follows:

$$\sigma_{xx}(LSG) = \rho x_0 \overline{a_x} S_0 + \frac{12\rho x_0 y}{H^2} (\overline{a_{xy}} S_0 - \overline{a_y x} S_0 + x_0 \overline{a_y} S_0) \quad (12)$$

where ρ is the density of the material and surface averages of the acceleration fields are taken over the area S_0 shown in Figure 23.

While this gives a linear approximation of the axial stress the obvious question is ‘how well does this represent the real stress distribution?’. Fortunately, this can be assessed by comparing the stress calculated with the linear stress-gauge with the stress calculated from the strains using the constitutive law previously identified. It was shown in [12–14] that these two measures agree well when the material is loaded elastically. At the onset of non-linearity (*e.g.* plasticity, damage or failure) the assumptions of the constitutive law break down and these two measures of stress begin to diverge. Therefore, the stress at which this divergence occurs is used to estimate the tensile failure stress. Before describing the implementation of this theory in the IBII processing code it is necessary to generate test cases to validate the functionality of the identification routines. The test cases are generated using finite element models and synthetic image deformation as described in the following section.

4.2 Numerical Validation Models

In this section synthetic images will be generated to demonstrate the outputs and validate the IBII processing code. The advantage of this approach is that a finite element model with a known constitutive law can be encoded in the synthetic grid images. The material properties input into the finite element simulation then serve as reference values that can be compared to the identified values output by the code. Generally, inverse identification techniques such as the VFM are validated using data taken directly from a finite element model. However, the use of pure finite element data does not allow one to test the grid method procedure and data smoothing procedures which will be verified here using synthetic image data. This section briefly describes the finite element models and the procedure used to create the synthetic images for the two material models.

4.2.1 Finite Element Models

Two finite element models were implemented in Abaqus Explicit (v6.14). The first model was created to replicate the case of the reduced orthotropic material model using the material properties of carbon fibre impacted in the transverse direction similar to [12]. The material was modelled with the nominal properties of carbon fibre as $\rho = 1600 \text{ kg.m}^{-3}$, $E_{11} = 125 \text{ GPa}$, $E_{22} = 8.3 \text{ GPa}$, $G_{12} = 3.7 \text{ GPa}$ and $\nu_{12} = 0.3$. The second model replicates the case of an isotropic material using the nominal properties of tungsten carbide similar to the case in [14]. For this case the nominal material properties of tungsten carbide were used, $\rho = 14500 \text{ kg.m}^{-3}$, $E = 550 \text{ GPa}$ and $\nu = 0.24$. No strain rate sensitivity is modelled here so the input material parameters serve as reference values for comparison with the identified values with the VFM.

Both models were constructed as two-dimensional rectangular plates with dimensions $70 \times 44 \text{ mm}$ similar to the schematic shown in Figure 23. The plate was meshed with square CPS4R (2D, plane stress, reduced integration) elements with an edge length of 0.25 mm . Bulk viscosity damping was disabled and beta damping was applied to both models with a damping coefficient of $1 \times 10^{-8} \text{ s}$. Note that beta damping is necessary to ensure that the accelerations in the model are in equilibrium with the stress. A temporally-triangular pressure pulse was applied to one short edge of the rectangular plate with all other edges remaining free, as shown in Figure 23. For the first model (reduced orthotropic case) the pulse peak pressure was 200 MPa with a rise and fall time of $10 \text{ }\mu\text{s}$. For the second model (isotropic case) the peak pulse pressure was 1500 MPa with a rise and fall time of $8 \text{ }\mu\text{s}$. Displacement fields were extracted from each model at intervals of $0.5 \text{ }\mu\text{s}$ for the reduced orthotropic model and $0.2 \text{ }\mu\text{s}$ for the isotropic model. These data output intervals correspond to the frame rate that would be used for each experiment (*i.e.* 2 MHz for the reduced orthotropic case and 5 MHz for the isotropic case).

4.2.2 Generating Synthetic Grid Images

Synthetic grid images were generated using the displacements from the FE models using the analytical equation that describes the grey level intensity $G(x, y)$ of a sinusoidal grid, as follows:

$$G(x, y) = 2^b \left[I_0 + \frac{\gamma}{4} \left(1 + \cos \left(\frac{2\pi x}{p} \right) \right) \left(1 + \cos \left(\frac{2\pi y}{p} \right) \right) \right] \quad (13)$$

where I_0 is the average illumination expressed as a fraction of the dynamic range (between 0 and 1); γ is the pattern contrast amplitude expressed as a fraction of the dynamic range (between 0 and 0.5); b is the number of bits encoding the image; and p is the grid pitch. As the given description of the grid is analytical it is possible to deform the image directly by substituting the positions ‘ x ’ and ‘ y ’ with the deformed co-ordinates of each pixel ‘ $x - u_x$ ’ and ‘ $y - u_y$ ’. The u_x and u_y displacements are calculated at the pixel centroid by linearly interpolating the nodal displacements extracted from the FE model. A Matlab code for performing the image deformation using this approach is given in the dataset attached to this report (‘*main_GridImageDeformation.v1_0r.m*’). Here, the grid images were generated to replicate the parameters of the Shimadzu HPV-X camera with $400 \times 250 \text{ pixels}$. The grid pitch was set to 0.9 mm with a sampling of 5 pixels/period . The contrast of the grid pattern was set to such that 50% of the dynamic range was used based on previous analysis in [12–14].

It should be noted that there are more general methods for generating deformed images from an arbitrary pattern or experimental image. The method of sub-pixel interpolation has been used extensively in previous image deformation simulations as it can also be applied to speckle patterns and used to analyse Digital Image Correlation (DIC) data. This method is described in detail in refs. [29, 42, 43, 45]. For the grid method this approach also has advantages as it allows a real experimental grid image to be deformed. This will encode any defects that might be present on the real grid (*e.g.* missing pitches) or any slight errors in the real grid pattern/sampling. Note that the approach of sub-pixel interpolation is also required when deforming sharp grids (*i.e.* square rather

than sinusoidal) as describe in [44]. The drawback of this approach (for grids) is that the extra interpolation required makes it computationally intensive compared to the analytical approach described previously.

4.3 IBII Processing Code Implementation

4.3.1 Code Overview

An overview of the underlying functions and processes will be described, however, the main focus will be on functionality of the code, the required inputs from the user and output. A copy of the code (for Matlab R2017a) and all dependent functions can be found in the dataset detailed at the end of this report. The key steps to the processing code are summarised in the flow chart in Figure 24 and will be described individually in the following sections. Following the description of each key section in the code the associated outputs will be demonstrated using the synthetic grid images generated for each material model.

4.3.2 Input Processing Parameters

Before executing the main IBII test processing script (*'main_IBIIProcessing_v1_0r.m'*)⁵, the user must generate a processing parameters file (*processingParameters.mat*). Two scripts are included in the dataset which will produce example processing parameters files for the reduced orthotropic and isotropic material models (*'main_initProcessingParams_iso_v1_0r.m'* and *'main_initProcessingParams_redOrtho.v1_0r.m'* respectively). Many options in the initialisation file are purely cosmetic and only control formatting of figures output by the code as diagnostics. These parameters will not be discussed here and instead the user is referred to the documented scripts in the dataset. The focus here will be on the parameters that have to be changed by the user for each test and have a direct impact on the identified material properties. The key inputs from the user include:

1. grid pitch - specified in the *'grid'* data structure as *'grid.pitch'*;
2. time step (camera frame rate) - specified in the *'time'* data structure as *'time.frameRate'*;
3. material density - specified in the material data structure as *'material.rho'*; and
4. smoothing kernels (spatial (pixels) and temporal (frames)) - specified in the *'smoothingOpts'* data structure.

The user should think of the first three parameters as calibration factors. The grid pitch is the spatial calibration factor, the frame rate is the temporal calibration factor and the material density acts as a stress calibration factor (as in equation 11). The use of these parameters is indicated in Figure 24. The effect of smoothing is more complex due to the interaction of spatial and temporal effects. Previous studies have shown that the identification of stiffness parameters using the IBII test with good contrast images is relatively insensitive to smoothing, so long as the user does not select extreme values [13, 14]. A general guideline for the upper bound on spatial smoothing is ten grid pitches (in pixels) and for temporal smoothing the time (in frames) required for the compressive wave to traverse the length of the specimen. However, image deformation simulations are essential to fully understand the effect of smoothing and quantify error associated with the identifications for a given experimental setup and set of processing parameters. Apart from the key input previously discussed the user should also specify the material model and which modules of the code (*i.e.* which stiffness or failure stress identification procedures) are to be run using the *'globalOpts'* data structure. The final parameter the user needs to be aware of is that the code assumes the co-ordinate system shown in Figure 23 with the free edge of the sample on the left

⁵Scripts to be executed manually by the user are denoted with the prefix *'main_.'*, while sub-functions are denoted with the prefix *'func_.'*

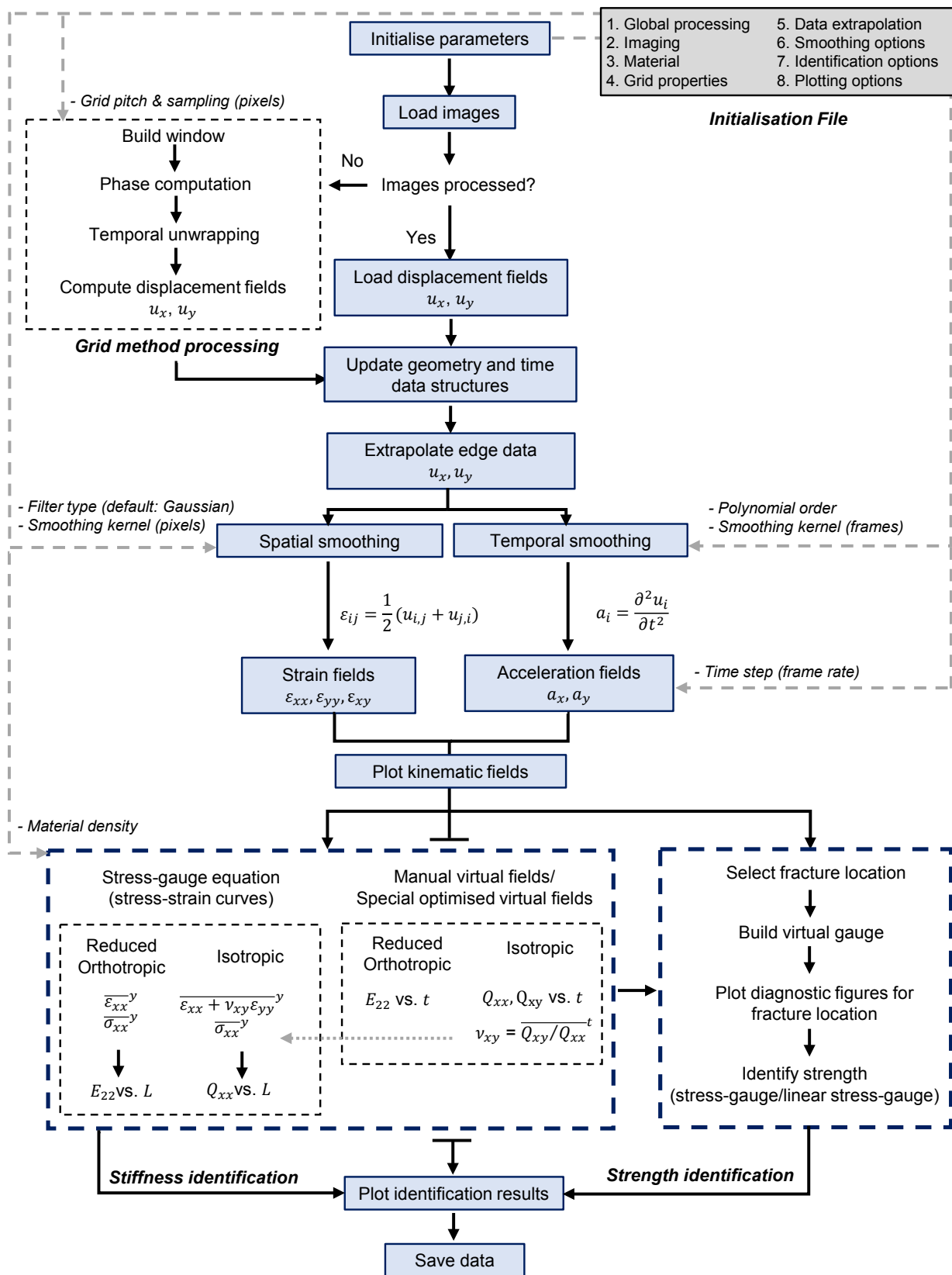


Figure 24: Flow chart describing the overall processing procedure implemented in Matlab code.

side of the sample. If the user specifies the free edge to be on the right side, the kinematic fields are flipped to conform to the coordinate system shown in Figure 23.

4.3.3 Initialisation and Data Input

For ease of data processing it is recommended that the user puts the image sequence from each test in its own folder with the associated processing parameters file. Once this is complete the main processing script can be run (*'main_IBIIProcessing.v1_0r.m'*). The first part of the code adds the default path for the folder containing all the required sub-functions. If this is not found the user is prompted to locate it manually. Once the dependent functions folder is added the code will prompt the user to select the first grid image in the test sequence using a file dialogue. The code then automatically looks for the file *'processingParameters.mat'* in the same directory as the images. After all the required files have been loaded the next step is to use the grid method to extract displacement fields from the raw images as described in the following section.

4.3.4 Grid Method Implementation

The raw bitmap images are processed using the grid method to obtain phase maps, from these the displacement field is extracted. An outline of the grid method procedure is given in the Section 3.2.2 and a detailed description of the mathematical formalism is given in [18]. The grid method code used here is freely available online and can be downloaded from: <http://www.thegridmethod.net/code>. The general steps in the grid method process are shown in Figure 24. The user has the option to calculate phase maps using the direct (method 1) or iterative (method 2) approaches as described in [18]. The iterative method accounts for irregularities or defects in the grid and should be used by default. Raw phase maps are discontinuous where the grid displaces more than one pitch, and therefore must be corrected using spatial and temporal unwrapping. The approach described in [34] was used to perform spatial unwrapping and temporal unwrapping was performed using an in-house Matlab function. The grid method section of the IBII code also creates the file *'specimenLocation.mat'*. This file contains the co-ordinates of the rectangular region selected by the user when processing the grid images. If the data is reprocessed the user will be prompted to automatically load the existing location file or select a new rectangular area. Note that the specimen location file is required to run the grid method script in an automated manner as required for parametric sweeps of image deformation data as described in Section 4.4.

In order to save time when the data is reprocessed the displacement fields obtained using the grid method are saved to the file *'GridMethod_ProcessedData.mat'* in the same directory as the raw image files. If the user processes the same specimen again the code will prompt the user to load the existing file or reprocess the images using the grid method.

4.3.5 Edge Extrapolation

Edge effects from the windowed Fourier transform cause one pitch of information on the border of the phase maps to be lost. Note that a similar problem is present for DIC data where one subset of data is lost on the edges of the sample. For the grid method, one pitch of displacement field data is missing in the direction of the field. That is, for the x displacement field one pitch of data is lost on the vertical edges but not on the horizontal edges. Previous studies have shown that identifications with the VFM can be drastically improved when this data is recovered using some sort of reconstruction rather than discarding the data [29,45]. This problem is more significant than usual here because of the low spatial resolution of the camera. Several methods were considered for reconstructing edge data using non-corrupted data near the edges: 1) two-point linear extrapolation based on data within two points next to the corrupt region as implemented in [12]; 2) extrapolation using a linear or quadratic regression fitting using 'N' defined points of good data near the edges; and 3) mesh extrapolation using the entire field of non-corrupt phase data to compute a surface fitting. For options 1) and 2) the extrapolation is performed independently for each row of pixels

(u_x fields), or column of pixels (u_y fields). To assess each approach, synthetic grid images were generated based on an FE simulation of the tests performed in [13]. In this study simulated displacement fields were used to deform synthetic images, which were processed using the grid method. Having access to the true signal within the corrupted region enables the goodness of each reconstruction method to be assessed quantitatively. From this study it was found that a linear regression fitting based on the data over one pitch inwards from the corrupted region (option 2 above) was best at reconstructing the signal and rejecting noise. If desired, the user may program in alternative edge reconstruction techniques. However, if the user is using a Shimadzu HPV-X or HPV-X2 camera the default settings in the processing parameters file are recommended.

4.3.6 Acceleration Calculation

The acceleration fields are obtained by temporally differentiating the displacement fields which have had the edge data reconstructed. The displacement fields are temporally smoothed first using a Savitsky-Golay filter with the Matlab function `'sgolayfilt'`. The polynomial order and length (in frames) of the filter are specified by the user in the `'smoothingOpts'` data structure in the initialisation file. In order to reduce edge effects from the Savitsky-Golay filter the default behaviour of the code is to pad the start of the displacement fields by one half of the kernel size (in frames). The smoothed fields are then differentiated twice in time to obtain acceleration maps. Temporal differentiation is performed twice using the `'gradient'` function in Matlab. The full-field acceleration data is then used directly in the VFM stiffness identification. When using the stress-gauge equation width averaged accelerations are required, by default these are calculated by averaging the full-field accelerations. The acceleration fields are stored in the data structure `'accel'` as three dimensional matrices where the dimensions of the matrix represent $[y, x, t]$. The `'accel'` data structure has fields `'accel.x'` and `'accel.y'`.

4.3.7 Strain Calculation

Strain fields are obtained by spatial differentiation of the displacement fields. Prior to differentiation, one pitch along the edges of the displacement field is reconstructed using the procedure described in the previous section. Spatial smoothing is also applied before differentiation. By default, spatial smoothing is performed with a Gaussian filter using the Matlab function `'imgaussfilt'`. The kernel size, in pixels, for the spatial smoothing filter is specified in the `'smoothingOpts'` data structure in the initialisation file. To mitigate edge effects coming from the Gaussian spatial filter the symmetric padding option is used by default. Once the displacement fields are smoothed spatially the fields are spatially differentiated using centred finite difference method implemented with the `'gradient'` Matlab function. Strain rate maps are then obtained by first temporally smoothing the strains using the same Savitsky-Golay filter parameters as for the acceleration. The strain fields are then temporally differentiated using a centred finite difference method. The data is also collapsed to a matrix containing width-averaged strains along the length of the specimen (rows) over time (columns) for plotting stress-strain curves with the stress-gauge equation. In a similar manner to the acceleration fields, the strain fields are stored in the data structure `'strain'` with fields `'strain.x'`, `'strain.y'` and `'strain.s'`.

4.3.8 Kinematic Field Outputs

The synthetic images for both material models were analysed using the IBII processing code. The synthetic images and all associated data output are provided in the dataset detailed at the end of this report. The processing parameters file for each case was generated to reflect the setup described by the FE model and synthetic grid generation (frame rate, grid properties *etc.*). All processing parameters were set as the default values apart from the addition of noise to the images and smoothing parameters, which were set based on previous experimental campaigns [13,14]. For the isotropic model the temporal filter was a 3rd order Savitsky-Golay filter over 11 *frames* and

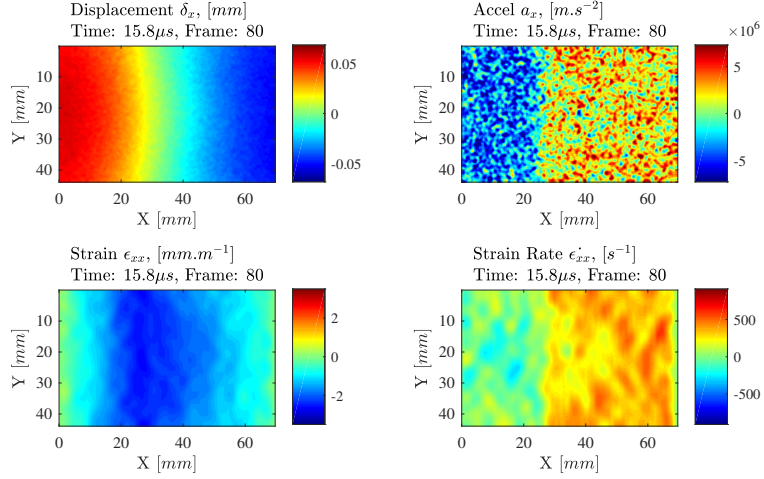


Figure 25: Example image taken from the first image sequence produced by the code for the isotropic test case.

the spatial filter was Gaussian with a total kernel width of 41 *pixels*. For the reduced orthotropic model the temporal filter was a 3rd order Savitsky-Golay filter over 11 *frames* and the spatial filter was Gaussian with a total kernel width of 25 *pixels*.

The code produces a number of image sequences showing the calculated kinematic fields (*i.e.* displacement, acceleration, strain and strain rate fields). The first image sequence contains only the ‘*x*’ components of the displacement, acceleration, strain and strain rate. An example output image is shown in Figure 25 for the isotropic model. The displacement shown in the image sequence has the rigid body motion of the sample removed by subtracting the average displacement over the whole field of view. Note that the displacement fields shown in all image sequences have not had any smoothing applied.

The following image sequences of the kinematic fields are produced by the IBII processing code, example outputs for each case are given in the referenced figures:

1. *x* components of displacement (u_x), acceleration (a_x), strain (ϵ_{xx}), and strain rate ($\dot{\epsilon}_{xx}$), see Figure 25;
2. displacement (u_x, u_y) and acceleration (a_x, a_y) fields, see Figure 26;
3. smoothed and un-smoothed strain components ($\epsilon_{xx}, \epsilon_{yy}, \epsilon_{xy}$), see Figure 27; and
4. strain and strain rate components ($\epsilon_{xx}, \epsilon_{yy}, \epsilon_{xy}$ and $\dot{\epsilon}_{xx}, \dot{\epsilon}_{yy}, \dot{\epsilon}_{xy}$), see Figure 28.

All output image sequences for both models are included in the dataset. To reduce the number of output image sequences (and reduce computation time) the parameter ‘*globalOpts.plotImageSeqs*’ can be set to ‘diagnostic’. In this case only the first image sequence will be plotted (*i.e.* just the ‘*x*’ component of the kinematic fields).

4.3.9 Stiffness Identification

The IBII processing code enables the user to identify material stiffness parameters from acceleration and strain maps using three VFM approaches: 1) manually-defined virtual fields; 2) special optimised virtual fields ; and 3) reconstructed stress and strain averages to fit stress-strain curves at each *x* coordinate from the free edge (*i.e.* using the stress-gauge equation).

Manual and special optimised virtual fields: The manual and special optimised VFM approaches provide a single set of stiffness components per time step, over the whole field of view.

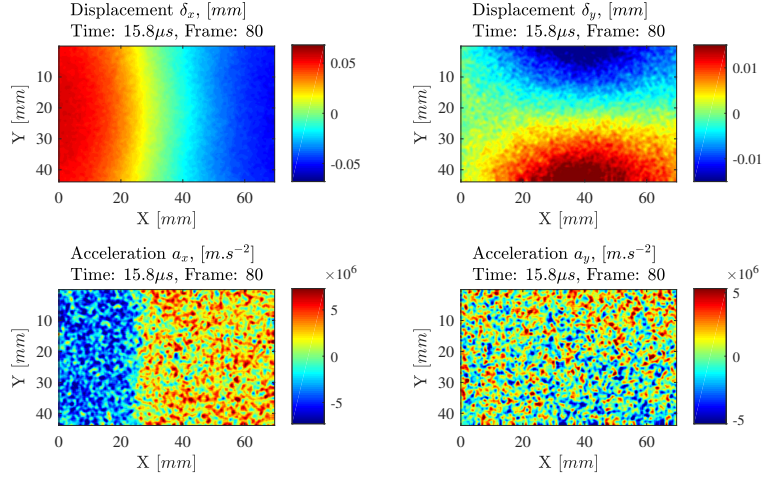


Figure 26: Example image taken from the second image sequence produced by the code for the isotropic test case.

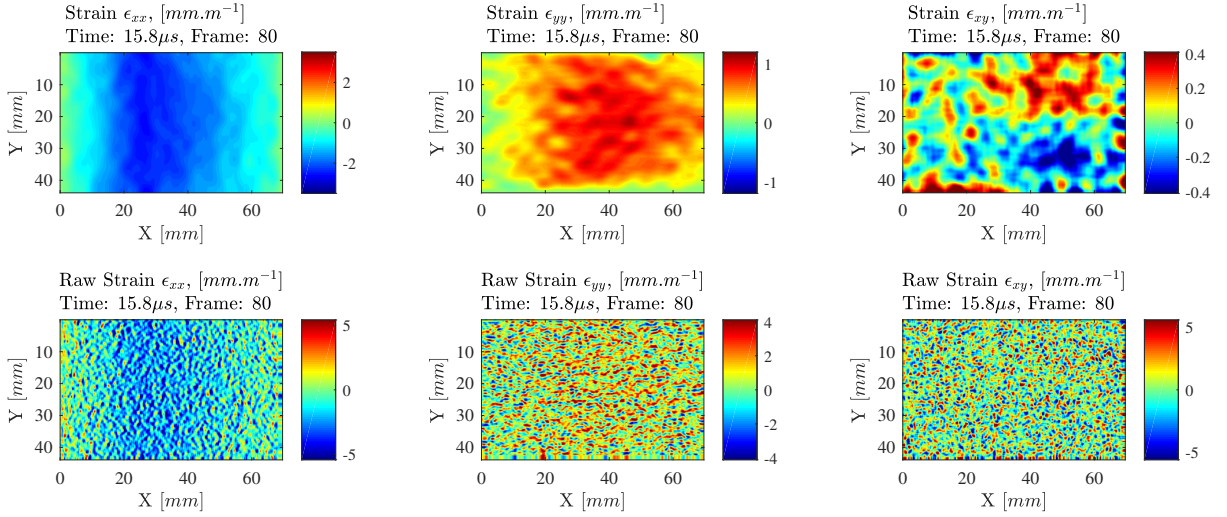


Figure 27: Example image taken from the third image sequence produced by the code for the isotropic test case.

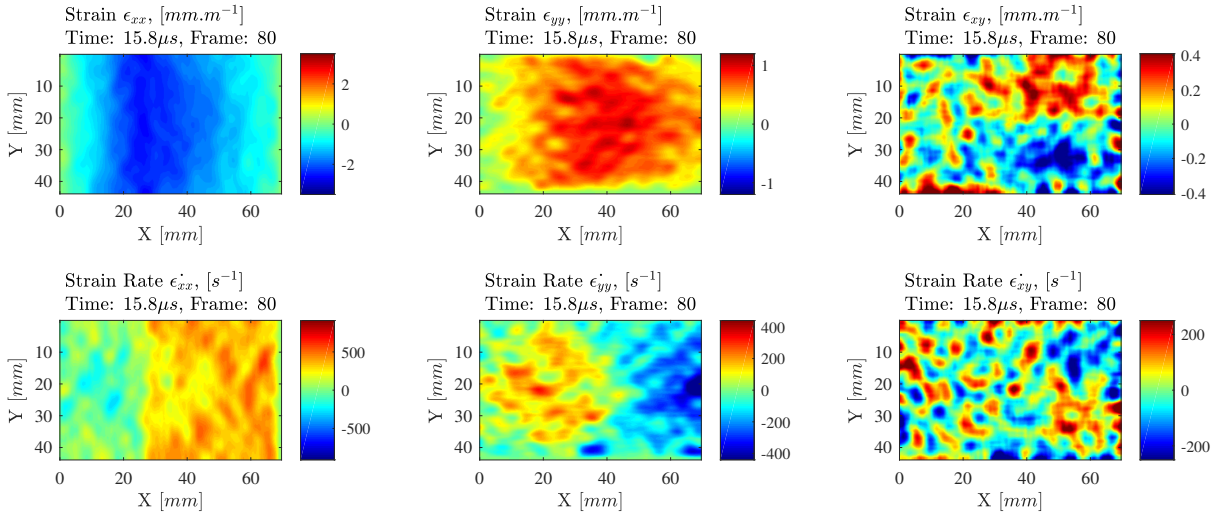


Figure 28: Example image taken from the fourth image sequence produced by the code for the isotropic test case.

For transversely isotropic materials, a ‘reduced’ virtual fields formulation is used. In this case, virtual fields are constrained to uniaxial virtual displacement. The result is a direct identification of E_{xx} from a_x and ϵ_{xx} fields only [12]. For isotropic materials, the a_y , ϵ_{yy} and ϵ_{xy} fields are also included in the formulation of the special optimised virtual fields. In this case, Q_{xx} and Q_{xy} are identified, from which E and ν are determined.

The special optimised virtual fields are formulated using a basis of piecewise functions (finite elements), as proposed in [54,56]. Independent sensitivity studies on previous IBII test data have shown that virtual meshes of 5x1 elements (x,y) and 5x4 elements (x,y) are a good starting point for processing reduced orthotropic and isotropic material models, respectively. The mesh density is defined in the initialisation file (‘*VFOpts*’ data structure). It is highly recommended that the user performs a virtual mesh refinement study using image deformation and/or experimental data to select optimal mesh densities for their specific experimental configuration. For both optimised virtual fields approaches the code was developed to discard data within one spatial smoothing kernel at the impact edge to reduce smoothing filter edge effects on the identification, and avoid edge reconstruction. This option can be turned off in the initialisation file (‘*VFOpts*’ data structure).

Compared to the other stiffness identification approaches the special optimised virtual fields method is more computationally intensive (calculation time on the order of several minutes rather than seconds). To reduce computation time when reviewing data between tests the user can disable the processing of the special optimised virtual fields using the flag in the ‘*globalOpts*’ data structure.

When using the manual or special optimised virtual fields, a single stiffness value can be identified by averaging over the time steps where the identification is most stable. Generally the identification is most stable with high strain and acceleration signal which occurs during the first compressive loading of the material. In the initialisation file the user can pre-select the range of times over which to average identified values (‘*VFOpts*’ structure). The default time range to identify an average stiffness using the manual or optimised virtual fields is set to be between 20% and 70% of the total recording time. The identified stiffness as a function of time and the average stiffness values identified are stored in the data structures ‘*identStiffVFMan*’ for the manual virtual fields and ‘*identStiffVFOpt*’ for the optimised virtual fields.

Stress-strain curves: In this approach the stress-gauge equation is used to calculate stress averages ($\overline{\sigma_{xx}}^y$) at each x coordinate from a_x fields. The stress average at any cross-section is combined with the average axial strain at the same cross-section. Each frame generates one point in the stress-strain space, and when plotted over time gives the full stress-strain response. For the orthotropic specimens, Poisson effects are neglected and the slope of $\overline{\sigma_{xx}}^y$ plotted against $\overline{\epsilon_{xx}}^y$ provides a direct identification of the elastic modulus in the matrix dominated direction (E_{22} for in-plane transverse testing and E_{33} for through-thickness testing) [12,13]. For isotropic materials, the slope of $\overline{\sigma_{xx}}^y$ plotted against $\overline{\epsilon_{xx} + \nu\epsilon_{yy}}^y$ provides a direct measurement of Q_{xx} . In the case of isotropic materials, the user has a choice of using a defined value for ν (stored in the ‘*material*’ data structure) or the identified value of ν from either the manual or special optimised virtual fields procedure. The default option is to use the Poisson’s ratio identified using the optimised virtual fields procedure. The stiffness identification procedure is automated to use a linear regression fit of the stress-strain curves up to the maximum compressive stress. Additional fitting options are available that allow the user to fit the tensile loading or threshold the fitting region based on the stress or strain. These options are specified in the ‘*stressGaugeOpts*’ data structure.

The stress-strain curves at every cross-section provide a spatial identification of stiffness. To obtain a single value for the stiffness for the whole test, the identified values can be averaged over the sample length. The identification tends to be poor near the free and impact edges due to extrapolated data, and edge effects from spatial smoothing. Therefore, the user may select identified values for averaging over a specified region of the sample (as a percentage of the length). This is specified in the ‘*stressGaugeOpts*’ data structure. The default is to average identified values over the middle 50% of the specimen. The stiffness as a function of position and the average identified

stiffness are stored in the data structure *'identStiffSG'*.

4.3.10 Stiffness Identification Outputs

Following the stiffness identification procedures a series of diagnostic figures are output by the IBII processing code. The example figures for the isotropic test case are shown below. Note that the data being analysed here is the synthetically deformed grid images for the isotropic case described in Section 4.2:

1. The input loading pulse calculated using equation 11, see Figure 29;
2. The identified stiffness components (as Q_{xx} , Q_{xy} and E, ν) as a function of time using manual virtual fields, see Figure 30;
3. The identified stiffness components as a function of time using the optimised virtual fields, see Figure 31;
4. Stress-strain curves constructed with the stress gauge equation, see Figure 32;
5. Linearly fitted stress-strain curves constructed with the stress gauge equation showing only the data range that is fitted and the fitted line, see Figure 33; and
6. Stiffness identified (as Q_{xx} and E) as a function of position from the free edge by fitting the stress-strain curves, see Figure 34.

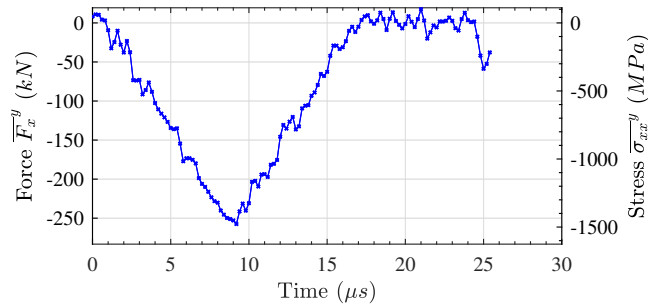


Figure 29: Applied loading pulse calculated using the average acceleration over the whole surface of the sample.

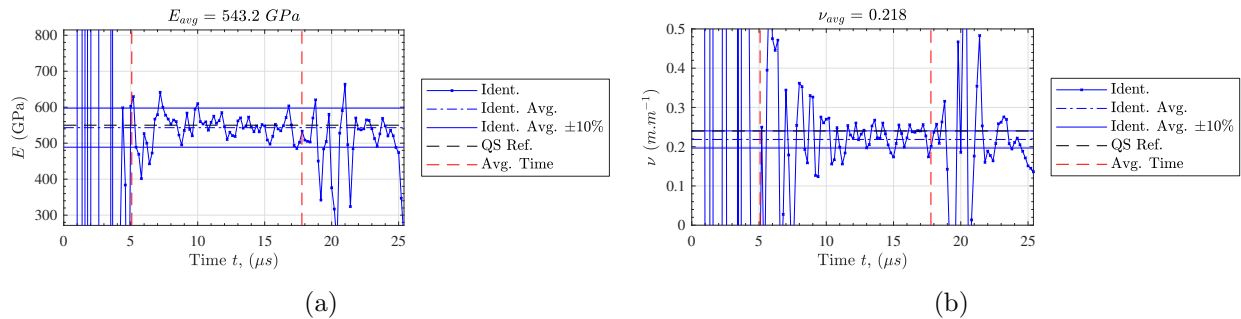


Figure 30: Stiffness identification over time using the manual virtual fields for the isotropic test case.

For the reduced orthotropic case only a single stiffness component is identified and the diagnostic figures only report results for E_{22} . The stiffness values input into the FE model serves as a comparison for the VFM identification. The FE reference value is shown by the horizontal line

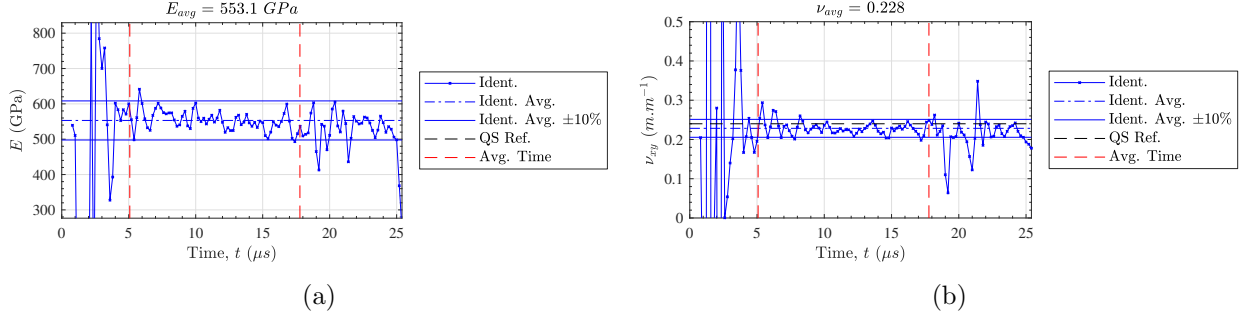


Figure 31: Stiffness identification over time using the optimised virtual fields for the isotropic test case.

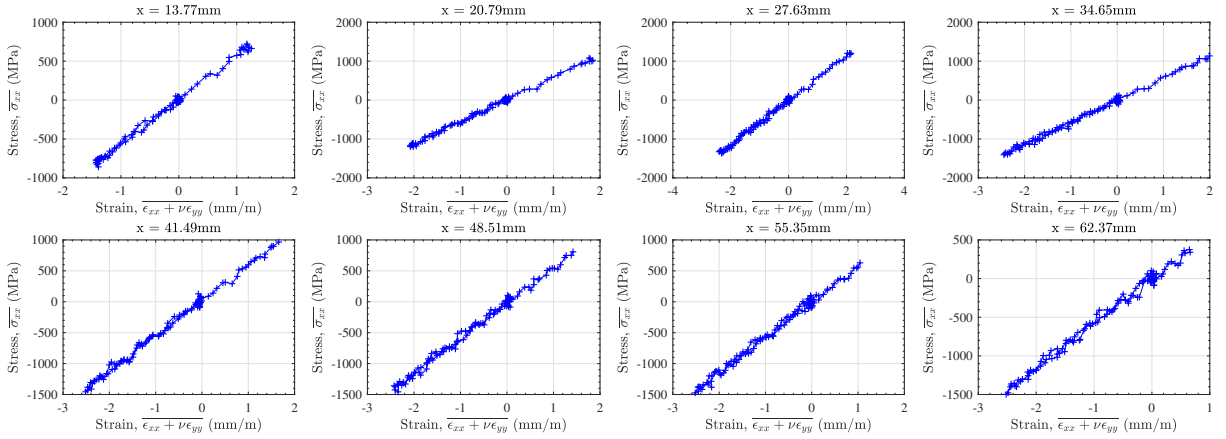


Figure 32: Stress-strain curves at various positions from the free edge. Note that $x = 0 \text{ mm}$ is the free edge location.

labelled ‘QS ref’ in all figures. When using the IBII processing code for real experimental data it can be useful to plot a quasi-static reference against identified stiffness to evaluate any strain rate sensitivity.

The output loading pulse and diagnostics from the stiffness identification can now be compared to the input parameters of the FE model to verify the functionality of the IBII processing code. The peak pressure of the triangular pressure in Figure 29 is 1496 MPa which compares well to the 1500 MPa pulse in the FE model. For the manual and optimised virtual fields the identification does not stabilise until there is enough acceleration and strain signal for a reliable identification. Analysis of Figures 30 and 31 shows some distinct differences between the manual and optimised virtual fields. The results for the optimised virtual fields stabilise earlier and remain stable for a longer duration. The difference between the manual and optimised virtual fields is more significant for the Poisson’s ratio where the variation in the identified value is significantly smaller for the optimised virtual fields. These differences are expected as the optimised virtual fields will focus on regions which are experiencing high strains, whereas the manual virtual fields act like a static filter (see ref. [12] for example). A comparison of the identified stiffness parameters for the isotropic test case is given in Table 3. The error for the identified elastic modulus is generally below 1% for except for the manually defined virtual fields. The error on the identified Poisson’s ratio is higher, which is not surprising given the target Poisson’s ratio is low and the strains are quite small for the isotropic test case (see Figure 27). Overall, the stability of the identification is remarkable for all cases given that the camera resolution (spatial/temporal) is modelled here as well as noise effects. These results validate the stiffness identification procedures are functioning correctly in the IBII processing code. Note that all output diagnostic figures for the reduced orthotropic test case can be found in the dataset.

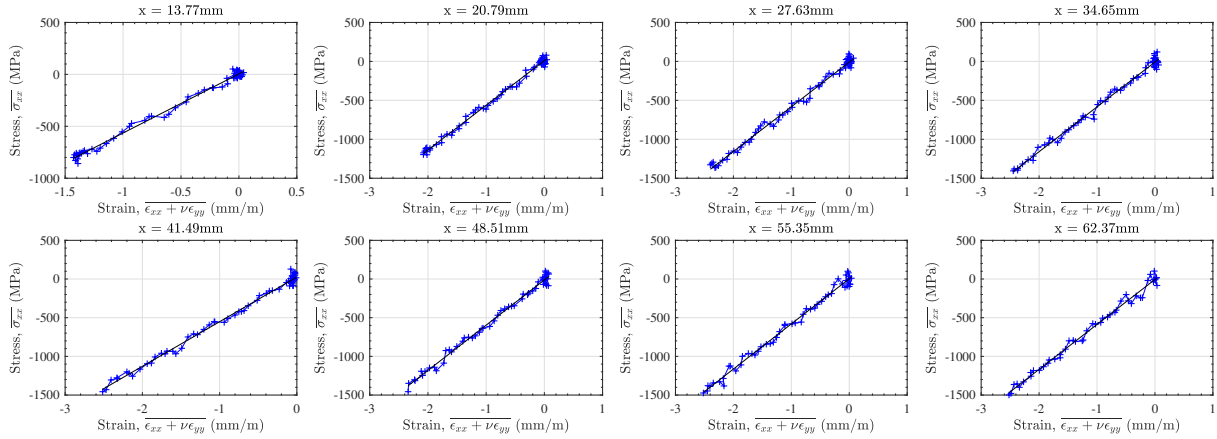


Figure 33: Linearly fitted stress-strain curves at various positions from the free edge. Note that $x = 0 \text{ mm}$ is the free edge location.

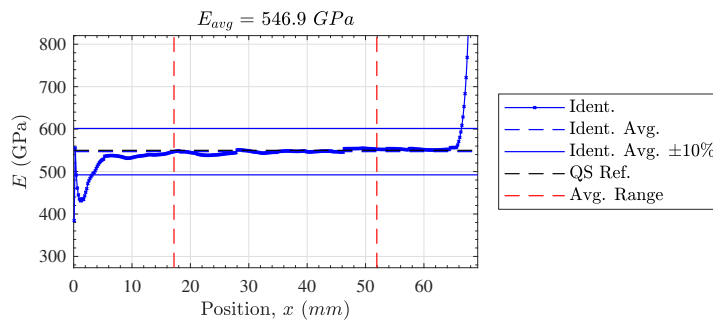


Figure 34: Stiffness identified by linearly fitting the stress-strain curves as a function of position from the free edge at $x = 0 \text{ mm}$.

4.3.11 Failure Stress Identification

The IBII processing code offers a failure stress identification procedure using the linear stress-gauge equation (equation 11) to give a local estimate of the failure stress. This method is designed to identify a tensile failure stress for brittle and quasi-brittle materials. The general methodology of this procedure is described in refs. [12–14]. In the following section only the isotropic test case will be considered. The same images and output for the reduced orthotropic case can be found in the dataset.

The first part of the failure stress identification requires the user to specify the location where the first crack forms. Initially, the user is asked to enter the frame when the first crack is clearly visible. This is best determined by reviewing the image sequence that contains all components of the raw (unsmoothed) strains (image sequence 3 described in Figure 27). The user is then prompted to manually enter the pixel coordinates of the crack or to select the location graphically on a heat map of the strain fields. The selected fracture location is then saved to the file *fracture.mat*. If the failure stress identification procedure is run on the same specimen again the user will be prompted to load the previous fracture location or select a new one.

A virtual gauge is then created and centred over the area selected by the user. The size of the virtual gauge defaults to 20 *pixels* in the x direction and 30 *pixels* in the y direction. The size of the virtual gauge can be specified by the user using the *strOpts* data structure created in the parameter initialisation file. The virtual gauge is used to average the kinematic data over the region where the crack forms to determine the failure stress.

Three stress-reconstructions are provided to the user in the failure stress diagnostics: 1) average stress along the cross-section where fracture occurs (stress-gauge equation), 2) the stress

Table 3: Comparison of identified material properties for the isotropic test case.

| | E (GPa) | E % diff. | ν | ν % diff. |
|--------------|--------------|----------------|-------|------------------|
| Reference | 550 | - | 0.24 | - |
| VF Manual | 543.2 | -1.24 | 0.218 | -9.00 |
| VF Optimised | 553.1 | -0.56 | 0.228 | -4.83 |
| Stress-Gauge | 546.9 | 0.57 | - | - |

reconstructed with the linear stress-gauge equation, and 3) stress reconstructed from strain using the identified stiffness parameters. These metrics are calculated at the exact fracture location specified by the user as well as averaged over the virtual gauge area. In general, the averages over the virtual gauge area are preferred as they are more robust to noise.

For brittle and quasi-brittle materials the IBII test is designed such that the sample remains linear elastic during the first transit of the compressive pulse across the sample. During this time the average stress calculated from the acceleration and from the strain should closely agree. Any divergence between the stress measures at this stage of the test is an indication of the overall test quality (see [12]). Specimens showing significant divergence should be discarded from any subsequent analysis. After the wave reflects and loads the sample in tension, the stress averages from strain and acceleration will initially follow each other until the point at which the sample cracks and fails in tension. At this point the strains become non-physical causing the stress calculated from the strain to diverge from the stress calculated from the acceleration. The maximum tensile stress after the two measures diverge is taken as the failure stress. This procedure works well for materials that do not exhibit significant non-linearity before failure as in refs. [13, 14].

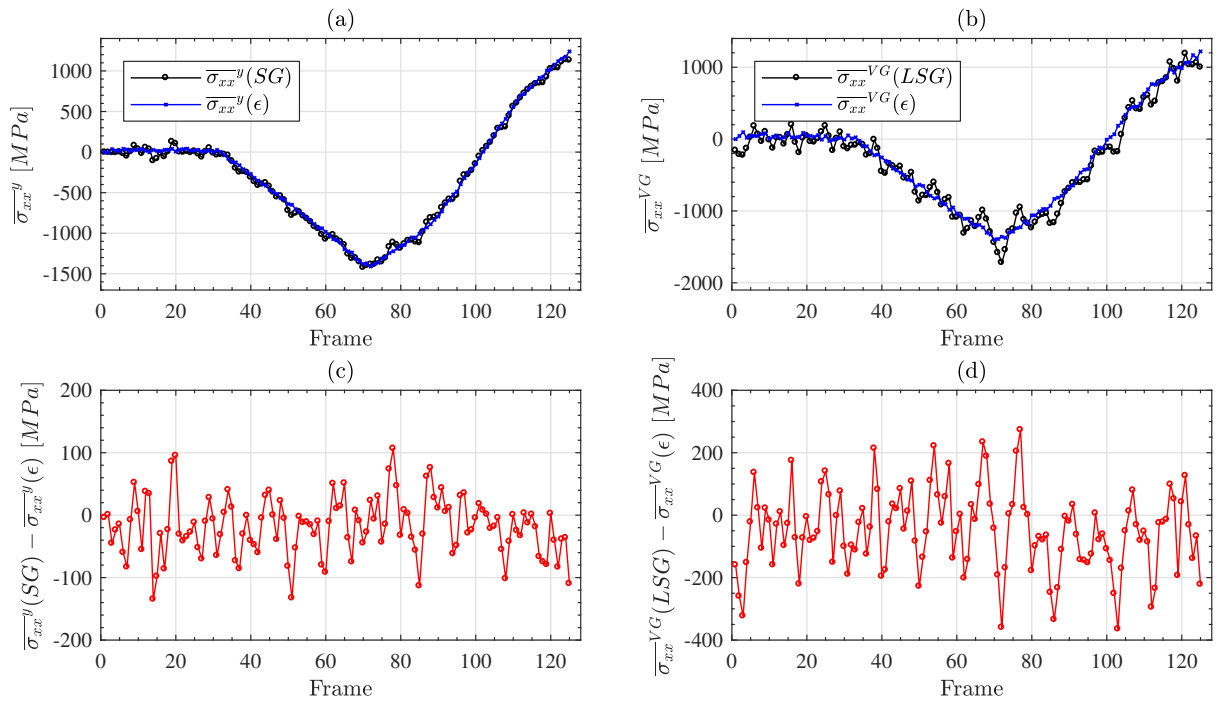


Figure 35: Failure stress identification diagnostic comparing stress averages from acceleration and strain. (a) Average stress over the vertical slice at the selected x coordinate. (b) Comparison of the average stress over the virtual gauge area. (c), (d) Difference between the stress measures.

For the simulated test case considered here, failure is not modelled so all stress measures will agree over the whole test duration as is shown in Figure 35. At the end of the test temporal edge

effects from the Savitsky-Golay filter corrupts the data over approximately half a smoothing kernel (5 frames in this case). Therefore, failure stress measurements should not be taken within a half a smoothing kernel of the end of the recorded images.

The simulated data is symmetric about the axial centreline of the specimen. Therefore, the second (moment) term in the linear stress-gauge equation (equation 12) is nominally zero and the linear stress-gauge and standard stress-gauge agree closely (equation 11). This is illustrated by comparing Figures 35 (a) and (b). However, the linear stress-gauge is noisier. This is caused by the contribution of the a_y acceleration to the moment term of the linear stress-gauge equation. As shown in Figure 26 the signal to noise ratio of the a_y acceleration is much smaller than that of the a_x component.

Two diagnostic image sequences are created during the failure stress identification procedure. Both sequences allow the user to compare the different stress measures over the test duration. The first sequence analyses the stress distribution over the axial slice at the selected fracture location. An example frame from this image sequence is shown in Figure 36. Figure 36 (a) shows a comparison of all stress measures over the sample width. This plot is useful for comparing the strain distribution with the linear stress-gauge equation to check how representative the linear approximation of the stress field is. For the test case shown in Figure 36 all stress measures agree closely apart from the effects of noise. The remaining plots show selected kinematic fields at the corresponding time point in the test. For all of the kinematic field plots in Figure 36 the axial slice of interest is shown using a dashed black line. The raw strain fields are provided in addition to the smoothed ones in this image sequence as it is much easier to see the point at which a crack forms on the raw strains.

The second image sequence compares the stress fields calculated from the strain with the stress field calculated using the linear stress-gauge equation. An example frame for the second diagnostic image sequence is shown in Figure 37. The virtual gauge area is shown on the stress fields in Figure 37 using a black rectangle. This image sequence also provides a comparison of the average stress in the virtual gauge area calculated using the strain or the linear stress-gauge equation in Figure 37 (c). The local stress-strain curve using the average stress and strain in the virtual gauge area is also provided in Figure 37 (d). During the image sequence the current point on Figure 37 (c) and (d) is shown using a red circle. In Figure 37 this corresponds to the point at which the maximum tensile stress was observed in the virtual gauge region. This frame of the test is also saved separately in the ‘*DiagnosticImages*’ folder so that the user can quickly access the frame at which the failure stress value was obtained. All failure stress identification information is stored in the data structure ‘*identStrength*’.

For failure stress analysis of experimental data, the linear stress gauge is generally preferred as the standard stress-gauge is likely to underestimate failure stress for cases when the stress-distribution is non-uniform across the height of the sample. This can occur when fracture occurs closer to the edges of the sample or when the pulse propagates at an angle to the impact edge. It is reiterated that the ability to measure the in-plane kinematic fields removes the requirement for a perfectly planar pulse for stiffness or failure stress identification. Here it should also be noted that the failure stress should not be taken directly from strain fields due to the uncertainty surrounding the exact time at which the strains become non-physical.

4.3.12 Final Output and Saved Data

The next section of the code has an optional module for plotting additional diagnostic image sequences that are not essential to the main functionality of the program. The main usage of these image sequences is for demonstrating the IBII processing procedure in conference presentations. An example frame for one of these image sequence is shown in Figure 38. The idea of this image sequence is to show the kinematic fields used to construct a stress-strain curve and concurrently plot the stress-strain curve at a given location. The first part of this image sequence (Figure 38 (a)) shows a stress-strain curve with the current time point indicated by a red circle. The remaining plots show the kinematic fields used to calculate the stress-strain curve as well as the strain rate

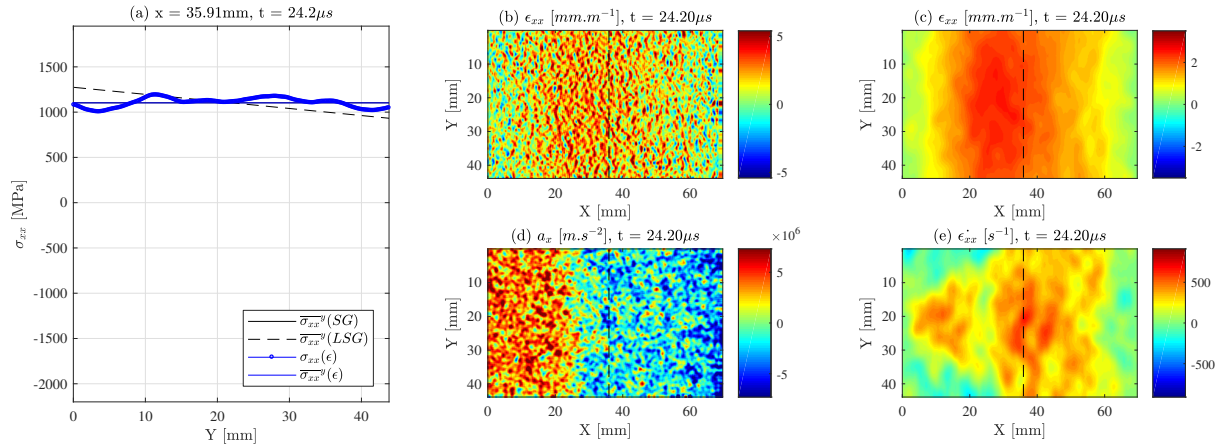


Figure 36: Example frame from the first diagnostic image sequence for failure stress identification. (a) Comparison of the stress measures at the axial section corresponding to the selected fracture location. (b)-(e) kinematic fields at the same time point with the section of interest shown using a black dashed line.

field. Figure 38 (b) shows the acceleration field used to calculate the average stress with the section of interest marked with a dashed black line. Figure 38 (c) shows the axial strain and Figure 38 (d) shows the axial strain rate. By default the section of interest corresponds to the location the user selected during failure stress identification. If the failure stress identification module is disabled the central section of the specimen is used.

The last section of the code saves all of the processed data to file for any subsequent processing. The file *'AllProcessedData.mat'* contains all output information including the kinematic fields. As the kinematic fields are three-dimensional matrices the file is relatively large. Therefore an additional file is saved, *'IdentifiedProperties.mat'*, that only contains the data structures relating to stiffness and failure stress identification. This file is much quicker to load and is useful for performing comparisons of the stiffness or failure stress identifications for multiple samples.

4.4 Image Deformation Simulations

As mentioned in Section 4.2 image deformation simulations provide a rational method for selecting optimal processing parameters for experiments involving full-field measurements. This section will provide an overview of the procedure for selecting optimal smoothing parameters for stiffness identification with the IBII test as previously implemented in [13,14]. Currently, the image deformation procedures implemented for the IBII method focus on minimising the error for the stiffness identification. It would be possible to implement a similar image deformation analysis for the failure stress identification using a cohesive zone finite element model. This will be implemented in a future paper analysing the data that has been previously collected using IBII test across a range of materials [12–14].

4.4.1 Image Deformation Procedure

The first step in the image deformation procedure is to develop a finite element model of the IBII test using the constitutive law to be identified. The displacement fields from the FE model are then encoded in a series of deformed grid images using the procedure described in Section 4.2.2. Here, the only isotropic test case will be considered as described in Section 4.2.1.

The deformed grid images are then processed using the same procedures described in Section 4.3. To quantify the effect of noise and smoothing (spatial and temporal), various smoothing kernel sizes were processed in a parametric sweep. As a general recommendation, the upper limit on the spatial smoothing kernel size should be approximately a quarter of the field of view (~ 100 pixels) or a

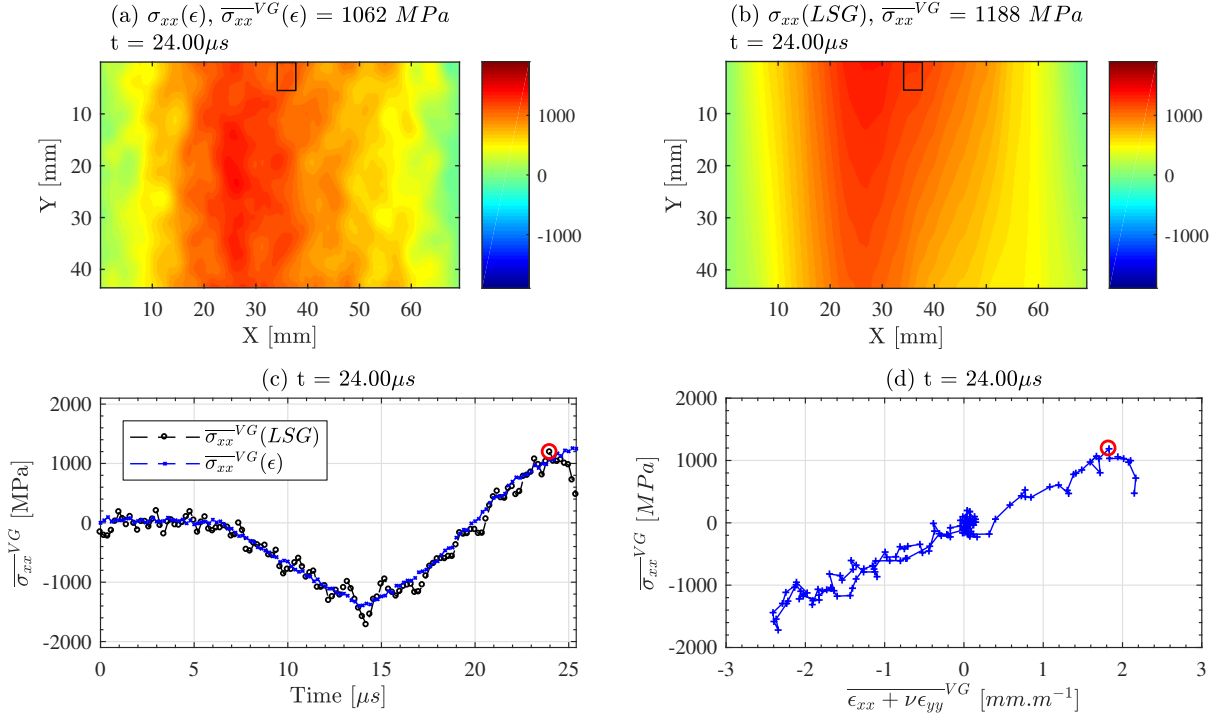


Figure 37: Example frame from the second diagnostic image sequence for failure stress identification. (a) Stress field calculated from the strains using the identified stiffness parameters and (b) from the linear stress σ_{xx} gauge equation. (c) Comparison of the stress measures averaged over the virtual gauge area. (d) Local stress-strain curve using the average data over the virtual gauge area.

quarter of the total recording time (~ 32 frames) for the temporal smoothing kernel. To reduce the computational cost of the sweep, it can also be useful to first run a coarse sweep over a broad range of kernels and then run a finer sweep to select the final processing parameters.

A Gaussian spatial filter was used and the smoothing kernel was swept between 0 and 51 pixels in increments of 10 pixels ($S_k = 0, 11, 21, \dots, 51$). A 3rd order Savitsky-Golay filter was used as a temporal filter and the kernel was swept between 0 and 25 frames in increments of 5 frames ($T_k = 0, 5, 11, \dots, 25$). Before running the identification for each combination of smoothing kernels, Gaussian white noise was added to the grey level images. Based on images taken with the HPV-X camera the standard deviation of the noise was conservatively set at 0.4% of the dynamic range. A total of 30 different iterations of noise are processed for each set of smoothing kernels. Statistical analysis of the 30 iterations for each combination of smoothing kernels is then used to assess the random and systematic error of the identification procedure. The optimal smoothing parameters are those which give the best compromise between the random and systematic errors. Here, only a coarse sweep will be considered using the isotropic test case.

This general procedure can also be used to investigate any other parameter of interest (*e.g.* camera frame rate, pixel array size or grid sampling). This allows the user to answer questions such as ‘What frame rate would I need to resolve accelerations in a high was speed material like boron carbide?’ or ‘What pixel array size do I need to resolve the strain gradients in my test with an error of less than 5%’ before running any experiments.

4.4.2 Error Analysis and Parameter Selection

The systematic error, Err_{sys} , for a given set of smoothing kernels is defined as the difference between the mean identified stiffness over the thirty iterations of noise $\overline{Q_{ij, ID}}$ and the stiffness input into the FE model, normalised by the stiffness of the FE model $Q_{ij, FE}$:

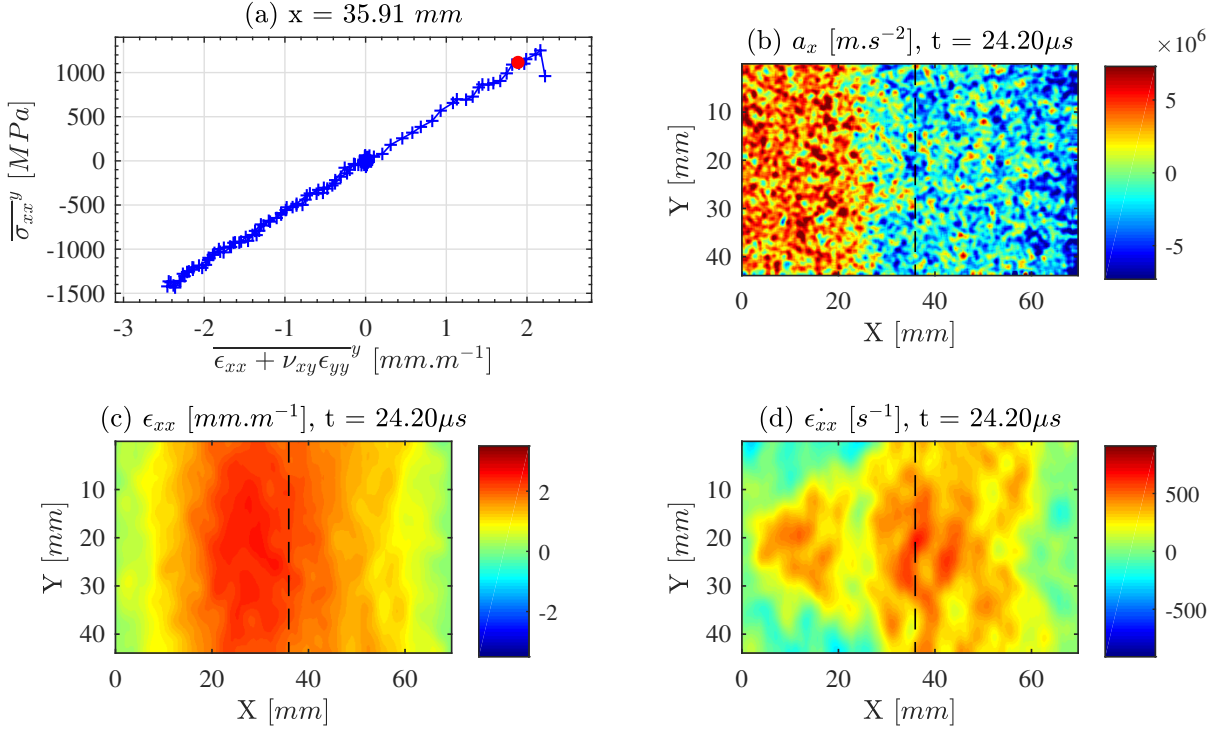


Figure 38: Example frame from the optional diagnostic image sequence. (a) Stress-strain curve at the location selected for failure stress identification. (b), (c) axial kinematic fields used for the calculation of the stress-strain curve and (d) the axial strain rate field. On (b)-(d) the section of interest is marked with a dashed black line.

$$Err_{sys} = \frac{(\overline{Q_{ij,ID}} - Q_{ij,FE})}{Q_{ij,FE}}, \quad ij = [xx, xy] \quad (14)$$

The systematic error can also be identified by processing noiseless images with no smoothing applied. Note that a comparison of the systematic error from noiseless images with the systematic error defined in equation 14 should be performed to assess if there is a noise induced bias on the systematic error. The random error, Err_{rnd} , is then given by the standard deviation of the identified stiffness over the thirty iterations normalised by the stiffness from the FE model:

$$Err_{rnd} = \frac{1}{Q_{ij,FE}} \sqrt{\frac{\sum_{k=1}^N (Q_{ij,ID}^k - \overline{Q_{ij,ID}})^2}{N-1}}, \quad ij = [xx, xy] \quad (15)$$

where N is the total iterations of noise (here $N = 30$) and $Q_{ij,ID}^k$ is the stiffness identified for the k^{th} iteration. The total error, Err_{tot} , is then defined by combining the systematic and random errors as follows:

$$Err_{tot} = \max(|Err_{sys} \pm 2Err_{rand}|) \quad (16)$$

The goal here is to select smoothing parameters that minimise the total error. Figure 39 shows the predicted error using the special optimised virtual fields to identify the stiffness components Q_{xx} and Q_{xy} . For this case the error is mainly driven by the temporal smoothing kernel. This result is expected as the special optimised virtual fields are only optimised to minimise the effect of strain noise not acceleration noise. Analysis of Figure 39 also shows that the predicted error for Q_{xy} is higher than Q_{xx} . This result is not surprising as the target Poisson's ratio is relatively low and accurately resolving the y strains is challenging (see Figure 27).

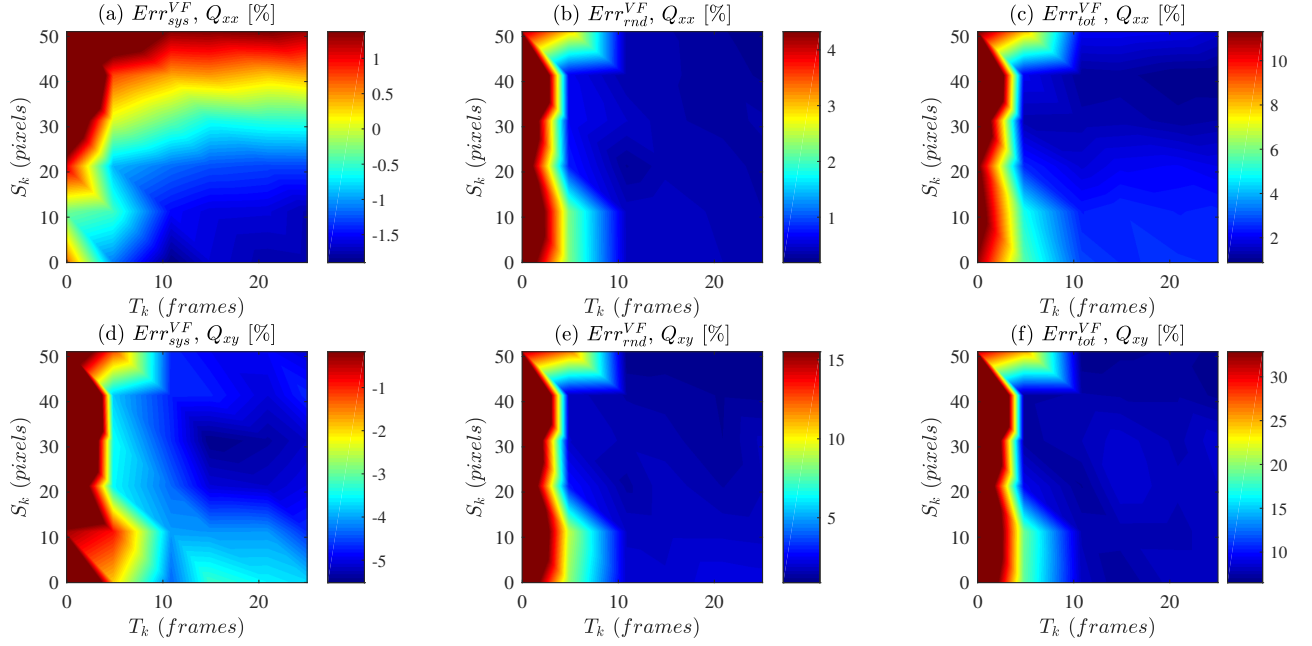


Figure 39: Error estimates from the parametric sweep for the isotropic model using the special optimised virtual fields. (a)-(c) Gives the systematic, random and total error estimates for the Q_{xx} stiffness and (d)-(f) gives the error estimates for the Q_{xy} stiffness.

Figure 40 shows the predicted error when identifying the stiffness component Q_{xx} using the stress-strain curves generated using the stress gauge equation. Here, the systematic error seems to be controlled primarily by the spatial smoothing kernel with only a weak dependence on the temporal smoothing kernel. This is not surprising as the stress-strain curve approach uses all temporal data points to fit a straight line and therefore contains built-in temporal regularisation. Applying even a small amount of spatial smoothing reduces the predicted systematic error below 5%. Analysis of the random error shows that applying even a small amount of spatial or temporal smoothing drastically reduces the estimated random error to be mostly less than 1%.

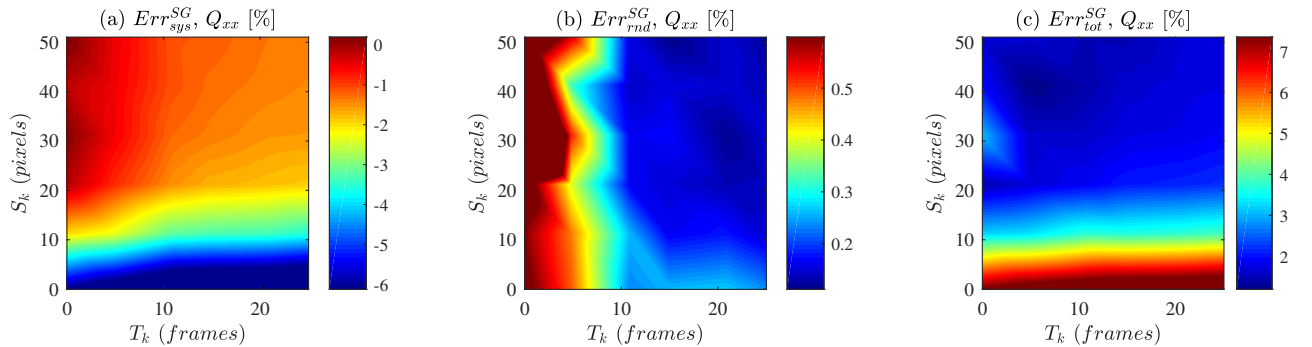


Figure 40: Error estimates from the parametric sweep for the isotropic model using the stress-gauge equation.

It can be desirable to select smoothing parameters that give a near optimal compromise for both stiffness identification procedures. This can be achieved by combining the total estimated error for the optimised virtual fields and the stress-gauge as follows: $Err_{comb} = \max(Err_{tot}^{VF}, Err_{tot}^{SG})$. The combined error is shown in Figure 41. The absolute minimum combined error is 2.2% when using a spatial smoothing kernel of $S_k = 41$ pixels and a temporal smoothing kernel of $T_k = 11$ frames. These smoothing parameters were used to process the data shown previously in Section 4.3. It should be noted here that generally it is also desirable to minimise the overall size of the spatial

and temporal smoothing kernels to reduce the impact of edge-effects on the identification. Thus, it can be beneficial to select smaller smoothing kernels that have a similar estimated error to the true minimum as in [14]. Finally, when a set of smoothing parameters has been selected, error bars are available from this process as well. It was shown in [57] that these error bars were realistic.

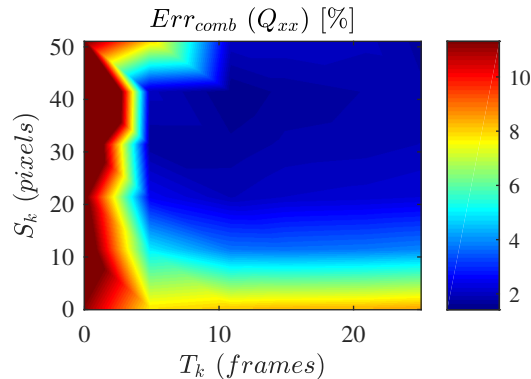


Figure 41: Combined total error for the special optimised virtual fields and the stress-gauge equation stiffness identification for Q_{xx} .

4.4.3 Parametric Sweep Code

The dataset contains a Matlab program for performing the parametric sweep of smoothing parameters for the IBII test called *'main_SmoothingSweep_Run_SPMD_v1_0r.m'*. The user should already have generated a series of deformed grid images using the program and method described in Section 4.4.1. Before running a full parametric sweep the deformed grid images should be first processed using the standard IBII processing code without any noise or smoothing applied. This serves two main functions 1) the IBII code will generate a file called *'specimenLocation.mat'* which is used by the parametric sweep program to automatically select the specimen location within the field of view to fully automate the grid method processing; and 2) this allows the user to verify that the FE model was correctly encoded in the grid images by analysing the diagnostic output from the standard IBII code. If there is an issue generating the synthetic grid images this can manifest as artificial fringes in the kinematic fields and/or anomalies in the stiffness identification. This analysis also gives the systematic error associated with the cameras spatial and temporal resolution without the effects of noise.

In order to reduce computation time the parametric sweep program uses the distributed computing toolbox in Matlab. Each combination of smoothing kernels and each processed iteration of noise is independent so multiple simulations can be run in parallel. The specific Matlab function used to achieve parallelisation is *'spmd'*. The user must specify the number of 'workers' to be created, which should be less than or equal to the number of available cores on the computer. The program assigns each combination of smoothing kernels to a different 'worker' distributing them as evenly as possible. For the case considered previously a total of 6 spatial kernels and 6 temporal kernels were simulated giving a total of 36 different combinations. Running this on a standard quad-core processor allows the user to assign 9 different combinations to each worker. For the isotropic case the sweep took just under 18 hours on a standard quad core desktop computer. Using a high performance work station the sweep time can be drastically reduced, with an 18 core system the same sweep took only 4 hours. Note that the identification for the reduced orthotropic case is significantly faster as only a single stiffness parameter is identified.

The simulation loop of the parametric sweep program uses the functions already implemented in the IBII processing code following the general methodology described previously. The main difference being that the modules for outputting image sequences and other diagnostic are removed to reduce computation time and data storage requirements. The only variables that are

retained for each iteration are the data structures associated with the identified stiffness components: *'identStiffVFMan'*, *'identStiffVFOpt'* and *'identStiffSG'*. Each worker will print to the console an information block detailing the current simulation that is running (*i.e.* the current smoothing parameters and iteration number). The previous iteration time is also displayed along with a projected completion time based on the average time to complete a single iteration.

Following the completion of the main simulation loop the parametric sweep program takes the data from each worker and combines it into a single cell array for later processing. This step is critical because the composite data structures which hold the data for each worker are completely lost when the parallel pool times out. A final program *'main_analyseImageDefSweep_SPMD_v1_0b.m'* can then be used to read the data from the sweep and plot the error maps shown in Figures 39, 40 and 41 allowing the user to select the smoothing kernels giving the smallest total error.

5 Conclusion

This report gives a detailed description of the implementation of the IBII test. The report was presented in three parts which covered the main aspects of implementing the test method including 1) design of a purpose-built gas gun impact apparatus, 2) experimental implementation of the IBII test and 3) VFM theory and data processing for IBII tests. We hope that the detailed account of our experience performing IBII tests given in this report will help researchers and engineers wanting to implement this method avoid some common pitfalls. In the future, ultra-high speed camera technology will improve opening up exciting new areas for using IBII-like tests to investigate more complex material behaviour such as interfaces and heterogeneous materials. The design space for this type of test is vast and we hope this report allows for the transfer of this technique to the wider experimental mechanics community so that others can build on and extend the IBII method to investigate new challenges in the dynamic behaviour of materials.

Acknowledgements

The authors would like to thank the group design project students Olivia Fan-Barrett, Joseph Perry, Matthew Leng, Keller Waud and Alexander Conway who produced the initial concept design of the gas gun detailed in this paper. The authors would also like to thank Dr Yves Surrel and the manager of the University of Southampton Print Centre, Mr Ian Wilcox, who developed the procedure for printing grids directly onto the samples. The authors are also grateful to the electronics workshop senior technical officer Lawrence Miles who implemented the electronics for the solenoid valve relays and light gate speed measurement system. The authors also want to thank Prof. Clive Siviour from the University of Oxford for useful tips and conversations over the years on the topic of dynamic testing of materials. Finally, the authors would like to thank Mr Sam Parry for helping to develop the top-down alignment procedure. Dr Lloyd Fletcher and Prof. Fabrice Pierron acknowledge support from EPSRC through grant EP/L026910/1. Jared Van Blitterswyk acknowledges PhD funding support from EPSRC.

Data Provision

All data supporting this report are openly available from the University of Southampton repository at: <http://dx.doi.org/10.5258/SOTON/D1053>. The dataset contains the following:

1. Design drawings for the gas gun, specimen holder and experimental components.
2. Simulink model used for the gas gun design.
3. Labview program for controlling the gas gun and Arduino code for projectile speed measurement and triggering the flash.

4. Postscript files for producing printed grids of various pitches.
5. Matlab programs for analysing grid sampling and out of plane movement tests.
6. Example images of printed grids taken with the Shimadzu HPV-X camera for comparison during set up.
7. Matlab programs for analysing IBII test data including: the main IBII processing code; a program for producing deformed grids from finite element data; and a program for running smoothing parameter sweeps.

Appendix I: List of Equipment for IBII Testing

Impact loading apparatus:

- Gas gun or other impact loading apparatus (*e.g.* Hopkinson bar with the output bar removed), see Section 2.1 for general requirements.
- Arduino and light gate system for measuring projectile speed and synchronising the lightning and camera system, see Sections 2.11 and 3.3.1.
- Specimen mounting system using precision mechanical stages for alignment, see Section 3.1.
- Alignment rod for initial alignment of the specimen mounting stages, see Section 3.1.
- Polished metal mirror and mounting system for top-down alignment shots, see Section 3.1.

Specimen and other components, see Section 3.4.2:

- Test specimen with a suitable grid pattern applied, see Section 3.2.3 for grid deposition techniques.
- Projectiles and sabots.
- Waveguides with prepared contact triggers requiring:
 - Copper tape
 - Double sided tape
 - Wire, 0.2 mm^2
 - Solder and soldering iron
- Wedge shaped foam stands.
- Cyanoacrylate glue for bonding the specimen to the waveguide, Loctite 422 is recommended for most applications.
- Set square and ruler for aligning samples on the wave guide.

Imaging equipment:

- Shimadzu HPV-X camera
- Computer for controlling the camera with:
 - ImageJ for analysing alignment shots
 - Matlab R2017a or higher
 - The grid sampling and out of plane movement codes for checking the grid setup, these can be found in data repository
- Sigma 105mm lens or appropriate lens for the selected sample geometry.
- Translation stage for mounting the camera.
- Camera tripod.
- Bowens Gemini 1000Pro flash or other suitable lighting system.
- Flash tripod.
- BNC cables for connecting the flash to the camera and for connecting the copper contact trigger to the camera.

- Voltage conversion box to convert 5 V from the camera to the 10 V required by the flash.
- Two small dual axis spirit levels to aid the process of aligning the camera.
- Tape measure or ruler for setting initial working distance of the camera based on required magnification.

Data processing equipment:

- Standard desktop computer with:
 - Matlab R2017a or higher.
 - IBII processing code listed in the data repository

References

- [1] H. Kolsky. An investigation of the mechanical properties of materials at very high rates of loading. *Proceedings of the Physical Society. Section B*, 62(11):676, 1949.
- [2] H. Kolsky and L. S. Douch. Experimental studies in plastic wave propagation. *Journal of the Mechanics and Physics of Solids*, 10(3):195–223, July 1962.
- [3] L. Djapic Oosterkamp, A. Ivankovic, and G. Venizelos. High strain rate properties of selected aluminium alloys. *Materials Science and Engineering: A*, 278(1):225–235, February 2000.
- [4] R. W. Armstrong and S. M. Walley. High strain rate properties of metals and alloys. *International Materials Reviews*, 53(3):105–128, May 2008.
- [5] M. A. Sutton, A. Gilat, J. Seidt, S. Rajan, and A. Kidane. Full field deformation measurements in tensile Kolsky bar experiments: studies and detailed analysis of the early time history. *Journal of Dynamic Behavior of Materials*, pages 1–19, January 2018.
- [6] B. A. Gama, S. L. Lopatnikov, and J. W. Gillespie. Hopkinson bar experimental technique: a critical review. *Applied Mechanics Reviews*, 57(4):223–250, October 2004.
- [7] S. L. Lopatnikov, B. A. Gama, K. Krauthouser, and J. W. Gillespie. Applicability of the classical analysis of experiments with split Hopkins pressure bar. *Technical Physics Letters*, 30(2):102–105, 2004.
- [8] L.G. Melin and L.E. Asp. Effects of strain rate on transverse tension properties of a carbon/epoxy composite: studied by moiré photography. *Composites Part A: Applied Science and Manufacturing*, 30(3):305–316, March 1999.
- [9] J. Neumayer, P. Kuhn, H. Koerber, and R. Hinterhölzl. Experimental determination of the tensile and shear behaviour of adhesives under impact loading. *The Journal of Adhesion*, 92(7-9):503–516, September 2016.
- [10] A. Gilat, T. E. Schmidt, and A. L. Walker. Full field strain measurement in compression and tensile split Hopkinson bar experiments. *Experimental Mechanics*, 49(2):291–302, April 2009.
- [11] F. Pierron, H. Zhu, and C. Siviour. Beyond Hopkinson’s bar. *Philosophical Transactions of the Royal Society of London A: Mathematical, Physical and Engineering Sciences*, 372(2023), August 2014.
- [12] L. Fletcher, J. Van-Blitterswyk, and F. Pierron. A novel image-based inertial impact test (IBII) for the transverse properties of composites at high strain rates. *Journal of Dynamic Behavior of Materials*, 5(1):65–92, March 2019.

- [13] J. Van Blitterswyk, L. Fletcher, and F. Pierron. Image-based inertial impact test for composite interlaminar tensile properties. *Journal of Dynamic Behavior of Materials*, 4(4):543–572, December 2018.
- [14] L. Fletcher and F. Pierron. An image-based inertial impact (IBII) test for tungsten carbide cermets. *Journal of Dynamic Behavior of Materials*, 4(4):481–504, December 2018.
- [15] F. Pierron and M. Grédiac. *The virtual fields method: extracting constitutive mechanical parameters from full-field deformation measurements*. Springer, New York, March 2012.
- [16] H. Zhu and F. Pierron. Exploration of Saint-Venant’s principle in inertial high strain rate testing of materials. *Experimental Mechanics*, 56(1):3–23, January 2016.
- [17] M. Grédiac, B. Blaysat, and F. Sur. A critical comparison of some metrological parameters characterizing local digital image correlation and grid method. *Experimental Mechanics*, 57(6):871–903, July 2017.
- [18] M. Grédiac, F. Sur, and B. Blaysat. The grid method for in-plane displacement and strain measurement: a review and analysis. *Strain*, 52(3):205–243, June 2016.
- [19] Z. J. Rohrbach, T. R. Buresh, and M. J. Madsen. Modeling the exit velocity of a compressed air cannon. *American Journal of Physics*, 80(1):24–26, January 2012.
- [20] A. Cave, S. Roslyakov, M. Iskander, and S. Bless. Design and performance of a laboratory pneumatic gun for soil ballistic applications. *Experimental Techniques*, 40(2):541–553, April 2016.
- [21] N. K. Bourne. A 50 mm bore gas gun for dynamic loading of materials and structures. *Measurement Science and Technology*, 14(3):273, 2003.
- [22] J. R. Brown, P. J. C. Chappell, G. T. Egglestone, and E. P. Gellert. A gas-gun facility for material impact studies using low-velocity, low-mass projectiles. *Journal of Physics E: Scientific Instruments*, 22(9):771, 1989.
- [23] M. de Icaza, C. Renero, and F. E. Prieto. Design operation and test of a light gas gun in a developing country. *Review of Scientific Instruments*, 60(10):3284–3292, October 1989.
- [24] G. R. Fowles, G. E. Duvall, J. Asay, P. Bellamy, F. Feistmann, D. Grady, T. Michaels, and R. Mitchell. Gas gun for impact studies. *Review of Scientific Instruments*, 41(7):984–996, July 1970.
- [25] Solenoid Valve World, 2018. <http://www.solenoid-valve.world/>.
- [26] A. Trujillo-Pino, K. Krissian, M. Alemán-Flores, and D. Santana-Cedrés. Accurate subpixel edge location based on partial area effect. *Image and Vision Computing*, 31(1):72–90, January 2013.
- [27] F. Pierron and P. Forquin. Ultra-high-speed full-field deformation measurements on concrete spalling specimens and stiffness identification with the virtual fields method. *Strain*, 48(5):388–405, October 2012.
- [28] F. Pierron, R. Chérigène, P. Forquin, R. Moulart, M. Rossi, and M. A. Sutton. Performances and limitations of three ultra high-speed imaging cameras for full-field deformation measurements. *Applied Mechanics and Materials*, 70:81–86, 2011.
- [29] M. Rossi, F. Pierron, and P. Forquin. Assessment of the metrological performance of an in situ storage image sensor ultra-high speed camera for full-field deformation measurements. *Measurement Science and Technology*, 25(2):025401, February 2014.

- [30] V. Tiwari, M. A. Sutton, and S. R. McNeill. Assessment of high speed imaging systems for 2d and 3d deformation measurements: methodology development and validation. *Experimental Mechanics*, 47(4):561–579, August 2007.
- [31] R. Moulart, F. Pierron, S. R. Hallett, and M. R. Wisnom. Full-field strain measurement and identification of composites moduli at high strain rate with the virtual fields method. *Experimental Mechanics*, 51(4):509–536, November 2010.
- [32] E.M.C. Jones and M.A. Iadicola, editors. *A Good Practices Guide for Digital Image Correlation*. International Digital Image Correlation Society, 2018.
- [33] F. Sur and M. Grédiac. Influence of the analysis window on the metrological performance of the grid method. *Journal of Mathematical Imaging and Vision*, 56(3):472–498, November 2016.
- [34] M. A. Herráez, D. R. Burton, M. J. Lalor, and M. A. Gdeisat. Fast two-dimensional phase-unwrapping algorithm based on sorting by reliability following a noncontinuous path. *Applied Optics*, 41(35):7437–7444, December 2002.
- [35] The grid method - code, 2018. <http://www.thegridmethod.net/code>.
- [36] J.-L. Piro and M. Grédiac. Producing and transferring low-spatial-frequency grids for measuring displacement fields with moiré and grid methods. *Experimental Techniques*, 28(4):23–26, July 2004.
- [37] B. Erzar and P. Forquin. An experimental method to determine the tensile strength of concrete at high rates of strain. *Experimental Mechanics*, 50(7):941–955, September 2010.
- [38] F. Davis, L. Fletcher, and F. Pierron. Inertial impact tests to identify the plastic properties of metals. In *EPJ Web of Conferences*, volume 183, page 02051, 2018.
- [39] P.L. Reu. Stereo-rig design: lens selection – part 3. *Experimental Techniques*, 37(1):1–3, January 2013.
- [40] F. Sur, B. Blaysat, and M. Grédiac. Determining displacement and strain maps immune from aliasing effect with the grid method. *Optics and Lasers in Engineering*, 86:317–328, November 2016.
- [41] R. Kuroda and D. Sugawa. Cameras with on-chip memory CMOS image sensors. In K. Tsuji, editor, *The Micro-World Observed by Ultra High-Speed Cameras: We See What You Don't See*, pages 103–124. Springer International Publishing, Cham, 2018.
- [42] P. Lava, S. Cooreman, S. Coppieters, M. De Strycker, and D. Debruyne. Assessment of measuring errors in DIC using deformation fields generated by plastic FEA. *Optics and Lasers in Engineering*, 47(7–8):747–753, July 2009.
- [43] P. Lava, S. Cooreman, and D. Debruyne. Study of systematic errors in strain fields obtained via DIC using heterogeneous deformation generated by plastic FEA. *Optics and Lasers in Engineering*, 48(4):457–468, April 2010.
- [44] M. Rossi and F. Pierron. On the use of simulated experiments in designing tests for material characterization from full-field measurements. *International Journal of Solids and Structures*, 49(3):420–435, February 2012.
- [45] M. Rossi, P. Lava, F. Pierron, D. Debruyne, and M. Sasso. Effect of DIC spatial resolution, noise and interpolation error on identification results with the VFM. *Strain*, 51(3):206–222, June 2015.

- [46] B. Lukić, D. Saletti, and P. Forquin. Use of simulated experiments for material characterization of brittle materials subjected to high strain rate dynamic tension. *Phil. Trans. R. Soc. A*, 375(2085):20160168, January 2017.
- [47] L. Fletcher, J. Van-Blitterswyk, and F. Pierron. Combined shear/tension testing of fibre composites at high strain rates using an image-based inertial impact test. In *EPJ Web of Conferences*, volume 183, page 02041, 2018.
- [48] A. Guigue, L. Fletcher, R. Seghir, and F. Pierron. IBII test for high strain rate tensile testing of adhesives. In J. Kimberley, L. E Lamberson, and S. Mates, editors, *Dynamic Behavior of Materials, Volume 1*, Conference Proceedings of the Society for Experimental Mechanics Series, pages 301–305. Springer International Publishing, 2018.
- [49] J. H. Kim, F. Pierron, M. R. Wisnom, and S. Avril. Local stiffness reduction in impacted composite plates from full-field measurements. *Composites Part A: Applied Science and Manufacturing*, 40(12):1961–1974, December 2009.
- [50] J. M. Considine, F. Pierron, K. T. Turner, P. Lava, and X. Tang. Smoothly varying in-plane stiffness heterogeneity evaluated under uniaxial tensile stress. *Strain*, 53(5):e12237, 2017.
- [51] B. Koohbor, A. Kidane, W.-Y. Lu, and Michael A. Sutton. Investigation of the dynamic stress–strain response of compressible polymeric foam using a non-parametric analysis. *International Journal of Impact Engineering*, 91:170–182, May 2016.
- [52] Aleksander Marek, Frances M. Davis, and Fabrice Pierron. Sensitivity-based virtual fields for the non-linear virtual fields method. *Computational Mechanics*, 60(3):409–431, September 2017.
- [53] F. Pierron and L. Fletcher. Generalized stress–strain curves for IBII tests on isotropic and orthotropic materials. *Journal of Dynamic Behavior of Materials*, 5(2):180–193, June 2019.
- [54] S. Avril, M. Grédiac, and F. Pierron. Sensitivity of the virtual fields method to noisy data. *Computational Mechanics*, 34(6):439–452, November 2004.
- [55] L. Fletcher and F. Pierron. The image-based inertial release test (IBIR) test: a new high strain rate test for stiffness strain-rate sensitivity identification. *Experimental Mechanics*, 2019. Submitted.
- [56] E. Toussaint, M. Grédiac, and F. Pierron. The virtual fields method with piecewise virtual fields. *International Journal of Mechanical Sciences*, 48(3):256–264, March 2006.
- [57] P. Wang, F. Pierron, M. Rossi, P. Lava, and O. T. Thomsen. Optimised experimental characterisation of polymeric foam material using DIC and the virtual fields method. *Strain*, 52(1):59–79, 2015.